UNIVERSIDADE FEDERAL DE SÃO CARLOS
Centro de Ciências Exatas e de Tecnologia
Departamento de Química
PROGRAMA DE PÓS-GRADUAÇÃO EM QUÍMICA

UNIVERSITAT JAUME I
Departament de Química Física i Analítica
PROGRAMA DE DOCTORADO EN CIENCIAS

"DESENVOLVIMENTO DE NOVAS TECNOLOGIAS BASEADAS EM MATERIAIS BIOCIDAS"

Marcelo de Assis*

Tese apresentada como parte dos requisitos para obtenção do título de DOUTOR EM CIÊNCIAS, área de concentração: QUÍMICA INORGÂNICA.

Orientador (UFSCar): Elson Longo
Co-Orientador (UFSCar): Jefferson Bettini
Orientador (UJI): Juan Andrés
Co-Orientador (UJI): Eva Maria Guillamón Torres

***bolsista CNPq (nº 166281/2017-4)**

São Carlos - SP

2021

UNIVERSIDADE FEDERAL DE SÃO CARLOS

Centro de Ciências Exatas e de Tecnologia
Programa de Pós-Graduação em Química

Folha de Aprovação

Defesa de Tese de Doutorado do candidato Marcelo de Assis, realizada em 13/08/2021.

Comissão Julgadora:

Prof. Dr. Elson Longo da Silva (UFSCar)

Prof. Dr. Mauricio Roberto Bomio Delmonte (UFRN)

Profa. Dra. Tatiana Martelli Mazzo (UNIFESP)

Profa. Dra. Regina Célia Galvão Frem (UNESP)

Profa. Dra. Yara Galvão Gobato (UFSCar)

O presente trabalho foi realizado com apoio da Coordenação de Aperfeiçoamento de Pessoal de Nível Superior - Brasil (CAPES) - Código de Financiamento 001.

O Relatório de Defesa assinado pelos membros da Comissão Julgadora encontra-se arquivado junto ao Programa de Pós-Graduação em Química.

“Sabe, eu acho que não sei fechar ciclos, colocar pontos finais. Comigo são sempre virgulas, aspas, reticências... eu vou gostando... eu vou cuidando, eu vou desculpando, eu vou superando, eu vou compreendendo, eu vou relevando, eu vou... e continuo indo, assim, desse jeito, sem virar páginas, sem colocar pontos....”

Caio Fernando Abreu

AGRADECIMENTOS

Primeiramente a tudo que nos faz mover, permanecer, ser, estar e mudar!

Resolvi ser um pouco mais profundo e falar sobre pessoas, pessoas estas que me ajudam a seguir todo dia, porque precisamos de pessoas para crescer, precisamos de pessoas para viver.

Os meus agradecimentos mais sinceros aos meus pais, **João Assis** e **Janet Assis**, por todo o esforço. Sei que minha personalidade hora conflituosa, hora teimosa me define de várias maneiras diferentes, mas não interfere no meu caráter e na minha honestidade que foi moldada por vocês. Obrigado pelos ensinamentos e pelos puxões de orelhas. Esta tese é especialmente para vocês.
A meu irmão **Rafael Assis**, meu ponto de paz e meu porto seguro. Obrigado por me ensinar tanto e ter essa paciência gigantesca comigo.
A minha cunhada e amiga **Danielle Assis**, que sempre esteve ao meu lado para me apoiar e me colocar para cima.
Ao meu ponto de luz, meu sobrinho **Kalel Assis**, por me contemplar com seu sorriso puro e me fazer querer ser uma pessoa melhor.
As minhas guerreiras **Regina Magda**, **Edilamar Araújo** e **Aparecida Assis**, por serem meus exemplos de vida, juntamente com meus tios e primos.

Um agradecimento mais que especial vai ao professor **Elson Longo**, sinônimo de paciência, caráter e integridade. Seus ensinamentos me moldaram como pesquisador e como pessoa.
Ao professor **Juan Andrés**, que com a sua persistência nos faz olhar o mundo com outros olhos e está sempre querendo fazer o melhor por todos os seus alunos.
A prof. **Eva Guillamón**, pelo acolhimento, pelo riso fácil e pelo ombro amigo. Te levarei sempre comigo!
Ao prof. **Jefferson Bettini** por estar sempre disponível a esclarecer minhas dúvidas ao longo do desenvolvimento do projeto.
A prof. **Rosa Llusar** por todo apoio do grupo de Materiais Moleculares (UJI).
Um agradecimento muito especial vai para este trio de mulheres fortes e cientistas que me acolheram e tiveram toda a paciência de me ensinar tudo o que sei até hoje, muito obrigado por tudo **Tatiana Mazzo**, **Rafaela Silveira** e **Içamira Nogueira**.

Ao grupo do **CDMF-LIEC** pela troca de conhecimentos, ajuda e pelas inúmeras risadas.
Ao grupo **QTC-UJI**, pelo acolhimento e amizade.
Ao grupo de **Materiales Moleculares-UJI** por toda estrutura e amizade.
Aos técnicos **Rorivaldo Camargo**, **Daniela Caceta**, **Madalena Turssi** e **Sandra Bellini** pela paciência e ajuda de sempre.
A **Nanox Tecnologia** por toda a estrutura e ajuda, em especial ao Gustavo Simões, Daniel Minozzi e Guilherme Tremiliosi.
Ao apoio financeiro recebido pela **FAPESP**, **FINEP**, **CNPq** e **CAPES**.

Essa jornada doida que é a pós graduação tinha que ser compartilhada com outros doidos. Dentro do CDMF-LIEC tive o prazer de fazer amigos para a vida toda, e aqui quero eterniza-los. A **Lara Kelly** por ser um pedaço de tudo, e me conhecer mais do que eu mesmo. A **Amanda Gouveia** por dividir tanta coisa e sempre evoluir junto comigo. A **Luma Garcia** por sempre me entender e ser minha parceira. A **Andressa Kubo**, que não ficava um dia sem tirar um sorriso do meu rosto. A **Camila Foggi** por cuidar e sempre estar por perto. A **Roberta Yonara** e **Aline Brandão**, que em tão pouco tempo foram eternizadas. A **Thaiane Robeldo** por partilhar

dos meus sufocos e passar os mesmos “nervosos”. A **Katiana Lima**, **Fabio Pires** e **Priscila Barros** por dividir tanto e sempre estarem juntos.

Por sorte fui agraciado por muitas pessoas maravilhosas que dividiram vários momentos inesquecíveis comigo em São Carlos. Gostaria de agradecer ao meu trio **Ana Clara**, **Renato Yonesake** e **Matheus Moreira**... são tantas as coisas que passamos junto que todo o afeto que sinto por vocês não cabe no meu peito. A **Mariana Ottaiano** e **Milena Maria** por me ensinar a tentar levar a vida mais leve e por ter essa coisa especial que é só nossa. Aos que me acompanham desde o início **Vitor Bolognesi**, **Felipe Santana** e **Gustavo Smidt**, vocês estiveram em momentos cruciais da minha jornada, e me fizeram crescer de maneiras inimagináveis. Ao meu par de vaso **Danilo Santana**, obrigado por ser meu porto seguro sempre. Aos meus parceiros de casa **André Filgueira**, **Pedro Flores** e **Henrique Landi**, cada um tem um espaço especial na minha vida. As amigas que o handebol me trouxe e que me fortalecem sempre, **Ana Iza** e **Beatriz Benassi**. A minhas parceiras de anos, que mesmo longe se tornam presentes sempre, **Juliana Bertin** e **Alessandra Miceli**. As curvas de rio que a AAA UFSCar colcou na minha vida, e que eu levarei pra sempre **Herisson Oliveira**, **Maria Gabriela**, **Lucas Galhardo**, **Karol Turssi**, **Alexandre Lamonica**, **Beatriz Alice, Juliana Argondizio**, **Ligia di Nardo**, **Leticia Natalino**, **Leticia Leis**, **Sabrina Petri**, **Taila Mariane**, **Karine Zanutto**, **Luisa Bergo**, **Georgia Semeghini**, **Mayra Bassini** e **Marina Barreto**. Aos de sempre, por permanecerem bem juntinhos de mim durante este periodo, **Raquel Vilela**, **Kamile Barletto**, **Jessica Vicentini**, **Thais Castro**, **Nataly Bellan, Marina Riciati** e **Thiago Cunha.** A melhor república que São Carlos já teve, **Repingado**, juntamente com meus amigos e irmãos **Igor Mesquita**, **Mathias Calil**, **Matheus Jacobsen**, **Gabriel Jacobsen**, **Lucas Guerra**, **Giovanni Mandarino** e **Jin Huang**.

O doutorado na UJI foi dividido em duas partes, e nessas duas partes tenho agradecimentos especiais. Lá em 2018, três brasileiros estavam perdidos em Castelló, tentando se virar como podiam, e levar a vida da melhor maneira possível. Durante este tempo só tenho a agradecer aos meus amigos **Samantha Custódio** e **Eduardo Gomes** pela parceria e cumplicidade. Já em 2021, minha família espanhola não podia ser melhor! Um muito obrigado mais do que especial a guapi **Maria Gutierrez** por ser meu ponto de fuga e meu braço direito dentro e fora do laboratório. A **Elena Pedrajas**, pelas risadas e pelos inúmeros “*No pasa nada*”, que por fim virou o lema da minha estadia. E por último a **Juanjo Mateu**, pelas palhaçadas e incontáveis sustos no laboratório. PS: A noticia do jornal espanhol nunca saiu (“Estudiantes de la UJI mueren en acidente...”). Amém!

A minha segunda família de São Carlos, **Handebol UFSCar**.
A **AAA UFSCar**, pelos anos de crescimento e inúmeros amigos.
A todos que torceram por mim de alguma forma e me mandaram boas energias durante toda a minha caminhada.
A **UFSCar** por me proporcionar os melhores anos da minha vida!

SOU FEDERAL, O SEU TERROR!

LIST OF TABLES

LIST OF FIGURES

RESUMO

DESENVOLVIMENTO DE NOVAS TECNOLOGIAS BASEADAS EM MATERIAIS BIOCIDAS. O surto mundial de pandemia de coronavírus (COVID-19) e outras infecções microbianas emergentes atraíram particular interesse para o design e desenvolvimento de novos agentes biocidas, com um amplo espectro de atividade. Desde então, estratégias eficientes precisam ser implementadas para o diagnóstico rápido, prevenção, controle e tratamento do vírus SARS-CoV-2, suas variantes, e outros patógenos oportunistas. No atual cenário de infecções por SARS-CoV-2, o desafio tecnológico reside no desenvolvimento de sistemas biocidas viáveis economicamente, reutilizáveis e capazes de inativar patógenos oportunistas, reduzindo, assim, o risco de infecção e transmissão. Nesse sentido, materiais a base de Ag utilizados em pequenas quantidades, podem se tornar atrativos para o desenvolvimento de novas tecnologias biocidas. O α-Ag_2WO_4, que já possui atividade biocida, quando modificado por elétrons ou laser em femtosegundos tem sua atividade biocida aumentada em até 32 vezes, contra bactérias resistentes (*Staphylococcus aureus* resistente a meticilina) e fungos (*Candida albicans*) devido a interface metal-semicondutor gerada (Ag/α-Ag_2WO_4). Além disso está modificação faz com que está interface seja seletiva para no combate de células cancerosas de bexiga (MB49), quando comparadas com células saudáveis (BALB/3T3), utilizando células modelo de camundongos. Outra interface estudada foi a de Ag/SiO_2 imobilizada em acetato-vinilo de etileno (EVA) que apresentou inibição de 99.99% de inibição de bactérias (*Staphylococcus aureus* e *Escherichia coli*) e fungos (*Candida albicans*), além de eliminar em apenas 2 minutos mais de 99% das réplicas do vírus SARS-CoV-2. Desta maneira pode-se obter tecnologias biocidas seguras utilizando interfaces metal-semicondutor baseadas em prata, que podem ser aplicadas para o design de equipamentos de proteção individual (EPI), embalagens, tecidos, implementos higiênicos, como implantes e próteses, e outros dispositivos economicamente viáveis para lutar contra o aumento de pandemias e riscos fatais associados a diversos patógenos.

Palavras-Chave: Interface metal-semicondutor, tungstato de prata, SiO_2-Ag, materiais biocidas, materiais anti-SARS-CoV-2.

ABSTRACT

DEVELOPMENT OF NEW TECHNOLOGIES BASED ON BIOCIDAL MATERIALS. The worldwide outbreak of the coronavirus pandemic (COVID-19) and other emerging microbial infections have attracted particular interest in the design and development of new biocidal agents with a broad spectrum of activity. Since then, efficient strategies need to be implemented for the rapid diagnosis, prevention, control and treatment of the SARS-CoV-2 virus, its variants, and other opportunistic pathogens. In the current scenario of SARS-CoV-2 infections, the technological challenge lies in the development of economically viable biocidal systems, reusable and capable of inactivating opportunistic pathogens, thus reducing the risk of infection and transmission. In this sense, Ag-based materials used in small quantities can become attractive for the development of new biocidal technologies. α-Ag_2WO_4, which already shows biocidal activity, when modified by electrons or femtosecond laser increases its biocidal activity up to 32x, against resistant bacteria (methicillin-resistant *Staphylococcus aureus*) and fungi (*Candida albicans*) due to the generated metal-semiconductor interface (Ag/α-Ag_2WO_4). In addition, this modification makes this interface selective for combating bladder cancer cells (MB49), *versus* healthy cells (BALB/3T3), using model mouse cells. Ag/SiO_2 immobilized on ethylene vinyl acetate (EVA) was another studied interface which showed 99.99% inhibition of bacteria (*Staphylococcus aureus* and *Escherichia coli*) and fungi (*Candida albicans*), besides eliminating in just 2 minutes over 99% of SARS-CoV-2 virus replicates. In this way, safe biocidal technologies can be obtained using silver-based metal-semiconductor interfaces, which can be applied to the design of personal protective equipment (PPE), packaging, fabrics, hygienic implements such as implants and prostheses, and other devices economically feasible to combat the increase in pandemics and fatal risks associated with various pathogens.

Keywords: Metal-semiconductor interfaces, Ag/α-Ag_2WO_4, SiO_2-Ag, biocidal materials, anti-SARS-CoV-2 materials.

RESUMEN

DESARROLLO DE NUEVAS TECNOLOGÍAS BASADAS EN MATERIALES BIOCIDALES. El brote mundial de la pandemia de coronavirus (COVID-19) y otras infecciones microbianas emergentes han atraído un interés particular en el diseño y desarrollo de nuevos agentes biocidas con un amplio espectro de actividad. Por esta razón, es necesario implementar estrategias eficientes para el diagnóstico, prevención, control y tratamiento rápido del virus SARS-CoV-2, sus variantes y otros patógenos oportunistas. En el escenario actual de infecciones por SARS-CoV-2, el desafío tecnológico radica en el desarrollo de sistemas biocidas económicamente viables, reutilizables y capaces de inactivar patógenos oportunistas, reduciendo así el riesgo de infección y transmisión. En este sentido, los materiales basados en Ag utilizados en pequeñas cantidades pueden resultar atractivos para el desarrollo de nuevas tecnologías biocidas. El α-Ag_2WO_4, que ya tiene actividad biocida, cuando se modifica por electrones o láser en femtosegundos ve incrementada su actividad biocida 32 veces frente a bacterias resistentes (*Staphylococcus aureus* resistente a meticilina) y hongos (*Candida albicans*) debido a la interfaz metal-semiconductor generada (Ag/α-Ag_2WO_4). Además, esta modificación hace que esta interfaz sea selectiva para combatir las células cancerosas de vejiga (MB49), *versus* las células sanas (BALB/3T3), utilizando células modelo de ratón. Otra interfaz estudiada fue Ag/SiO_2 inmovilizado en etileno vinil acetato (EVA), que mostró una inhibición del 99,99% de bacterias (*Staphylococcus aureus* y *Escherichia coli*) y hongos (*Candida albicans*), además de eliminar en sólo 2 minutos más del 99 % de réplicas del virus SARS-CoV-2. De esta forma, es posible obtener tecnologías biocidas seguras utilizando interfaces metal-semiconductor baseados en plata, que se pueden utilizar para el diseño de equipos de protección personal (EPI), embalajes, tejidos, implementos higiénicos, como implantes y prótesis, y otros dispositivos económicamente viables para combatir el aumento de pandemias y riesgos fatales asociados con diversos patógenos.

Keywords: Interfaz metal-semiconductor, wolframato de plata, SiO_2-Ag, materiales biocidas, materiales anti-SARS-CoV-2.

SUMÁRIO

1 – PUBLICATIONS

1.1 – Thesis Publications

1. Assis, M.; Simoes, L.G.P.; Tremiliosi, G.C; Coelho, D.; Minozzi, D.T.; Santos, R.I.; Vilela, D.C.B.; Santos, J.R.; Ribeiro, J.K.; Rosa, I.L.V.; Mascaro, L.H.; Andrés, J.; Longo, E. et al. SiO_2-Ag Composite as a Highly Virucidal Material: A Roadmap that Rapidly Eliminates SARS-CoV-2. Nanomaterials, 11, 638, 2021. DOI: 10.3390/nano11030638

2. Assis, M.; Robeldo, T.; Foggi, C. C.; Kubo, A. M.; Minguez-Vega, G.; Cordoncillo, E.; Beltran-Mir, H.; Torres-Mendieta, R.; Andrés, J.; Oliva, M.; Vergani, C. E.; Barbugli, P. A.; Camargo, E. R.; Borra, R. C.; Longo, E. Ag Nanoparticles/α-Ag_2WO_4 Composite Formed by Electron Beam and Femtosecond Irradiation as Potent Antifungal and Antitumor Agents. Scientific Reports, 9, 9927, 2019. DOI: 10.1038/s41598-019-46159-y

3. Assis, M.; Cordoncillo, E.; Torres-Mendieta, R.; Beltrán-Mir, H.; Mínguez-Vega, G.; Oliveira, R.; Leite, Edson R.; Foggi, C.C.; Vergani, C.E.; Longo, E.; Andrés, J. Towards the scale-up of the formation of nanoparticles on α-Ag_2WO_4 with bactericidal properties by femtosecond laser irradiation. Scientific Reports, 8, 1884, 2018. DOI: 10.1038/s41598-018-19270-9

1.2 – Another Publications

4. Assis, M.; Foggi, C.C.; Teodoro, V.; Costa, J.P.C.; Silva, C.E.; Robeldo, T.; Caperucci, P.F.; Vergani, C.E.; Borra, R.C.; Sorribes, I.; Gouveia, A.F.; San-Miguel, M.A.; Andrés, J.; Longo, E. Surface-Dependent Photocatalytic and Biological Activities of Ag_2CrO_4: Integration of Experiment and Simulation. Applied Surface Science, 545, 148964, 2021. DOI: 10.1016/j.apsusc.2021.148964

5. Mesquita, W.D.; Oliveira, M.C.; Assis, M.; Ribeiro, R.A.P.; Eduardo, A.C.; Teodoro, M.D.; Marques, G.E.; Junior, M.G.; Longo, E.; Gurgel, M.F.C. Unraveling the relationship between bulk structure and exposed surfaces and its effect on the electronic structure and photoluminescent properties of $Ba_{0.5}Sr_{0.5}TiO_3$: A joint experimental and theoretical approach. Materials Research Bulletin, 143, 111442, 2021. DOI: 10.1016/j.materresbull.2021.111442

6. Lima, A.E.B.; Reis, R.Y.N.; Ribeiro, L.S.; Ribeiro, L.K.; Assis, M.; Santos, R.S.; Fernandes, C.H.M.; Cavalcante, L.S.; Longo, E.; Osajima, J.A.O.; Luz, G.E. Microwave-assisted hydrothermal synthesis of $CuWO_4$-palygorskite nanocomposite for enhanced visible photocatalytic response. Journal of Alloys and Compounds, 863, 158731, 2021. DOI: 10.1016/j.jallcom.2021.158731

7. Assis, M.; Ponce, M.A.; Gouveia, A.F.; Souza, D.; Costa, J.P.C.; Teodoro, V.; Gobato, Y.G.; Andrés, J.; Macchi, C.; Somoza, A.; Longo, E. Revealing the Nature of Defects in α-Ag_2WO_4 by Positron Annihilation Lifetime Spectroscopy: A Joint Experimental
8. and Theoretical Study. Crystal Growth & Design, 21, 1093-1102, 2021. DOI: 10.1021/acs.cgd.0c01417

9. Sorribes, I.; Ventura-Espinosa, D.; Assis, M.; Martín, S.; Concepición, P.; Bettini, J.; Longo, E.; Mata, J.A.; Andrés, J. Unraveling a Biomass-Derived Multiphase Catalyst for the Dehydrogenative Coupling of Silanes with Alcohols under Aerobic Conditions. ACS Sustainable Chemistry & Engineering, 9, 2912, 2021. DOI: 10.1021/acssuschemeng.0c08953

10. Ramos, S. P.; Giaconia, M. A.; Assis, M; Jimenez, P.C.; Mazzo, T.M.; Longo, E.; Rosso, V.V.; Braga, A.R.C. Uniaxial and Coaxial Electrospinning for Tailoring Jussara Pulp Nanofibers. Molecules, 26, 1206, 2021. DOI: 10.3390/molecules26051206

11. Costa, J.P.C.; Teodoro, V.; Assis, M.; Andrés, J.; Carmo, J.P.P.; Longo, E. A scalable electron beam irradiation platform applied for allotropic carbon transformation. Carbon, 174, 567, 2021. DOI: 10.1016/j.carbon.2020.11.054

12. Godoy, K.F.; Rodolpho, J.M.A.; Brassolatti, P.; Fragelli, B.D.L.; Castro, C.A.; Assis, M.; Bernardi, J.C.; Correia, R.O.; Albuquerque, Y.R.; Speglich, C.; Longo, E.; Anibal, F.F. New Multi-Walled Carbon Nanotube of industrial interest induce cell death in murine fibroblast cells. Toxicology Mechanisms and Methods, (in press), 2021. DOI: 10.1080/15376516.2021.19930311

13. Rodolpho, J.M.A.; Godoy, K.F.; Brasoolatti, P.; Fragelli, B.D.L.; Castro, C.A.; Assis, M.; Speglich, C.; Cancino-Bernardi, J.; Longo, E.; Anibal, F.F. Apoptosis and oxidative stress triggered by carbon clack nanoparticle in the LA-9 fibroblast. Cellular Physiology and Biochemistry, (in press) 2021. DOI: 10.33594/000000382

14. Gondim, M.S.S.; Silva, E.C.; Santos, A.L.; Assis, M.; Mercury, J.M.R.; Leite, E.R.; Nogueira, I.C. Synthesis of $ZnWO_4$ by the polymerizable complex method: evidence of amorphous phase coexistence during the phase formation process. Ceramics International, (in press) 2021. DOI: 10.1016/j.ceramint.2021.03.253

15. Oliveira, L.P.; Foggi, C.C.; Pimentel, B.N.A.S.; Assis, M.; Andrés, J.; Longo, E.; Vergani, C.E. Increasing the photocatalytic and fungicide activities of Ag_3PO_4 microcrystals under visible-light irradiation. Ceramics International, (in press) 2021. DOI: 10.1016/j.ceramint.2021.04.27

16. Foggi, C.C.; Oliveira, R.C.; Assis, M.; Fabbro, M.T.; Mastelaro; V.R.; Vergani, C.E.; Gracia, L.; Andrés, J.; Longo, E.; Machado, A.L. Unveiling the role of β-Ag_2MoO_4 microcrystals to the improvement of antibacterial activity. Materials Science & Engineering C-Materials for Biological Applications, 111, 110765, 2020. DOI: 10.1016/j.msec.2020.110765

17. Teixeira, M.M.; Gobato, Y.G.; Gracia, L.; Silva, L.F.; Avansi, W.; Assis, M.; Oliveira, R.C.; Prando, G.A.; Andrés, J.; Longo, E. Towards a white-emitting phosphor $Ca_{10}V_6O_{25}$ based material. Journal of Luminescence, 220, 116990, 2020. DOI: 10.1016/j.jlumin.2019.116990

18. Ramos, S.; Giaconia, M.; Marco, J.; Paiva, R. S.; Rosso, V.V.; Lemes, A.; Egea, M.; Assis, M.; Mazzo, T. M.; Longo, E.; Braga, A. R. C. Development and Characterization

19. of Electrospun Nanostructures Using Polyethylene Oxide: Potential Means for Incorporation of Bioactive Compounds. Colloids and Interfaces, 4, 14, 2020. DOI: 10.3390/colloids4020014

20. Assis, M.; Ribeiro, R.A.P.; Carvalho, M.H.; Teixeira, M.M.; Gobato, Y.G.; Prando G.A.; Mendonça, C.B.; De Boni, L.; Oliveira, A.J.A.; Bettini, J.; Andrés, J.; Longo, E. Unconventional Magnetization Generated from Electron Beam and Femtosecond Irradiation on α-Ag_2WO_4: A Quantum Chemical Investigation. ACS Omega, 5, 10052, 2020. DOI: 10.1021/acsomega.0c00542

21. Assis, M.; Groppo Filho, F.C.; Pimentel, D.S.; Robeldo, T.; Gouveia, A.F.; Castro, T.F.D.; Fukushima, H.C.S.; Foggi, C.C.; Costa, J.P.C.; Borra, R.C.; Andrés, J.; Longo, E. Ag Nanoparticles/AgX (X=Cl, Br and I) Composites with Enhanced Photocatalytic Activity and Low Toxicological Effects. ChemistrySelect, 5, 4655, 2020.DOI: 10.1002/slct.202000502

22. Tello, A.C.M.; Assis, M.; Menasce, R.; Gouveia, A.F.; Teodoro, V.; Jacomaci, N.; Zaghete, M.A.; Andrés, J.; Marques, G.E.; Teodoro, M.D.; Silva, A.B.F.; Bettini, J.; Longo, E. Microwave-Driven Hexagonal-to-Monoclinic Transition in BiPO4: An In-Depth Experimental Investigation and First-Principles Study. Inorganic Chemistry, 59, 7453, 2020. DOI: 10.1021/acs.inorgchem.0c00181

23. Costa, J.P.C.; Assis, M.; Teodoro, V.; Rodrigues, A.; Foggi, C.C.; San-Miguel, M.; Carmo, J.P.P.; Andrés, J.; Longo, E. Electron beam irradiation for the formation of thick Ag film on Ag_3PO_4. RSC Advances, 10, 21745, 2020. DOI: 10.1039/D0RA03179H

24. Laier, L.O.; Assis, M.; Foggi, C.C.; Gouveia, A.F.; Vergani, C.E.; Santana, L.C.L.; Cavalcante, L.S.; Andrés, J.; Longo, E. Surface-dependent properties of α-Ag_2WO_4: a joint experimental and theoretical investigation. Theoretical Chemistry Acounts, 139, 108, 2020. DOI:10.1007/s00214-020-02613-z

25. Trindade, L. G.; Zanchet, L.; Dreon, R.; Souza, j.C.; Assis, M.; Longo, E.; Martini, E.M.A.; Chiquito, A.J.; Pontes, F.M. Microwave-assisted solvothermal preparation of Zr-BDC for modification of proton exchange membranes made of SPEEK/PBI blends. Journal of Materials Science, 55, 14938, 2020. DOI: 10.1007/s10853-020-05068-6

26. Penha, M.D.; Gouveia, A.F.; Teixeira, M.M.; Oliveira, R.C>; Assis, M.; Sambrano, J.R.; Yokaichya, F.; Santos, C.C.; Gonçalves, R.F.; Li, M.S.; San-Miguel, M.A.; Andrés, J.; Longo, E. Structure, optical properties, and photocatalytic activity of α-$Ag_2W_{0.75}Mo_{0.25}O_4$. Materials Research Bulletin, 132, 111011, 2020. DOI: 10.1016/j.materresbull.2020.111011

27. Cruz, L.; Teixeira, M.M.; Teodoro, V.; Jacomaci, N.; Laier, L.O.; Assis, M.; Macedo, N.G.; Tello, A.C.M.; Silva, L.F.; Marques, G.E.; Zaghete, M.A.; Teodoro, M.D.; Longo, E. Multi-Dimensional Architecture of Ag/α-Ag_2WO_4 Crystals: Insights into Microstructural, Morphology, and Photoluminescent Properties. Crystengcomm, 22, 7903-7917, 2020. DOI: 10.1039/D0CE00876A

28. Torres-Mendieta, R.O.; Teixeira, M.M.; Minguez-Vega, G.; Souza, D.; Gobato, Y.G.; Assis, M.; Beltran-Mir, H.; Cordoncillo, E.; Andrés, J.; Cernik, M.; Longo, E. Toward Expanding the Optical Response of Ag_2CrO_4 and Bi_2O_3 by Their Laser-Mediated

29. Heterojunction. Journal of Physical Chemistry C, 124, 26404, 2020. DOI: 10.1021/acs.jpcc.0c08301

30. Pinatti, I.M.; Pereira, P.F.S.; Assis, M.; Longo, E.; Rosa, I.L.V. Rare earth doped silver tungstate for photoluminescent applications. Journal of Alloys and Compounds, 771, 433-447, 2019. DOI: 10.1016/j.jallcom.2018.08.302

31. Assis, M.; Oliveira, M.C.; Machado, T.R.; Macedo, N.G.; Costa, J.P.C.; Gracia, L.; Andrés, L.; Longo, E. In Situ Growth of Bi Nanoparticles on $NaBiO_3$, δ-, and β-Bi_2O_3 Surfaces: Electron Irradiation and Theoretical Insights. Journal of Physical Chemistry C, 123, 5023-5030, 2019. DOI: 10.1021/acs.jpcc.8b11566

32. Macedo, N.G.; Machado, T.R.; Roca, R.A.; Assis, M.; Foggi, C.C.; Puerto-Beldia, V.; Minguez-Vega.; Rodrigues, A.; San-Miguel, M.A.; Cordoncillo, E.; Beltran-Mir, H.; Andrés, J.; Longo, E. Tailoring the bactericidal activity of Ag nanoparticles/α-Ag_2WO_4 composite induced by electron beam and femtosecond laser irradiation: Integration of experiment and computational modeling. ACS Applied Bio Materials, 2, 824, 2019. DOI: 10.1021/acsabm.8b00673

33. Lemos, P.S.; Silva, G.S.; Roca, R.A.; Assis, M.; Torres-Mendieta, R.; Beltran-Mir, H.; Minguez-Vega, G.; Cordoncillo, E.; Andrés, J.; Longo, E. Laser and electron beam-induced formation of Ag/Cr structures on Ag_2CrO_4. Physical Chemistry Chemical Physics, 21, 6101, 2019. DOI: 10.1039/C8CP07263A

34. Chaves, M.J.S.; Lima, G.O.; Assis, M.; Mendonça, C.J.S.; Pinatti, I.M.; Gouveia, A.F.; Rosa, I.L.V.; Longo, E.; Almeida, M.A.P.; Franco, T.C.R.S. Environmental remediation properties of Bi_2WO_6 hierarchical nanostructure: A joint experimental and theoretical investigation. Journal of Solid-State Chemistry, 274, 270, 2019. DOI: 10.1016/j.jssc.2019.03.031

35. Santos, C.C.; Assis, M.; Machado, T.R.; Pereira, P.F.S.; Minguez-Vega, G.; Cordoncillo, E.; Beltran-Mir, H.; Donate-Buendia, C.; Andrés, J.; Longo, E. Proof of Concept Studies Directed toward the Formation of Metallic Ag Nanostructures from Ag_3PO_4 Induced by Electron Beam and Femtosecond Laser. Particle & Particle Systems Characterization, 36, 1800533, 2019. DOI: 10.1002/ppsc.201800533

36. Silva, J.S.; Machado, T.R.; Martins, T.A.; Assos, M.; Foggi, C.C.; Macedo, N.G.; Beltran-Mir, H.; Cordoncillo, E.; Andrés, J; Longo, E. α-$AgVO_3$ Decorated by Hydroxyapatite ($Ca_{10}(PO_4)_6(OH)_2$): Tuning Its Photoluminescence Emissions and Bactericidal Activity. Inorganic Chemistry, 58, 5900-5913, 2019. DOI: 10.1021/acs.inorgchem.9b00249

37. Silva, E.Z.; Faccin, G.M.; Machado, T.R.; Assis, M.; Macedo, N.G.; Maya-Johnson, S.; Sczancoski, J.C.; Andrés, J.; Longo, E.; San-Miguel, M.A. Connecting Theory with Experiment to Understand the Sintering Processes of Ag Nanoparticles. Journal of Physical Chemistry C, 123, 11310-11318, 2019. DOI: 10.1021/acs.jpcc.9b02107

38. Pereira, P. F. S.; Gouveia, A. F.; Assis, M.; Oliveira, R.C.; Pinatti, I.M.; Penha, M.; Gonçalves, R.F.; Gracia, L.; Andrés, J.; Longo, E. $ZnWO_4$ nanocrystals: synthesis, morphology, photoluminescence and photocatalytic properties. Physical Chemistry Chemical Physics, 20, 1923, 2018. DOI: 10.1039/C7CP07354B

39. Trindade, L.G.; Minervino, G.B.; Trench, A.B.; Carvalho, M.H.; Assis, M.; Li, M.S.; Oliveira, A.J.A.; Pereira, E.C.; Mazzo, T.; Longo, E. Influence of ionic liquid on the photoelectrochemical properties of ZnO particles. Ceramics International, 44, 10393, 2018. DOI: 10.1016/j.ceramint.2018.03.053

40. Macedo, N.G.; Gouveia, A.F.; Roca, R.A.; Assis, M.; Gracia, L.; Andrés, J.; Leite, E.R.; Longo, E. Surfactant-Mediated Morphology and Photocatalytic Activity of α-Ag_2WO_4 Material. Journal of Physical Chemistry C, 122, 8667, 2018. DOI: 10.1021/acs.jpcc.8b01898

41. Trench, A.B.; Machado, T.R.; Gouveia, A.F. Assis, M.; Trindade, L.G.; Santos, C.C.; Perrin, A.; Perrin, C.; Oliva, M.; Andrés, J.; Longo, E. Connecting structural, optical, and electronic properties and photocatalytic activity of Ag_3PO_4:Mo complemented by DFT calculations. Applied Catalysis B, 238, 198, 2018. DOI: 10.1016/j.apcatb.2018.07.019

42. Assis, M.; Cordoncillo, E.; Torres-Mendieta, R.; Beltran-Mir, H.; Minguez-Vega, G.; Gouveia, A.F.; Leite, E.R.; Andrés, J.; Longo, E. Laser-Induced Formation of Bismuth Nanoparticles. Physical Chemistry Chemical Physics, 20, 13693, 2018. DOI: 10.1039/C8CP01225C

43. Machado, T.R.; Macedo, N.G.; Assis, M.; Donate-Buendia, C.; Minguez-Vega, G.; Teixeira, M.M.; Foggi, C.C.; Bergani, C.E.; Beltran-Mir, H.; Andres, J.; Cordoncillo, E.; Longo, E. From Complex Inorganic Oxides to Ag-Bi Nanoalloy: Synthesis by Femtosecond Laser Irradiation. ACS Omega, 3, 9880-9887, 2018. DOI: 10.1021/acsomega.8b01264

44. Assis, M.; Macedo, N.G.; Machado, T.R.; Ferrer, M.M.; Gouveia, A.F.; Cordoncillo, E.; Torres-Mendieta, R.; Beltran-Mir, H.; Minguez-Vega, G.; Leite, E.R.; Sambrano, J.R.; Andrés, J.; Longo, E. Laser/Electron Irradiation on Indium Phosphide (InP) Semiconductor: Promising Pathways to In Situ Formation of Indium Nanoparticles. Particle & Particles Systems Characterization, 35, 1800237, 2018. DOI: 10.1002/ppsc.201800237

45. Oliveira, M.C.; Ribeiro, R.A.P.; Gracia, L.; Lazaro, S.R.; Assis, M.; Oliva, M.; Rosa, I.L.V.; Gurgel, M.F.C.; Longo, E.; Andrés, J. Experimental and theoretical study of the energetic, morphological, and photoluminescence properties of $CaZrO_3$:Eu^{3+}. Crystengcomm, 20, 5519, 2018. DOI: 10.1039/C8CE00964C

46. Gouveia, A.F.; Assis, M.; Cavalcante, L.S.; Gracia, L.; Longo, E.; Andrés, J. Reading at exposed surfaces: theoretical insights into photocatalytic activity of $ZnWO_4$. Frontier Research Today, 1, 1, 2018. DOI: 10.31716/frt.201801005

47. Oliveira, R.C.; Zanetti, S.M.; Assis, M.; Penha, M.; Mondego, M.; Cilense, M.; Longo, E.; Cavalcante, L.S. Effect of metallic Ag growth on the electrical resistance of 3D flower-like $Ag_4V_2O_7$ crystals. Journal of the American Ceramics Society, 100, 2358, 2017. DOI: 10.1111/jace.14803

48. Oliveira, R.C.; Foggi, C.C.; Teixeira, M.M.; Silva, M.D.P.; Assis, M.; Francisco, E.M.; Pimentel, B.N.A.S.; Vergani, C.E.; Machado, A.L.; Andrés, J.; Gracia, L.; Longo, E.

49. Mechanism of Antibacterial Activity via Morphology Change of α-$AgVO_3$: Theoretical and Experimental Insights. ACS Applied Materials & Interfaces, 9, 11472, 2017. DOI: 10.1021/acsami.7b00920

50. Oliveira, M.C.; Gracia, L.; Assis, M.; Rosa, I.L.V.; Gurgel, M.F.C.; Longo, E.; Andrés, J. Mechanism of photoluminescence in intrinsically disordered $CaZrO_3$ crystals: First principles modeling of the excited electronic states. Journal of Alloys and Compounds, 722, 981, 2017. DOI: 10.1016/j.jallcom.2017.06.052

1 – INTRODUCTION

Research on nanostructured materials has contributed great excitement to the material science field. Their small dimensions do not only allow more surface functionality in a given volume, but also lead to physical properties that usually differ from their bulk counterparts in many aspects, including electronic, optical, and magnetic features. (BARUAH and DUTTA, 2009; CHERIYAMUNDATH and VAVILALA, 2021; GUSEINOV and ILYIN, 2021) These properties include quantum confinement in semiconductors, surface plasmon resonance in metals, and superparamagnetism in magnetic materials, due to a substantial increase in the ratio of activated atoms on the surface and the optimization of surface effects. (BUOT, 1993; KANAPARTHY and KANAPARTHY, 2011; KIM et al., 2009; YU and MEYYAPPAN, 2006) Dispersed nanoparticles can be used as the building structured components of solid materials allowing to control their final shape and size, starting from individual dispersed nanoparticles and liquid-stabilized colloids. (ICHIKAWA et al., 2003) The contour region between nanoparticles plays an important role in terms of structure, size and chemical composition**,** because the excess energy accumulates in this area, namely interfaces, which is a region with a high density of defects. (GRANO et al., 2013) Indeed dispersions of oxide nanoparticles, in particular, can be used to obtain sensors, (KOH and JOSEPHSON, 2009; PERFÉZOU et al., 2012; WANG et al., 2010) inorganic membranes, (BALTA et al., 2012; SHCHUKIN and CARUSO, 2003) electrolytes for fuel cells, (OLAYIWOLA and DEJAM, 2020; VIDAL-IGLESIAS et al., 2012) solar energy conversion, (CHEN et al., 2018; MA et al., 2018) water splitting, (FOMINYKH et al., 2014; SATHISH et al., 2006) catalysts (ASTRUC et al., 2005; LI et al., 2011; PRIETO et al., 2013) and biocidal materials. (ELTARAHONY et al., 2018; HUANG et al., 2018) This allows for the preparation of a wide variety of materials with different properties. (CILEK and KARACA, 2015)

Nanoscience and nanotechnology has a huge impact in many different domains of society and industrial sectors, such as health, food, communication, technology, energy and environment. (KHAN et al., 2019) New products derived from advances in nanotechnology require new materials, specifically functional nanoparticles. In particular, nanomaterials based on metals and semiconductor oxides are of particular industrial interest due to their unique properties and applications, both in technology and in biomedicine. (SALATA, 2004) In this sense, studies on crystal growth process, evolution of the morphology and the corresponding mechanisms are extremely important. Thus, new strategies for morphological control and particle size have become the target of research interest. (ASSIS and DE FOGGI et al., 2021; DE FOGGI et al., 2020; PEREIRA et al., 2018)

Among their applications, nanostructured materials appear as potential biocidal agents due to their unique chemical and physical properties. (CHINTAGUNTA et al., 2021; GHAFFARI et al., 2021; JINDAL and GOPINATH, 2020). Furthermore, it is possible to modify and maximize their properties by controlling their size and surface area. (SUGIMOTO, 2007; XU et al., 2006) SARS-CoV-2 and many other infectious diseases caused by microorganisms are often transmitted by human body fluids, mainly through eyes, mouth or nose, (PRATHER et al., 2020) and results suggest that these pathogens can survive for several days in different surfaces. (CHIN et al., 2020) One way to reduce the transmission *via* these surfaces is to design coatings able to eliminate these pathogens by applying them on common surfaces such as door handles, bus supports, etc., reducing the elimination period from weeks (VAN DOREMALEN et al., 2020) to hours or minutes. In this context, Behzadinasab (BEHZADINASAB et al., 2020) and Hosseini (HOSSEINI et al., 2021) observed that coatings based on copper oxides eliminate copies of SARS-CoV-2 when in contact with these surfaces, due to the production of reactive oxygen species (ROS) that degrade constituent proteins and membranes of these microorganisms. Promising results have also been obtained using semiconductors, such as ZnO, (TAVAKOLI et al., 2018; TE VELTHUIS et al., 2010) TiO_2 (MLCOCHOVA et al., 2020) and Fe_2O_3/Fe_3O_4. (ABO-ZEID et al., 2020) Noble metal particles, such as Au and Ag, have also been developed as biocidal materials, especially anti-SARS-CoV-2, as they can interact with various functional groups that make up the virus, preventing its replication or destroying it. (BUI et al., 2020; JEREMIAH et al., 2020; PANDEY et al., 2021) Carbon-based materials, such as graphene and chitosan, are also effective against microorganisms, as these materials interact permanently with the RNA. (MAIO et al., 2020; MILEWSKA et al., 2021) An interesting advantage to using inorganic materials to combat virus in general, is that the virus is less likely to develop resistance compared to conventional therapies. (CHEN, et al., 2013; GAIKWAD et al., 2013; LARA et al., 2010; SPESHOCK et al., 2010)

Although a lot of knowledge about materials and nanomaterials has been acquired during the last 20 years of research, there is still a lot of room to improve the unconventional synthesis processes. Innovation and technological transfer of these biocidal materials to the market continues being a challenge, enabling the economic viability. Theoretical and experimental studies capable to connect the morphology with their properties have been presented. In fact, it is possible to predict some properties of these materials by analyzing geometry, electronic and magnetic properties at the exposed surfaces. Currently, morphology and property of several complex semiconductors have been theoretically correlated, such as: β-

Ag_2MoO_4, (DE FOGGI et al., 2020) Ag_2CrO_4, (ASSIS and DE FOGGI et al., 2021) $BiPO_4$, (TELLO et al., 2020) α-Ag_2WO_4, (CRUZ et al., 2020; LAIER et al., 2020; MACEDO et al., 2018) $ZnWO_4$, (PEREIRA et al., 2018) α-$AgVO_3$ (DE OLIVEIRA, et al., 2017) and $Ag_4V_2O_7$. (DE OLIVEIRA, et al., 2016) In this way, we are able to associate the biocidal property with the semiconductor morphology, finding the best method of synthesis to maximize their activity.

Once the best morphology and synthetic methodology has been defined, the formation of a metal/semiconductor interface can still enhance the biocidal activity of the material. The development and use of heterojunctions, composed of a metal and semiconductor, in this case metallic nanoparticles (NPs) deposited on the surface of a semiconductor, lead to advantageous characteristics related to the effects of superficial plasmon resonance and the Schottky contact. This creates additional local active sites together with the presence of electronic traps, (CLAVERO, 2014; KNIGHT et al., 2011; ZHANG et al., 2018) that are used to improve the generation of electron-hole pairs (e^- - h^+) in the semiconductor. Such effect results in an increase in the production of ROS through the metal/semiconductor interface, which are responsible for the oxidative stress of microorganisms. In order to obtain these interfaces, two techniques currently stand out: using femtosecond laser and/or electron beam irradiation. (ASSIS e CORDONCILLO et al., 2018; LONGO, E e colab., 2013) These techniques can be considered green processes as they do not use toxic solvents and do not generate by-products during their development, that is, there is no formation of any kind of waste. By using both techniques, internal atoms that make up the semiconductor migrate to the surface, giving rise to the metal/semiconductor interfaces and generating internal metallic vacancies in the semiconductor. (ASSIS e CORDONCILLO et al., 2018; ASSIS e GROPPO FILHO et al., 2020; ASSIS e PONTES RIBEIRO et al., 2020; DOS SANTOS et al., 2019)

The femtosecond laser irradiation is capable of reducing metal cations to form metallic Ag, (ASSIS and CORDONCILLO et al. 2018; ASSIS and RIBEIRO et al., 2020; DOS SANTOS et al., 2019; MACEDO et al., 2019) Bi (ASSIS and CORDONCILLO et al., 2018; MACHADO et al., 2018) and In (ASSIS and MACEDO et al., 2018) in several different semiconductor matrices, such as α-Ag_2WO_4, (ASSIS and CORDONCILLO et al., 2018; ASSIS and PONTES RIBEIRO et al., 2020; MACEDO et al., 2019) Ag_3PO_4, (DOS SANTOS et al., 2019) Ag_2CrO_4, (LEMOS et al., 2019) $NaBiO_3$ (MACHADO et al., 2018) and InP.(ASSIS et al., 2018) In addition, this physical modification can generate metastable phases and form unusual metal alloys, due to the high photon density focused on a small area. (MACHADO et al., 2018) On the other hand, under electron beam irradiation different nanoparticles of Ag, (LONGO, et al., 2013; LONGO, et al., 2016) Bi, (ASSIS et al., 2019) In, (ASSIS and MACEDO

et al., 2018) Cu, (PARK et al., 2014) Li, (GHATAK et al., 2012) are also obtained. Thus, laser and electron beam irradiation constitute both synthetic and microfabrication techniques to prepare nanostructures and nanomaterials (metal/semiconductor) in an accessible and controlled manner. These materials can be explored an applied in different biotechnological fields, due to their unique physico-chemical properties. In this way, minimizing the amount of metal NPs and/or metal oxide NPs as semiconductor in the encapsulation process commercial materials becomes essential for the development of a final and economically available product.

As a result of research efforts, there are countless technologies on the market based on the versatility of nanomaterials nowadays. In particular, the worldwide, extraordinary outbreak of coronavirus pandemic (*i.e.,* COVID-19) and other emerging viral expansions have drawn particular interest to the design and development of novel antiviral and viricidal agents, with a broad-spectrum of antiviral activity. The present and crucial challenge lies in the development of universal virus repudiation systems that are reusable, and capable of inactivating pathogens, thus reducing risk of infection and transmission. Based on the type of materials used at the contaminated sites, the antiviral coatings have been divided into three major groups: antiviral polymers, metal ions/metal oxides, and functional nanomaterials. Both antiviral and viricidal compositions and surface modification technologies play a major role in the destruction of pathogens, by providing a thin film over the surface to retain its biocide activity.

Up to now, various nanomaterials have been designed and developed for diagnosing SARS-CoV-2 and controlling its spread. (CARVALHO et al., 2021) Metal NPs like Ag, Au, and metal oxide NPs such as CuO, TiO_2, and Fe_3O_4 have been extensively applied for the COVID-19 management because of their exceptional features. (MALLAKPOUR, et al. 2021) On this regard, anti-viral and antibacterial coatings, face masks, immunosensors and diagnostic kits for timely identification have been developed by using such NPs. Moreover, synthetic polymers (*i.e*., polypropylene, polystyrene, and poly(vinyl)alcohol) and natural polymers (such as alginate, chitosan, etc.) have revealed a critical role to control and fight against the COVID-19 outbreak. Using these macromolecules, various medical devices and equipment such as diagnostic kits, anti-viral coatings, face masks, and shields for protection, disinfection, and immunization have been developed. (MALLAKPOUR, et al. 2021)

Nevertheless, the above antiviral composites are produced through complex and expensive manufacturing processes, which render them non-viable for a global solution of the COVID-19 pandemic. Recently, a new composite formed from polycotton and Ag NPs has been developed and has proved up to 99% of the SARS-CoV-2 virus, bacteria and fungi efficiency, resulting in a biocidal and economically viable fabric. (TREMILIOSI et al., 2020)

In the last work, stabilization of Ag NPs in amorphous SiO_2, immobilizing this heterojunction in a polymeric matrix (ethyl vinyl acetate, EVA) is highlighted, with 99.85% elimination of the SARS-CoV-2 virus in 10 minutes, and a useful life of 2 years. (ASSIS and SIMOES et al., 2021).

2 – PUBLISHED ARTICLES

The published articles that compose this doctoral thesis with the associated experimental approach are found at the following pages.

2.1 – Towards the scale-up of the formation of nanoparticles on α-Ag_2WO_4 with bactericidal properties by femtosecond laser irradiation

www.nature.com/scientificreports

SCIENTIFIC REPORTS

OPEN

Received: 1 September 2017
Accepted: 16 December 2017
Published online: 30 January 2018

Towards the scale-up of the formation of nanoparticles on α-Ag_2WO_4 with bactericidal properties by femtosecond laser irradiation

Marcelo Assis[1], Eloisa Cordoncillo[2], Rafael Torres-Mendieta[3], Héctor Beltrán-Mir[2], Gladys Mínguez-Vega[4], Regiane Oliveira[1], Edson R. Leite[1], Camila C. Foggi[5], Carlos E. Vergani[5], Elson Longo[1] & Juan Andrés[6]

In recent years, complex nanocomposites formed by Ag nanoparticles coupled to an α-Ag_2WO_4 semiconductor network have emerged as promising bactericides, where the semiconductor attracts bacterial agents and Ag nanoparticles neutralize them. However, the production rate of such materials has been limited to transmission electron microscope processing, making it difficult to cross the barrier from basic research to real applications. The interaction between pulsed laser radiation and α-Ag_2WO_4 has revealed a new processing alternative to scale up the production of the nanocomposite resulting in a 32-fold improvement of bactericidal performance, and at the same time obtaining a new class of spherical $Ag_xW_yO_z$ nanoparticles.

Towards the scale-up of the formation of nanoparticles on α Ag_2WO_4 with bactericidal properties by femtosecond laser irradiation

Marcelo Assis[1], Eloisa Cordoncillo[2], Rafael Torres-Mendieta[3], Héctor Beltrán-Mir[2], Gladys Mínguez-Vega[4], Regiane Oliveira[1], Edson R. Leite[1], Camila C. Foggi[5], Carlos E. Vergani[5], Elson Longo[1] & Juan Andrés[6]

[1]CDMF-UFSCar, Universidade Federal de São Carlos, P.O. Box 676, CEP, 13565-905, São Carlos, SP, Brazil.
[2]Department of Inorganic and Organic Chemistry, University Jaume I (UJI), Castelló, 12071, Spain.
[3]Institute for Nanomaterials, Advanced Technologies and Innovation Technical University of Liberec, Studentská 1402/2, 46117, Liberec, Czech Republic.
[4]GROC·UJI, Institut de Noves Tecnologies de la Imatge (INIT, University Jaume I (UJI), Castelló, 12071, Spain.
[5]FOAr-UNESP, Universidade Estadual Paulista, P.O. Box 1680, 14801903, Araraquara, SP, Brazil.
[6]Department of Analytical and Physical Chemistry, University Jaume I (UJI), Castelló, 12071, Spain.

In recent years, complex nanocomposites formed by Ag nanoparticles coupled to an α-Ag_2WO_4 semiconductor network have emerged as promising bactericides, where the semiconductor attracts bacterial agents and Ag nanoparticles neutralize them. However, the production rate of such materials has been limited to transmission electron microscope processing, making it difficult to cross the barrier from basic research to real applications. The interaction between pulsed laser radiation and α-Ag_2WO_4 has revealed a new processing alternative to scale up the production of the nanocomposite resulting in a 32-fold improvement of bactericidal performance, and at the same time obtaining a new class of spherical $Ag_xW_yO_z$ nanoparticles.

Introduction

The ever-increasing use of semiconductors in daily human life has brought a wave of new materials with a wide range of technological applications. In particular, one of the semiconductor families that has attracted the most attention in recent years is the family of ternary tungsten oxides, such as metal tungstates (with the general formula MWO_4), which are a class of functional materials with fascinating properties at the cutting edge of fundamental science, as well as having many potential applications that are studied and applied widely in many fields[1-3]. Within this family of materials, silver tungstate (α-Ag_2WO_4) is an important inorganic material that has attracted significant attention owing to its applications in photocalalysts, photoswitches, or as an alternative to conventional wide band gap semiconductors[4-13]. Recent studies have demonstrated that crystals of α-Ag_2WO_4 showed a

metal nanoparticle growth attached to the semiconductor framework, which in the near future may lead to outstanding applications due to Ag segregation, such as photocatalysis, ozone sensing and bacteriocidicity[3,5,8,14-22].

Despite the great potential for growing novel metal nanoparticles on the framework of tungstate semiconductors, the ability to grow and control their molecular structure has been limited to Transmission Electron Microscopy (TEM) processing[2,23-31]. It is of exceptional scientific importance to scale up the production of the assembly under non-special conditions, and at the same time the methodology should provide enough versatility to be extensible to a wide range of materials. In this context, ultrashort laser irradiation over the sample in air may represent an alternative, as it can be easily integrated within a production process. Other alternatives may be electron beam machining.

The influence of laser irradiation over materials promotes a complex interplay between various physical and chemical mechanisms associated with sub-nanosecond timescale processes, influencing the constituent elements of materials in an intense way, which may result in the emergence of changes in the macroscopic behavior of materials due to internal modifications. In this sense, the current scientific literature demonstrates an ever-increasing use of femtosecond laser radiation in processing materials, the induction of a nanometric structure in bulk materials being its most popular use for obtaining novel species that present highly attractive properties for technological advances[32–37]. However, the ease with which the structure of materials can be modified at nanometric scales also allows the manufacture of novel complex nanoensembles[38–41]. Nowadays, the femtosecond laser-matter interactions that lead to the production of such promising materials are still not fully understood. However, the reliability and versatility of using pulsed laser radiation for nanomaterials has led to an exponential growth in its use[42–44].

Based on this fact, in this communication we seek to fulfill a three-fold objective. The first is to report the novel formation of Ag and ($Ag_xW_yO_z$) nanoparticles from α-Ag_2WO_4 by laser-assisted irradiation, where a large amount of material is created and non-special conditions are required, rather than irradiating the α-Ag_2WO_4 sample in air. These results are compared with those obtained in previous theoretical and experimental studies on the response triggered by electron beam irradiation on α-Ag_2WO_4. Second, based on this comparison, an explanation is given to unveil the formation of Ag nanoparticles occurring along the laser interaction. The third aim is to demonstrate that laser-irradiated samples have a much higher bactericidal activity than samples treated with electron beams. We believe that these novel results are of outstanding relevance, since they may inspire the efficient synthesis of nanocompounds and contribute to

broadening the fundamental knowledge on the effect of laser-matter interactions.

Experimental Results

In this proof-of-concept experiment to demonstrate the ability of the femtosecond laser to increase the efficiency of the production of nanoparticles over large areas of α-Ag_2WO_4 and test its bactericidal activity, an 8 mm × 8 mm portion of the surface of each sample was irradiated. The samples were then characterized by high resolution TEM (HR-TEM) and analyzed by energy dispersive X-ray spectroscopy (EDS). In parallel, bactericidal activity was tested by bringing the treated samples into contact with Planktonic cultures of Methicillin-Resistant Staphylococcus Aureus ATCC 33591 (MRSA), and then analyzing them by scanning microscopy (SEM) and confocal laser scanning microscopy (CLSM).

Material characterization. Powder and pellet samples of α-Ag_2WO_4 were prepared and irradiated following two different routes. Protocol I consisted in irradiating the sample with a spot diameter in the order of 20 µm at a fluence of about 60 J/cm2. In protocol II the sample was irradiated with a spot diameter of approximately 84 µm at a fluence of about 3.6 J/cm2. The samples were then characterized by HR-TEM and analyzed by EDS.

In protocol I, two different chemical regions can be distinguished based on the change in color of the material. On the one hand, the laser interaction leaves a clear black line on the sample whereas, on the other hand, the extremely high density of photons also leads to the formation of a plasma plume which produces a red cloud that can deposit with time, as can be observed in Fig. 1, where the samples are exhibited under the laser irradiation process.

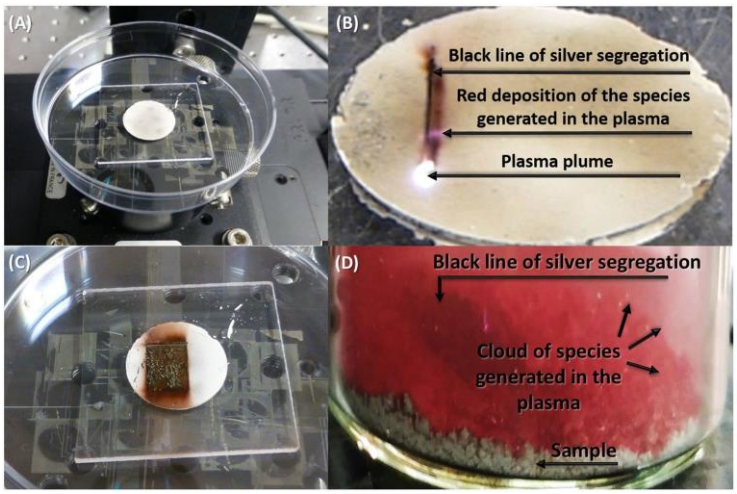

Figure 1. Photographs of sample (**A**) before, (**B**) during, and (**C**) after the laser irradiation process. (**D**) Detail of the cloud of species generated in the plasma.

Fig. 2A depicts a low-magnification HR-TEM image of the regions obtained from the black line acquired in protocol I. Two different types of microstructures can be observed: spherical nanoparticles (Fig. 2B and C), which can be isolated or agglomerated, and nanorods sputtered from the sample (Fig. 2D). Additionally, in Fig. 2E it can be seen that there was a release of nanoparticles in specific regions of the α-Ag_2WO_4 nanorod.

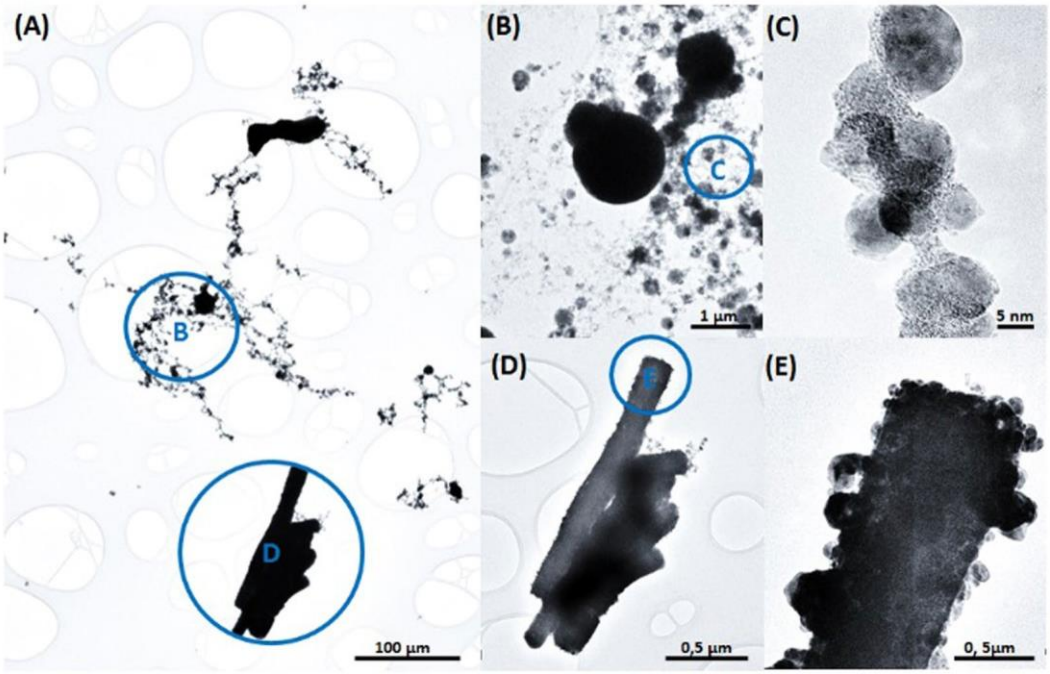

Figure 2. (**A**) Sample irradiated with a femtosecond pulsed laser beam (black part of the sample); (**B**–**C**) Magnification of spherical nanoparticles formed by laser; (**D**–**E**) Magnification of nanorods containing nanoparticles on the surface.

EDS analysis was performed on the irradiated sample (Fig. 3). In Fig. 3A, spherical nanoparticles are observed on the surface of a nanorod. EDS analysis of these nanospheres shows only the presence of Ag (100 at % Ag), whereas Ag and W (atomic percentage ratio Ag/W = 0.068) are observed in the center of the nanorod. The last atomic percentage ratio, less than 2, reveals that there has been a reduction of Ag+ to Ag0 and, thus, metallic silver has been segregated on the tungstate surface. Therefore, the formula of the nanorod becomes α-$Ag_{2-x}WO_{4-\delta}$.

As can be observed in Fig. 3B and C, most of the spherical nanoparticles are agglomerated and they exhibit a crystalline structure. The surface of these spherical nanoparticles is very smooth, with sharp clear edges, which indicates a single-crystalline nature. This is confirmed by the reciprocal distances with the stronger reflections corresponding to lattice planes (200) and (111), which matches cubic Ag, according to the JCPDS database (PDF

65-287). These results suggest a strong decomposition of α-Ag_2WO_4 and the reduction of Ag+ to Ag0 under laser irradiation.

Figure 3. (**A**) HR-TEM image of the α-Ag_2WO_4 sample irradiated by laser and EDS analysis of rods and NPs; (**B**) and (**C**) detail of the Ag NPs formed; I, II, III and IV crystallographic planes of Ag NPs.

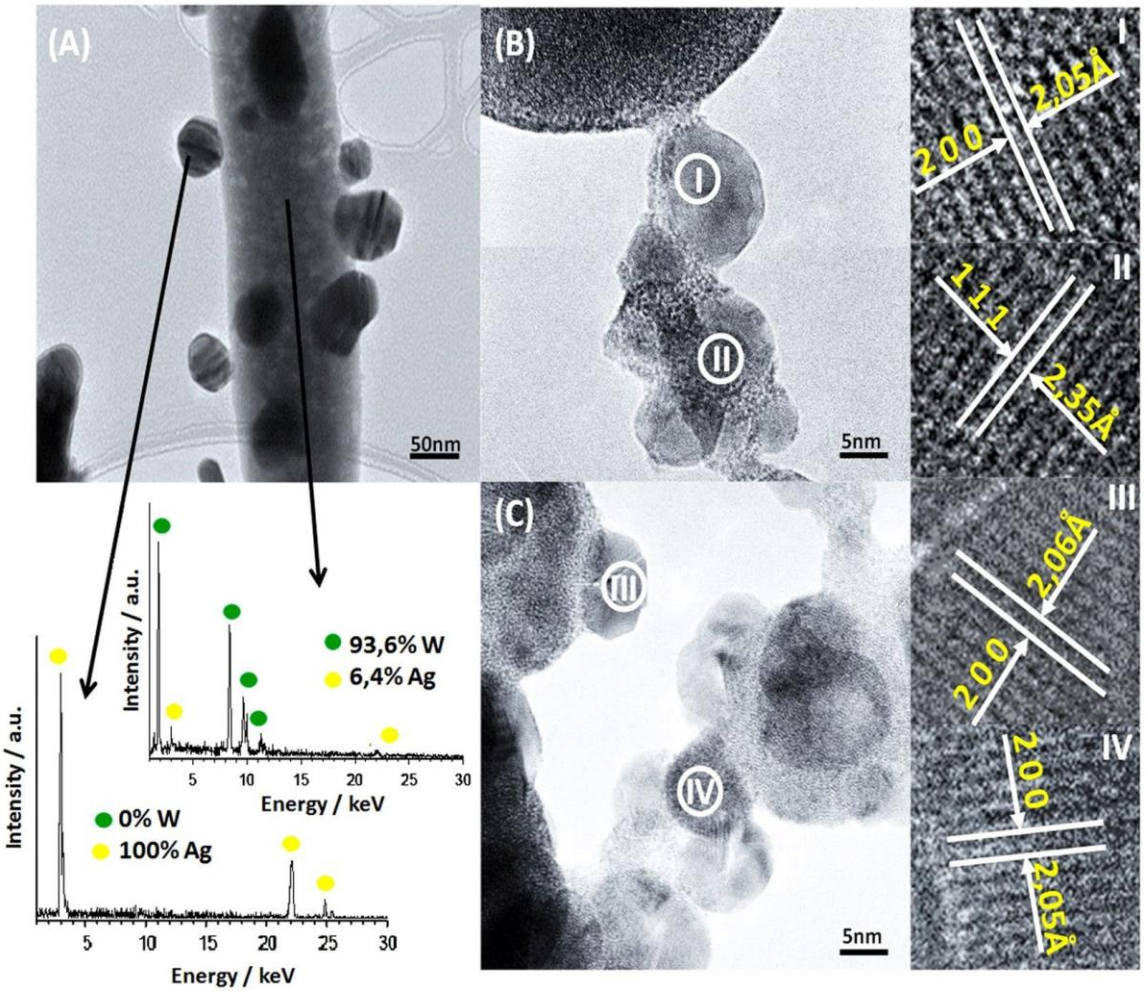

Next, it is important to focus attention on the species that form the red cloud produced by the plasma plume, the species that effectively leave the material's surface. To analyze these species, we collect them directly from the red cloud. The morphology of the collected material is shown in Fig. 4A and a compositional analysis of single particles by EDS is indicated in Fig. 4B. All the particles that form the red cloud are spherical and with a particle size of less than 10 nm. They contain Ag, W and O with different stoichiometry, the formula for which can be denoted as $Ag_xW_yO_z$ due to the non-homogeneity of this material.

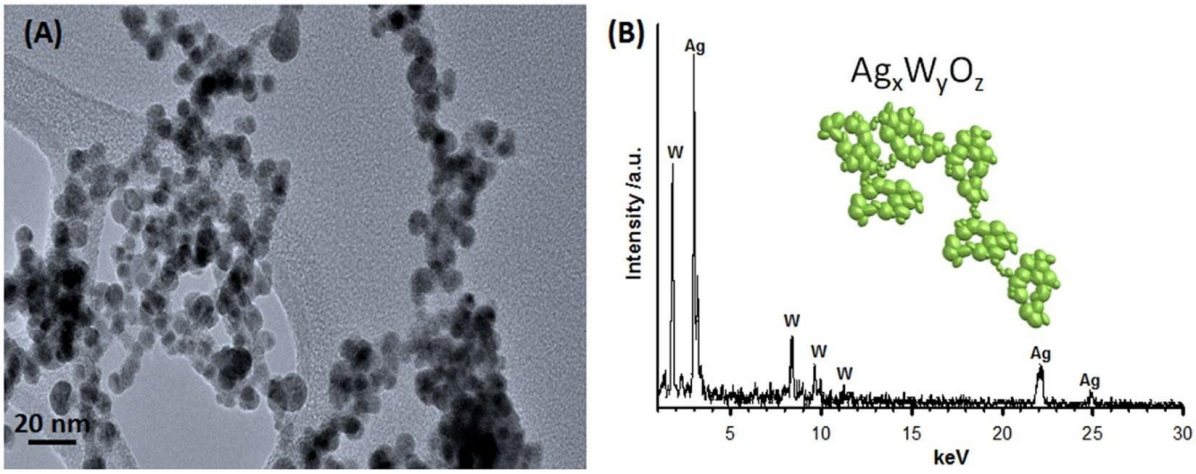

Figure 4. **(A)** Higher magnification HR-TEM micrographs of the particles contained in the plasma (red region); **(B)** EDS analysis of these particles ($Ag_xW_yO_z$). Note that the oxygen signal is not included in the figure

In protocol II, at a lower irradiation fluence regimen, there is no observable ablation plume and only a clear black line in the irradiation zone can be distinguished. The species found here don't show any appreciable differences from the species coming from the black line in protocol I. Consequently, when only the formation of Ag nanoparticles on α-Ag_2WO_4 is desired, low energies or high irradiation speeds can be employed and Ag segregation can be optimized.

Next, it is important to compare the results obtained when α-Ag_2WO_4 crystals were irradiated by laser with those observed when these samples were irradiated with an electron beam in the TEM under a high vacuum[17,26]. In the latter, the formation of Ag filaments on the surface of α-Ag_2WO_4 is identified, and the crystalline structure of α-Ag_2WO_4 remains unchanged. So, there are differences between these two processes. To clarify them, Fig. 5A shows an α-Ag_2WO_4 sample irradiated by laser followed by subjecting it to irradiation with an electron beam for a short time (5 min average). The Ag produced by laser irradiation presents a spherical morphology on the surface of the semiconductor and these spheres do not grow with the time of electron exposure (Fig. 5B). Conversely, in the regions of the sample without previous Ag segregation, the formation of Ag filaments on the surface is observed, due to the irradiation by the electron beam (Fig. 5C). EDS confirmed that both nanostructures contain only metallic Ag (see Fig. 5D). To see the growth of the filament in detail, the reader is directed to Fig. S1 of Supplementary Material.

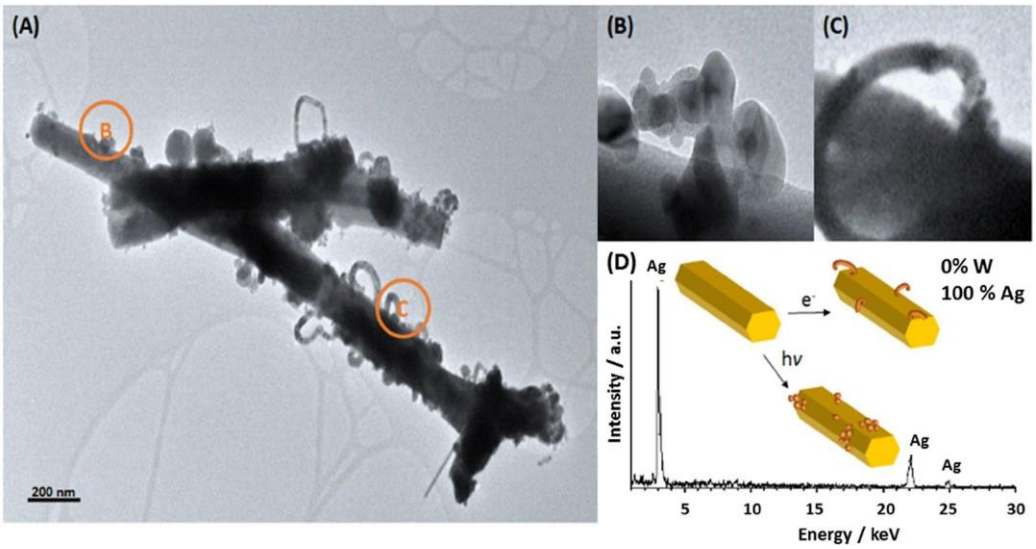

Figure 5. (**A**) HR-TEM image of the α-Ag_2WO_4 sample irradiated by laser followed by subjecting it to irradiation with an electron beam; (**B**) Ag NPs formed by laser irradiation; (**C**) Ag NPs formed by electron beam irradiation; (**D**) EDS analysis results of spherical Ag NPs and the Ag filaments which show the scheme for obtaining the different Ag NPs.

The complete mechanism of the interaction between short pulsed laser radiation and matter is rather com- plicated. The energy of the laser pulse is absorbed by the electrons on the sample's surface, which is a practically instantaneous process. The consequently excitation of electrons contrast with the electrons in the lattice that are in a basal state, and this excitation gradient leads to an equilibrium that is reached through rapid electron-phonon interactions as well as electron diffusion out of the excited region. At the point when the lattice excitation is high enough, ablation may occur. In the case of the electron irradiation, the Ag nanoparticles grow in sequential steps, suffering changes in size and shape along irradiation, due to the presence of electrons on conduction band. This leads to a particle segregation process that is associated to a kinetic energy exchange.

In sum, when we irradiate the sample first with the laser and later with the electron beam, the main information that we can extract is the following: i) both mechanisms allow the segregation of Ag, ii) the nanoparticles obtained with the laser are spherical, while the segregation of Ag in the electron beam promotes the formation of filaments, and iii) in the places where the nanoparticles have already been segregated by the laser, there is no longer any segregation by the electron beam.

X-ray diffraction (XRD) was also performed to analyze the differences between femtosecond laser irradiated material and non-laser irradiated material (Fig. S2 in the Supplementary Material). A small displacement of the peaks in the X-ray pattern of the laser irradiated material occurs, which indicates that there has been a shift in the distance between

the planes of the lattice, thereby distorting the original structure without any extra peaks appearing. The Ag NPs formed by the process cannot be observed using XRD in the powder technique, although it is evidenced in the HR-TEM measurements.

Bactericidal Behavior. A comparison of bactericidal activity against MRSA was performed between non-treated samples of α-Ag_2WO_4, and α-Ag_2WO_4 treated with laser radiation.

The bactericidal activity of materials should lead to complete inhibition of the growth of a particular bacteria or fungus. The minimal inhibitory concentration (MIC) of the samples was measured by exposing planktonic MRSA cells, previously incubated in a 96-well microtiter plate for 24 hrs at 37 °C, to a series of dilutions of α-Ag_2WO_4 non-treated and laser-treated samples in tryptic soy broth (TSB) (from 1000 to 1.95 µg/mL). Pure TSB mixed with MRSA was used as a control, and the lowest concentration of α-Ag_2WO_4 where there was no visible bacteria growth was considered as the MIC. Fig. 6 shows a difference in the bacteria growth colony after coming into contact with non-irradiated and irradiated α-Ag_2WO_4 samples. The results demonstrate that, while the non-irradiated material shows a MIC at 125 µg/mL, when the mate- rial is irradiated with laser radiation, there is a 32-fold improvement in MIC for 3.91 µg/mL over non-treated samples. Moreover, studies performed by irradiating with an electron beam report a MIC magnification of only about 4 times for 31 µg/mL[45].

The literature indicates that the improvement is due to the formation of Ag NPs on the surface of α-Ag_2WO_4, which, in accordance with several studies, present an excellent bactericidal activity against various microorganisms[46–49]. The difference between electron beam-treated samples and laser radiation-treated samples may be due to the amount and/or the morphology of Ag segregated by each treatment. While electron beam treatment is limited to TEM processing, growing Ag with a non-specific morphology, laser irradiation treatment allows the segregation of spherical NPs of Ag in large areas of α-Ag_2WO_4.

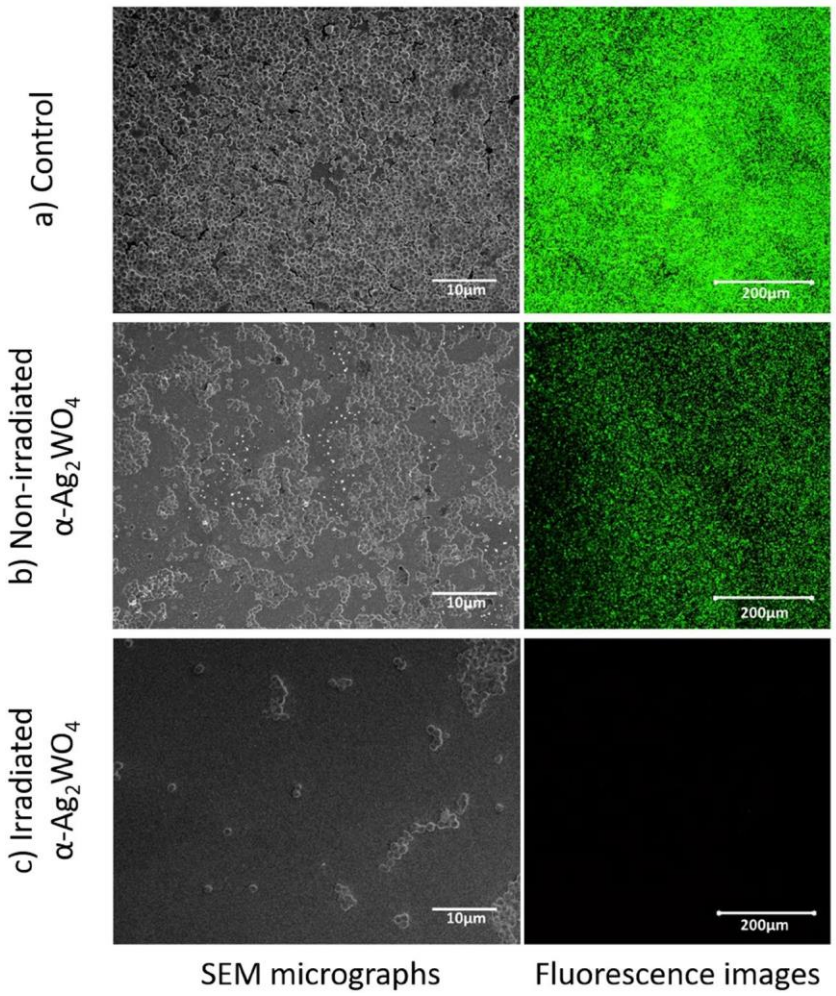

Figure 6. SEM micrographs and fluorescence images of (**A**) pure planktonic culture of MRSA, (**B**) MRSA culture after coming into contact with 125 µg/mL of non-treated α-Ag_2WO_4, and (**C**) MRSA culture after coming into contact with 3.91 µg/mL of α-Ag_2WO_4 irradiated with laser radiation.

Discussion

To gain a better understanding of the resultant species it is important to associate their growth to energy-dependent effects. α-Ag_2WO_4 is a semiconductor with a band gap of 3.1 eV, i.e., 400 nm, which cannot be activated by visible light[50]. From detailed experimental and theoretical studies, it is well established that their orthorhombic structure can be described by the local coordination of both W and Ag cations, i.e., ($[AgO_y]_{\ y}$ = 2, 4, 6, and 7): angular [AgO_2], tetrahedral [AgO_4], octahedral [AgO_6], pentagonal bipyramid [AgO_7], and [WO_6] clusters[2,23–25]. These clusters are intrinsically disordered, and the Ag-O and W-O bonds, as well as the O-Ag-O and O-W-O bond angles, are free to stretch/shorten and bend, respectively, as shown in Fig. 7. This could affect the crystal field and change the dipole and electronic band structures of both the valence band (VB) and the conduction band (CB), thereby influencing the behaviors

of photogenerated charge carriers, including the excitation processes[2,14,21].

When the sample is exposed to sub-picosecond pulsed laser irradiation, the laser radiation is delivered to the surface of the material finding it in a stationary state, which means that there are no interatomic movements and external electrons of atoms in the surface of the material can absorb incoming photons, thereby yielding a photo-activation process. The excess of energy in the electrons would lead to an energetic jump to a metastable excited state, and considering that in sub-picosecond laser pulses a large population of photons is interacting with the excited electrons in a shorter time than that required by electrons to return to the basal state, one of the possibilities that can occur is that electrons experience multiphoton absorption, leading to the expulsion of electrons out of the atom's structure and the laser-matter interaction would be limited to these effects or further effects would be observed, depending on the laser fluence that is applied.

Electrons that belong to structural defects in the lattice require a low energy to be detached from the crystal network. The detachment of electrons leads to the formation of an exciton, and the non-equilibrium carriers (electron–hole pairs) couple with the lattice system temporally and spatially, finally transferring most of their energy to the lattice. As a result, the system tries to recover equilibrium by distributing the excess of energy between carriers and lattices, leading to the segregation of the constituent elements such as Ag, W or O. The segregation of Ag from the constituent clusters is considered to be easier, due to the clusters containing Ag are located at the exterior places of the crystalline lattice[2]. Therefore, the clusters that should receive more energy from the incoming laser radiation and consequently being forced to leave the crystal network in a faster way are the Ag clusters, the clusters that are located at the surface of the crystals.

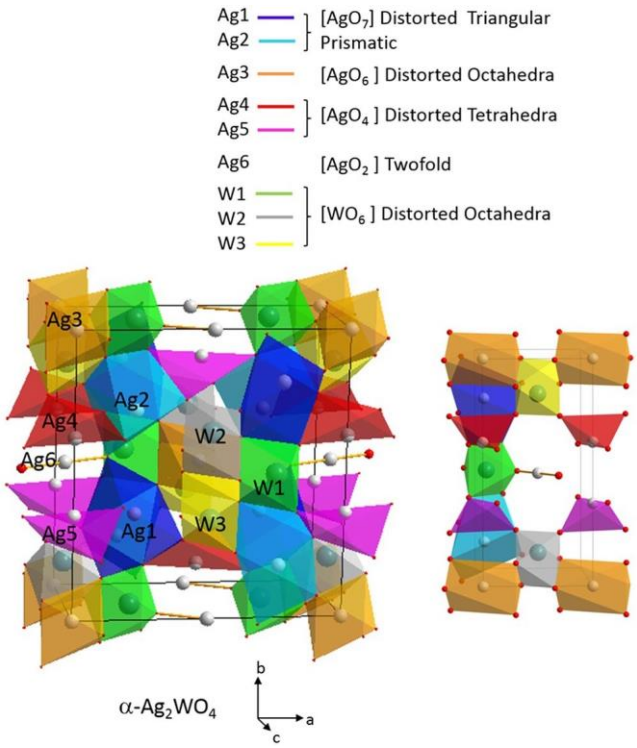

Figure 7. α-Ag_2WO_4 crystal structure.

In consequence, the area subjected to the laser radiation where the departure of Ag takes place presents a large number of Ag vacancies, resulting in the transformation from an n-type to a p-type semiconductor. This could be attributed to the laser-induced formation of internal defects, enhancing the transfer and separation of photo- generated electron-hole pairs.

When the material undergoes a higher laser fluence, a large number of electrons are pulled out of the material's surface, thus forming an electronic cloud. This effect causes the remaining ions to leave the surface of the materials by electromagnetic attraction or inelastic collisions[51,52]. The cloud formed by hot electrons, ions and some other detached species form a plasma known as plasma plume, the life-time of which is in the order of nanoseconds[53]. After the plasma plume is extinguished, the excess energy is released into the surrounding medium and the surface of the sample. Some of the elements forming the plasma are expelled into the surrounding medium and others are projected onto the surface of the sample. Ag, W and O elements experience an instantaneous nucleation leading to the formation of spherical NPs of Ag, and spherical NPs of a mixture of Ag, W and O, the shape taking on a spherical form due to this being the minimum energy shape for nanocrystals. Additionally, some elements do not have enough time to leave the α-Ag_2WO_4 network completely and form spheres attached to the surface of the sample. The lack of time may lead to a lack of energy, thereby promoting an effect that is similar to the one observed at low laser fluences.

When the sample undergoes the irradiation of an electron beam, the formation of Ag filaments takes 5 min at an energy of 10 kV. According to Longo *et al*., during the electron irradiation process, an electronic and structural disorder is introduced into the material through the clusters, which play a major role in the nucleation and growth of Ag filaments[2]. The electrons added to the material by the electron beam are transferred from one cluster to another through the crystal lattice, and Ag formation occurs by reducing clusters [AgO_2] and [AgO_4] in an orderly fashion and, to a lesser extent, through the cluster reduction of [WO_6]. It is proposed that the segregation of Ag atoms by laser irradiation in femtoseconds occurs in a similar way, but in theory faster due to the fact that a femtosecond (10^{-15}s) laser pulse is able to deliver peak power in the region of gigawatts in a shorter time than the conventional electronic relaxation time for most materials (10^{-12}s). Therefore, due to the expected velocity of segregation, the morphology of Ag-segregated NPs tends to be different under electron beam radiation from that obtained when the sample is irradiated with femtosecond laser radiation.

The reasons for conducting this research are manifold and encompass the intellectual excitement of deriving macroscopic performance from molecular-level foundations. The extreme light-matter interaction of femtosecond pulses with α-Ag_2WO_4 has revealed itself as a method to produce silver tungstate nanocomposites in large areas of the sample, which is very interesting from the point of view of scaling up the process. Moreover, our investigation has demonstrated the laser light-driven synthesis of a rich variety of chemical species, which can be summarized as follows:

a) Black species: When the sample is irradiated by the ultrafast laser following protocol I or II. In this case, (spherical) Ag nanoparticles and crystalline Ag clusters are formed on the surface of $Ag_{2-x}WO_{4-\delta}$. We consider that this is a photochemical phenomenon and, therefore, it is not exclusively induced by ultrafast radiation. Moreover, we observed that the new α-$Ag_{2-x}WO_{4-\delta}$ laser composition was stable against electron beam interaction, whereas the regions of the α-Ag_2WO_4 nanorods where Ag° was not generated led to Ag0 nanofilament growth during electron beam irradiation.

b) Red cloud species: When the sample is irradiated by laser following protocol I (only at high fluences). This is a plasma-mediated ablation of the α-Ag_2WO_4 sample, yielding $Ag_xW_yO_z$ nanoparticles. The nanoparticles have been produced due to a multiphoton absorption and the subsequent ionization process.

Furthermore, the bactericidal properties of the laser-irradiated samples increase

dramatically. A 32-fold improvement can be observed compared to the non-laser irradiated material. We believe this work is instructive for the design of nanoparticles on a α-Ag_2WO_4 framework induced by femtosecond laser irradiation. Further efforts in this area are currently underway. In particular, work is being carried out on the tunability of the laser-induced effects by controlling and varying the laser power and the irradiation time, which may open up a new field in the synthesis of novel materials with a broad range of applications.

Methods

α-Ag_2WO_4 powders were prepared according to the co-precipitation procedure described by Longo *et al.*[17]. Powders were also pressed into pellets by a uniaxial press. α-Ag_2WO_4 pellets were irradiated with a Ti:sapphire laser (Femtopower Compact Pro, Femto Lasers) using 30 fs full width at half maximum (FWHM) pulses at the central wavelength of 800 nm, and a repetition rate of 1 kHz. To achieve more precise pulse com- pression at the sample, a programmable acousto-optic filter (DAZZLER, Faslite) was used. A laser beam with a diameter of 6 mm, at the 1/e2 point, and a mean power of 200 mW was focused onto the surface of a target pel- let of α-Ag_2WO_4 with a spherical convex 75 mm lens in order to obtain a focal spot with a diameter of 20.6 μm and in this way achieve a laser fluence of 60 J/cm2, which is a considerably high fluence. The α-Ag_2WO_4 sample was placed at the bottom of a quartz cuvette attached to a two-dimensional motion-controlled stage moving at a constant speed of 0.45 mm/s in the focus plane perpendicular to the laser beam in a stair-like pattern. A scheme of the experimental procedure is shown in Fig. 8, where the results obtained are also presented pictorially, and an irradiation stair-like pattern is depicted in the inset. A complete video of laser-matter interaction can be found in the Supplementary Material.

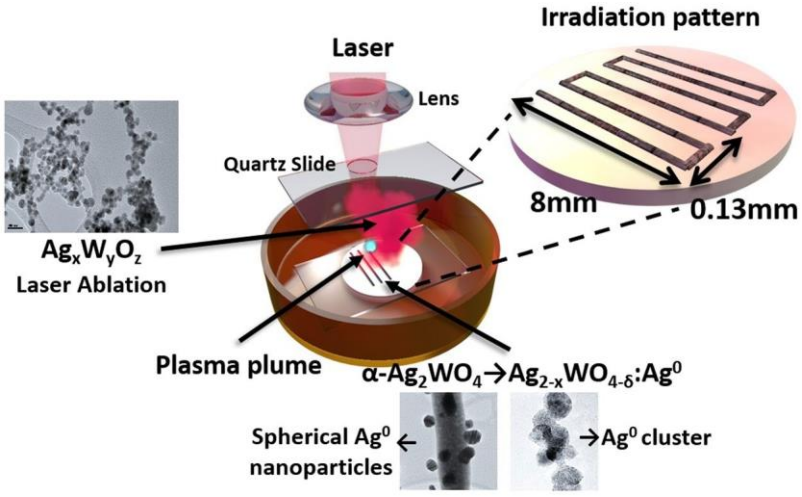

Figure 8. Schematic representation of the experimental procedure, representation of the observed results, and inset showing the representation of the irradiation pattern.

Additional experiments were conducted to better understand the current behavior.

1) In order to spread the energy through a larger irradiation spot in the sample in order to avoid the creation of a plasma plume, the position of the α-Ag_2WO_4 was set 8 mm closer to the convex lens so as to obtain an irradiation spot with a diameter of 84.3 µm, the incoming power was set to 200 mW, and therefore the irradiation laser fluence was 3.6 J/cm2. The highest fluence, obtained at an irradiation spot with a diameter of 20.6 µm, was accompanied by the production of a plasma plume, visible to the naked eye, and the ablation of material. However, when the irradiation spot was set to 84.3 µm the plasma was no longer observed but there was still an explicit interaction between the laser and the α-Ag_2WO_4 as it changed its color to black without material ablation.

2) α-Ag_2WO_4 samples in powder state and deposited in a large vessel were irradiated with 200 mW, matching the focal plane of the lens with the surface of the powder, to obtain an irradiation spot of 20.6 µm, and the vessel was attached to the stage moving at the same constant velocity along the same stair-like pattern. Under these experimental conditions, the black color was still formed over the powder but the species from the ablation plume, light red in color, were collected in the vessel as can be observed in Fig. 1D. To collect the species in the red cloud, a microscope coverslip was located in the path of the laser beam so that the cloud species in the plasma were naturally attached to the coverslip.

To determine the crystallinity of α-Ag_2WO_4 samples before any treatment, a D/Max-2500PC (Rigaku, Japan) diffractometer with Cu Kα 108 radiation (λ = 0.154 nm) was used in a 2θ range from 10° to 70° at a scan velocity of 2°/min with a step of 0.02°. The XRD patterns of the samples indicate an orthorhombic structure with a space group of Pn2n, in agreement with the JCPDS database (PDF34-0061). The lattice parameters were a = 1.082 nm, b = 1.201 nm, and c = 0.59 nm. All the peaks were sharp in nature, indicating a high degree of crystallinity.

To compare the ultrafast laser-irradiated samples with TEM-treated samples, a non-laser irradiated α-Ag_2WO_4 sample was treated by an electron beam using a field-emission scanning electron microscope (model Inspect F50, FEI Company, Hillsboro, OR) at 10 kV for 5, 10, 15 and 20 minutes (see the evolution of the growth of Ag NPs at different times in Figure S1 in the Supplementary Material).

To characterize the structural changes that occurred in the irradiated regions, the laser-irradiated samples were characterized by HR-TEM. This was performed using a Jem-2100

LaB6 (Jeol) HR-TEM with an accelerating voltage of 200 kV coupled with an INCA Energy TEM 200 (Oxford) energy dispersive X-ray spectrometer. The same instrument was used to perform TEM, electron diffraction, and microanalysis measurements to characterize structural changes. Powder samples were prepared by depositing a representative sample of the powder directly onto holed carbon-coated Cu grids, whereas the pellets were prepared by ultramicrotomy. The pellets were embedded in an epoxy resin and sliced at room temperature in an RMC Utracut (Powertome XL model).

References

1. Heyer, O. *et al*. A new multiferroic material: $MnWO_4$. *Journal of Physics: Condensed Matter* **18**, L471 (2006).
2. Andrés, J. *et al*. Structural and electronic analysis of the atomic scale nucleation of Ag on α-Ag_2WO_4 induced by electron irradiation. *Scientific Reports* **4**, 5391 (2014).
3. Janáky, C., Rajeshwar, K., de Tacconi, N. R., Chanmanee, W. & Huda, M. N. Tungsten-based oxide semiconductors for solar hydrogen generation. *Catalysis Today* **199**, 53–64 (2013).
4. McGlone, T., Streb, C., Long, D.-L. & Cronin, L. Assembly of pure silver-tungsten-oxide frameworks from nanostructured solution processable clusters and their evolution into materials with a metallic component. *Advanced Materials.* **22**, 4275–4279 (2010).
5. Chen, H. & Xu, Y. Photoactivity and stability of Ag_2WO_4 for organic degradation in aqueous suspensions. *Applied Surface Science* **319**, 319–323 (2014).
6. Cheng, L., Shao, Q., Shao, M., Wei, X. & Wu, Z. Photoswitches of one-dimensional Ag_2MO_4 (M = Cr, Mo, and W). *The Journal Physical Chemistry C* **113**, 1764–1768 (2009).
7. Zhang, X.-Y., Wang, J.-D., Liu, J.-K., Yang, X.-H. & Lu, Y. Construction of silver tungstate multilevel sphere clusters by controlling the energy distribution on the crystal surface. *CrystEngComm* **17**, 1129–1138 (2015).
8. Vafaeezadeh, M. & Hashemi, M. M. One pot oxidative cleavage of cyclohexene to adipic acid using silver tungstate nano-rods in a bronsted acidic ionic liquid. *RSC Advanced* **5**, 31298–31302 (2015).
9. Ding, Y., Wan, Y., Min, Y.-L., Zhang, W. & Yu, S.-H. General synthesis and phase control of metal molybdate hydrates $MMoO_4$ nH_2O (M = Co, Ni, Mn, n = 0, 3/4, 1) nano/microcrystals by a hydrothermal approach: Magnetic, photocatalytic, and electrochemical properties. *Inorganic Chemistry* **47**, 7813–7823 (2008).
10. Wang, X., Fu, C., Wang, P., Yu, H. & Yu, J. Hierarchically porous metastable β-Ag_2WO_4 hollow nanospheres: controlled synthesis and high photocatalytic activity. *Nanotechnology* **24**, 165602 (2013).
11. Yang, X. *et al*. Fabrication of Ag_3PO_4-graphene composites with highly efficient and stable visible light photocatalytic performance. *ACS Catalysis* **3**, 363–369 (2013).
12. Abdurahman, A., Nizamidin, P. & Yimit, A. Optical and electrochemical gas sensing properties of yttrium–silver co-doped lithium iron phosphate thin films. *Materials Science in Semiconductor Processing* **22**, 21–27 (2014).
13. Moshe, A. B. & Markovich, G. Synthesis of single crystal hollow silver nanoparticles in a fast reaction-diffusion process. *Chemistry of Materials* **23**, 1239–1245 (2011).
14. Cavalcante, L. S. *et al*. Cluster coordination and photoluminescence properties of α-Ag_2WO_4 microcrystals. *Inorganic Chemistry* **51**, 10675–10687 (2012).
15. Longo, V. M. *et al*. Potentiated electron transference in α-Ag_2WO_4 microcrystals with Ag nanofilaments as microbial agent. *The Journal of Physical Chemistry A* **118**, 5769–

5778 (2014).

16. da Silva, L. F. *et al*. novel ozone gas sensor based on one-dimensional (1d) α-Ag_2WO_4 nanostructures. *Nanoscale* **6**, 4058–4062 (2014).
17. Longo, E. *et al*. Toward an understanding of the growth of Ag filaments on α-Ag_2WO_4 and their photoluminescent properties: A combined experimental and theoretical study. *The Journal of Physical Chemistry C* **118**, 1229–1239 (2014).
18. Zhang, R. *et al*. Facile hydrothermal synthesis and photocatalytic activity of rod-like nanosized silver tungstate. *IET Micro Nano Letters* **7**, 1285–1288 (2012).
19. Dutta, D. P., Singh, A., Ballal, A. & Tyagi, A. K. High adsorption capacity for cationic dye removal and antibacterial properties of sonochemically synthesized Ag_2WO_4 nanorods. *Eur. J. Inorganic Chemistry* **2014**, 5724–5732 (2014).
20. Pan, L., Li, L. & Chen, Y. Synthesis and electrocatalytic properties of microsized Ag_2WO_4 and nanoscaled MWO_4 (M = Co, Mn). *Journal of Sol-Gel Science and Technology* **66**, 330–336 (2013).
21. Lin, Z. et al. Electronic reconstruction of α-Ag2WO4 nanorods for visible-light photocatalysis. *ACS Nano* **9**, 7256–7265 (2015).
22. da Silva, L. F. et al. Acetone gas sensor based on α-Ag_2WO_4 nanorods obtained via a microwave-assisted hydrothermal route. *Journal Alloys Compounds* **683**, 186–190 (2016).
23. Longo, E. et al. Direct in situ observation of the electron-driven synthesis of Ag filaments α-Ag_2WO_4 crystals. *Scientific Reports* **3**, 1676 (2013).
24. Pereira, W. S. et al. Elucidating the real-time ag nanoparticle growth on α-Ag_2WO_4 during electron beam irradiation: experimental evidence and theoretical insights. *Physical Chemistry Chemical Physics* **17**, 5352–5359 (2015).
25. San-Miguel, M. A. et al. In situ growth of Ag nanoparticles on α-Ag_2WO_4 under electron irradiation: probing the physical principles. *Nanotechnology* **27**, 225703 (2016).
26. Longo, E. et al. In situ transmission electron microscopy observation of Ag nanocrystal evolution by surfactant free electron-driven synthesis. *Scientific Reports* **6**, 21498 (2016).
27. Shi, G. et al. Electron beam induced growth of silver nanoparticles. *Scanning* **35**, 69–74 (2013).
28. Umalas, M. et al. Electron beam induced growth of silver nanowhiskers. *Journal Crystal Growth* **410**, 63–68 (2015).
29. Pattabi, M., Pattabi, R. M. & Sanjeev, G. Studies on the growth and stability of silver nanoparticles synthesized by electron beam irradiation. *Journal of Materials Science: Materials in Electronics* **20**, 1233 (2009).
30. Li, K. & Zhang, F.-S. A novel approach for preparing silver nanoparticles under electron beam irradiation. *Journal Nanoparticle Research* **12**, 1423–1428 (2010).
31. Mansourian, A., Paknejad, S. A., Zayats, A. V. & Mannan, S. H. Stereoscopic nanoscale-precision growth of free-standing silver nanorods by electron beam irradiation. *The Journal of Physical Chemistry C* **120**, 20310–20314 (2016).
32. Bonse, J., Rosenfeld, A. & Krüger, J. On the role of surface plasmon polaritons in the formation of laser-induced periodic surface structures upon irradiation of silicon by femtosecond-laser pulses. *Journal Applied Physics* **106**, 104910 (2009).
33. Bonse, J., Höhm, S., Rosenfeld, A. & Krüger, J. Sub-100-nm laser-induced periodic surface structures upon irradiation of titanium by Ti:sapphire femtosecond laser pulses in air. *Applied Physics A* **110**, 547–551 (2013).
34. Rebollar, E. et al. Ultraviolet and infrared femtosecond laser induced periodic surface structures on thin polymer films. *Applied Physics Letters* **100**, 041106 (2012).
35. Kaempfe, M., Rainer, T., Berg, K.-J., Seifert, G. & Graener, H. Ultrashort laser pulse induced deformation of silver nanoparticles in glass. *Applied Physics Letters* **74**, 1200–

1202 (1999).

36. Do, J., Fedoruk, M., Jäckel, F. & Feldmann, J. Two-color laser printing of individual gold nanorods. *Nano Letters* **13**, 4164–4168 (2013).
37. Chou, S. S. et al. Laser direct write synthesis of lead halide perovskites. *The Journal of Physical Chemistry Letters* **7**, 3736–3741 (2016).
38. Torres-Mendieta, R. et al. In situ decoration of graphene sheets with gold nanoparticles synthetized by pulsed laser ablation in liquids. *Scientific Reports* **6**, 30478 (2016).
39. Goutaland, F., Sow, M., Ollier, N. & Vocanson, F. Growth of highly concentrated silver nanoparticles and nanoholes in silver- exchanged glass by ultraviolet continuous wave laser exposure. *Optical Materials Express* **2**, 350–357 (2012).
40. Baraldi, G., Gonzalo, J., Solis, J. & Siegel, J. Reorganizing and shaping of embedded near-coalescence silver nanoparticles with off- resonance femtosecond laser pulses. *Nanotechnology* **24**, 255301 (2013).
41. Doster, J. et al. Tailoring the surface plasmon resonance of embedded silver nanoparticles by combining nano- and femtosecond laser pulses. *Applied Physics Letters* **104**, 153106 (2014).
42. Semaltianos, N. G. Nanoparticles by laser ablation. *Critical Reviews in Solid State and Materials Sciences* **35**, 105–124 (2010).
43. Cortie, M. B. & McDonagh, A. M. Synthesis and optical properties of hybrid and alloy plasmonic nanoparticles. *Chemical Rev*iews **111**, 3713–3735 (2011).
44. Zhang, D., Gökce, B. & Barcikowski, S. Laser synthesis and processing of colloids: Fundamentals and applications. *Chemical Rev*iews **117**, 3990–4103 (2017).
45. Longo, V. M. et al. Potentiated electron transference in α-Ag_2WO_4 microcrystals with ag nanofilaments as microbial agent. *The Journal of Physical Chemistry A* **118**, 5769–5778 (2014).
46. Feng, Q. L. et al. A mechanistic study of the antibacterial effect of silver ions on escherichia coli and staphylococcus aureus. *Journal Biomedical Materials Research* **52**, 662–668 (2000).
47. Ruparelia, J. P., Chatterjee, A. K., Duttagupta, S. P. & Mukherji, S. Strain specificity in antimicrobial activity of silver and copper nanoparticles. *Acta Biomaterialia* **4**, 707–716 (2008).
48. Panáček, A. et al. Silver colloid nanoparticles: Synthesis, characterization, and their antibacterial activity. *The Journal of Physical Chemistry B* **110**, 16248–16253 (2006).
49. Sotiriou, G. A. et al. Nanosilver on nanostructured silica: Antibacterial activity and ag surface area. *Chemical Engineering Journal* **170**, 547–554 (2011).
50. Gallais, L. et al. Transient interference implications on the subpicosecond laser damage of multidielectrics. *Applied Physics Letters.* **97**, 051112 (2010).
51. Correa, D. S. et al. Ultrafast laser pulses for structuring materials at micro/nano scale: From waveguides to superhydrophobic surfaces. *Photonics* **4**, 8 (2017).
52. Stoian, R., Ashkenasi, D., Rosenfeld, A. & Campbell, E. E. B. Coulomb explosion in ultrashort pulsed laser ablation of Al_2O_3. *Physical Review B* 62, 13167–13173 (2000).
53. Joglekar, A. P., Liu, H.-h., Meyhöfer, E., Mourou, G. & Hunt, A. J. Optics at critical intensity: Applications to nanomorphing. *PNAS* **101**, 5856–5861 (2003).

2.2 – Ag Nanoparticles/α-Ag_2WO_4 Composite Formed by Electron Beam and Femtosecond Irradiation as Potent Antifungal and Antitumor Agents

www.nature.com/scientificreports

SCIENTIFIC REPORTS

OPEN

Received: 28 November 2018
Accepted: 20 June 2019
Published online: 09 July 2019

Ag Nanoparticles/α-Ag_2WO_4 Composite Formed by Electron Beam and Femtosecond Irradiation as Potent Antifungal and Antitumor Agents

M. Assis[1], T. Robeldo[2], C. C. Foggi[1], A. M. Kubo[1], G. Mínguez-Vega[3], E. Condoncillo[4], H. Beltran-Mir[4], R. Torres-Mendieta[5], J. Andrés[6], M. Oliva[6], C. E. Vergani[7], P. A. Barbugli[7], E. R. Camargo[1], R. C. Borra[2] & E. Longo[1]

The ability to manipulate the structure and function of promising systems via external stimuli is emerging with the development of reconfigurable and programmable multifunctional materials. Increasing antifungal and antitumor activity requires novel, effective treatments to be diligently sought. In this work, the synthesis, characterization, and *in vitro* biological screening of pure α-Ag_2WO_4, irradiated with electrons and with non-focused and focused femtosecond laser beams are reported. We demonstrate, for the first time, that Ag nanoparticles/α-Ag_2WO_4 composite displays potent antifungal and antitumor activity. This composite had an extreme low inhibition concentration against *Candida albicans*, cause the modulation of α-Ag_2WO_4 perform the fungicidal activity more efficient. For tumor activity, it was found that the composite showed a high selectivity against the cancer cells (MB49), thus depleting the populations of cancer cells by necrosis and apoptosis, without the healthy cells (BALB/3T3) being affected.

Ag Nanoparticles/α-Ag_2WO_4 Composite Formed by Electron Beam and Femtosecond Irradiation as Potent Antifungal and Antitumor Agents

Marcelo Assis[1], T. Robeldo[2], C. C. Foggi[1], A. M. Kubo[1], G. Mínguez-Vega[3], E. Condoncillo[4], H. Beltran-Mir[4], R. Torres-Mendieta[5], J. Andrés[6], M. Oliva[6], C. E. Vergani[7], P. A. Barbugli[7], E. R. Camargo[1], R. C. Borra[2] & E. Longo[1]

[1]CDMF, LIEC, Chemistry Department of the Federal University of São Carlos - (UFSCar), P.O. Box 676, 13565-905, São Carlos, SP, Brazil.

[2]LIA, Laboratory of Applied Immunology, Department of Genetics and Evolution, Federal University of São Carlos - (UFSCar), São Carlos, Brazil.

[3]GROC·UJI, Institut de Noves Tecnologies de la Imatge (INIT, University Jaume I (UJI), Castelló, 12071, Spain.

[4]Department of Inorganic and Organic Chemistry, University Jaume I (UJI), Castelló, 12071, Spain.

[5]Institute for Nanomaterials, Advanced Technologies and Innovation, Technical University of Liberec, Studentská 1402/2, 461 17, Liberec, Czech Republic.

[6]Department of Analytical and Physical Chemistry, University Jaume I (UJI), Castelló, 12071, Spain.

[7]São Paulo State University (UNESP), Department of Dental Materials and Prosthodontics, School of Dentistry at Araraquara, Rua Humaitá, 1680, 14801-903, Araraquara, SP, Brazil.

The ability to manipulate the structure and function of promising systems via external stimuli is emerging with the development of reconfigurable and programmable multifunctional materials. Increasing antifungal and antitumor activity requires novel, effective treatments to be diligently sought. In this work, the synthesis, characterization, and in vitro biological screening of pure α-Ag_2WO_4, irradiated with electrons and with non-focused and focused femtosecond laser beams are reported. We demonstrate, for the first time, that Ag nanoparticles/α-Ag_2WO_4 composite displays potent antifungal and antitumor activity. This composite had an extreme low inhibition concentration against *Candida albicans*, cause the modulation of α-Ag_2WO_4 perform the fungicidal activity more efficient. For tumor activity, it was found that the composite showed a high selectivity against the cancer cells (MB49), thus depleting the populations of cancer cells by necrosis and apoptosis, without the healthy cells (BALB/3T3) being affected.

Introduction

Silver nanoparticles (Ag NPs), are considered one of the most important members of the noble metal NPs family. The ever-increasing research activity around them relies on their

unique physical, chemical, and biological properties toward applications in catalysis for reduction, oxidation, and oxidative coupling reactions[1–3], air and water purification systems[4–6], development of consumer products (e.g., cosmetics, paints, laundry detergents, toys, accessories, and a variety of household applications)[7,8], and fabrication of sensing devices[9,10]. Moreover, they exhibit diverse useful bioactivities for healthcare[11–13], antiviral properties[14,15], bactericidal behavior[16,17], anti- fungal activity[18], as high antimicrobial agent against yeasts, molds, Gram-positive and Gram-negative bacteria[19–23], anti-cancer[24–26], and anti-inflammatory effects[27]. Recently, Chernousova and Epple[17] reviewed the state of research on the effects of Ag on bacteria, cells, and higher organisms, which has shown promising results. However, apart from its outstanding single-NP behavior, its hybridization with semiconductors is also leading to unprecedented behaviors and features that have now paved the way toward promising applications in many fields[28–30].

The development and use of hybrid nanomaterials, composed by a noble metal–semiconductor, i.e., NPs of Ag, Au, or Pt deposited on a semiconductor surface, have led to advantageous features related to surface plasmon resonance effects, a Schottky contact additional active sites and/or presence of electronics traps[31–33], that in the end are used to enhance localized heating in living systems, wich may find potential applications in thermal ablation therapies or drug delivery mechanisms[34].

In this context, a highly attractive semiconductor for its photochemical activity is α-Ag_2WO_4. This is an n-type semiconductor with a band gap value of 3.1 eV (400 nm)[34–36] which has been widely exploited in applications such as visible-light photocatalysis for the degradation of organic dyes and aromatic organic compounds[37–40], as well as ozone and acetone gas sensing[41,42]. Ag NPs on the semiconductor's surface could enhance the surface plasmon resonance effect, which might improve the separation rate of the photo-generated holes and electrons in the composite, leading to augmented photo-derived phenomena. Therefore, developing a metal–semiconductor junction of Ag/Ag_2WO_4 in a controllable way would represent a wise strategy that may have significant potential for the design of novel materials[43].

The great potential for growing Ag NPs on the framework of semiconductors, induced by electron beam irradiation, is well known[44–46]. Recently, our research group demonstrated that the exposure to electron or femto- second (fs) laser beams can give rise to many fascinating and unexpected phenomena, such as the formation and growth process of Ag NPs on α-Ag_2WO_4 crystals[34,47–52] with a wide range of applications, including microbial[53,54] and antifungal[55] agents. Very recently, we demonstrated that the interaction between pulsed fs laser irradiation and α-Ag_2WO_4 revealed a new processing alternative for the formation of Ag NPs on α-

Ag_2WO_4 with bactericidal properties[36]. From a medical point of view, the development of novel composites as antimicrobials is very attractive, owing to the worldwide crisis of bacterial resistance to conventional, narrow-target antibiotics.

Taking into consideration its afore mentioned biological relevance, the synthesis of Ag NPs/α-Ag_2WO_4 composite by electron beam and fs irradiation was undertaken and a systematic study of its antifungal and antitumor activities was carried out in order to analyze the beneficial implications of the composite in two of the most important bio-medical applications (as an antitumor and antifungal agent) that directly impact the healthcare of human kind.

Results

Structural analysis. Four samples were studied: pure α-Ag_2WO_4, a composite irradiated with electrons (Ag NPs/α-Ag_2WO_4:E), a composite irradiated by a fs laser beam under non-focused conditions (Ag NPs/α- Ag_2WO_4:NF), and a composite irradiated by a fs laser beam under focused conditions (Ag NPs/α-Ag_2WO_4:F).

Fig. 1A shows the X-ray diffraction (XRD) patterns of the samples to evaluate the crystalline order/disorder at long distances. The samples present an orthorhombic structure with a space group of *Pn2n* and eight molecules per unit cell (Z = 8), according to the crystallographic data sheet n° 2489692 in the Inorganic Crystal Structure Database (ICSD). The lattice parameters are: a = 10.878 Å, b = 12.009 Å, and c = 5.89 Å. Figure 1B shows the most intense diffraction peak (231), which was shifted slightly to higher values of 2θ for all composites. This behavior is also observed for the (002) and (400) peaks of Ag NPs/Ag_2WO_4:E composite, and the (002), (400) and (313) peaks of Ag NPs/Ag_2WO_4:F composite (Fig. 1C). Another phenomenon that occurs is the suppression of certain peaks in relation to the non-irradiated phase. For all composite, the (303) peak is not observed, whereas for the Ag NPs/ Ag_2WO_4:F composite, the peak (301) does not appear (Fig. 1B).

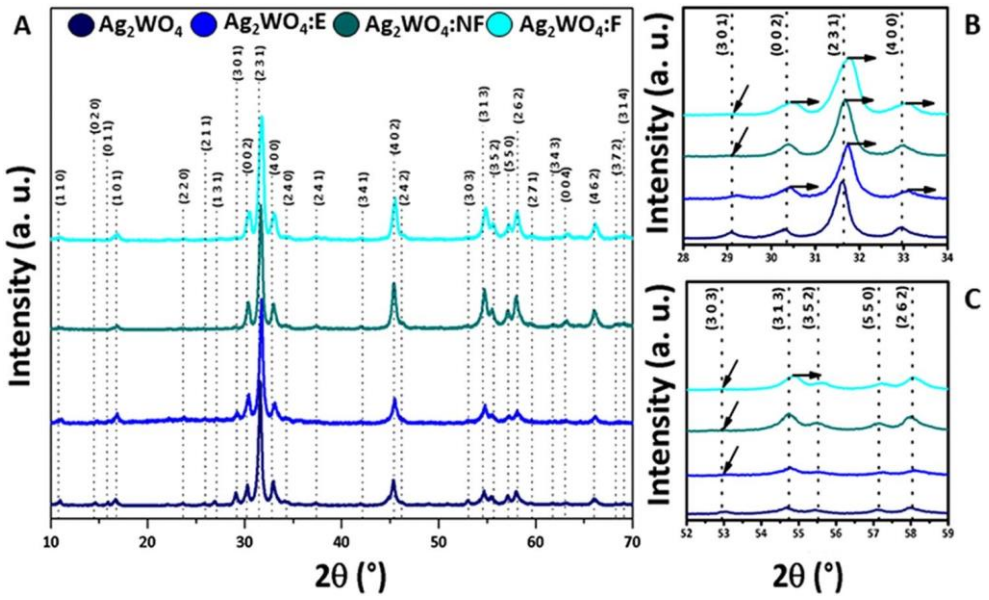

Figure 1. (**A**) X-ray diffractograms of the α-Ag_2WO_4 samples before and after the different irradiations; (**B**) Approximation of the diffracted region between 28 and 34° and (**C**) Approximation of the diffracted region between 52 and 59°.

Micro-Raman spectroscopy analysis, as shown in Fig. 2, was performed to determine the short-range structural order/disorder effects, and is thus a structural complementary technique to XRD. α-Ag_2WO_4 belongs to the C_{2v} symmetry group; its structure is composed by four different clusters associated with the local coordination of Ag: [AgO_2], [AgO_4], [AgO_6], and [AgO_7], and only one cluster of W: [WO_6]. The active Raman modes are observed at 80, 104, 324, 668, 769, and 875 cm^{-1} (Fig. 2A). The modes located at lower wavelengths, 80 and 104 cm^{-1}, can be associated to a transition A_{1g} of the crystal lattice modes of Ag[53,56] that do not undergo changes, even for samples irradiated by laser and electrons. The other modes correspond to movements of the [WO_6] cluster, the values 875 cm^{-1} and 769 cm^{-1} are associated with the A_{2g} and A_{1g} vibrational modes of the symmetric and asymmetric stretching modes of O-W-O, respectively[53,56,57]. The B_{1g} mode of 668 cm^{-1} was related to stretching modes of the W-O bond and the A_{2g} mode at 324 cm^{-1} was attributed to cationic lattice vibrations[57]. It is observed that both Ag NPs/α-Ag_2WO_4:E and Ag NPs/α-Ag_2WO_4:NF composites do not present significant changes, whereas for the Ag NPs/α-Ag_2WO_4:F composite, the defined peaks at 668 and 769 cm^{-1} disappear, thus presenting a higher structural disorder at short-range than the other composites (Fig. 2B).

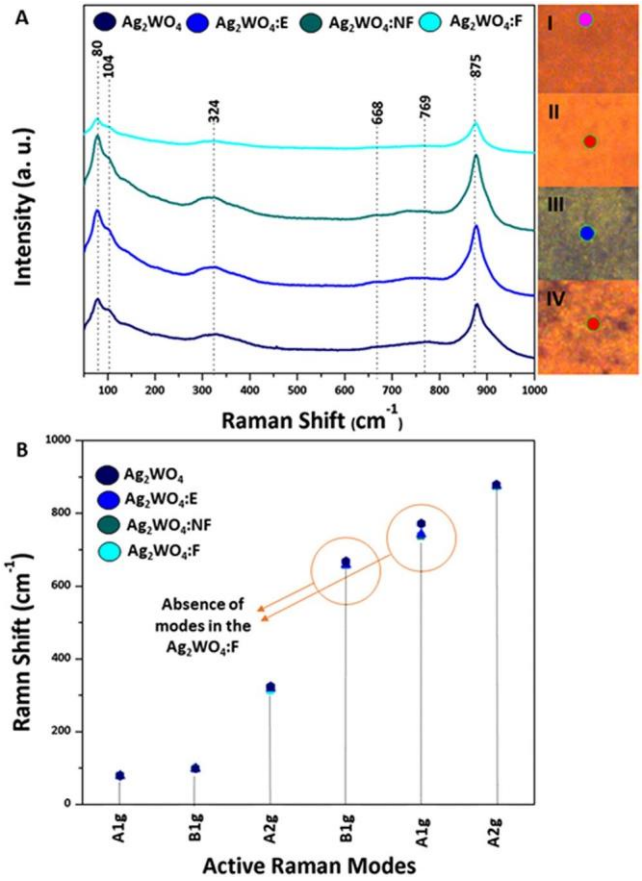

Figure 2. Micro-Raman spectra of α-Ag_2WO_4 samples before and after the different irradiations with the respective regions in the sample (I–iv); (**B**) Comparison between relative positions of experimental Raman- active modes for the samples.

Fig. 3 presents images of the samples obtained by field emission scanning electron microscopy (FE-SEM). In the α-Ag_2WO_4 sample (Fig. 3A), the formation of Ag NPs was not observed because the system was not disturbed by any external energy source. For Ag NPs/α-Ag_2WO_4:E composite (Fig. 3B), it is possible to observe the delocalized formation of Ag NPs, as reported by Longo *et al.*[34]. Fig. 3C, D display the images of Ag NPs/α-Ag_2WO_4:NF and Ag NPs/α-Ag_2WO_4:F composite, respectively. In the Ag NPs/α-Ag_2WO_4:NF composite, there is a small number of Ag NPs attached to the semiconductor's surface (similar to Ag NPs/α-Ag_2WO_4:E composite) and a slight sinterization of α-Ag_2WO_4 microrods, whereas the Ag NPs/α-Ag_2WO_4:F composite presents many spherical Ag NPs with a larger particle size than in α-Ag_2WO_4:NF, probably due to an enhancement of the sinterization process experienced by α-Ag_2WO_4 microrods, as was observed by Andrés *et al.*[34].

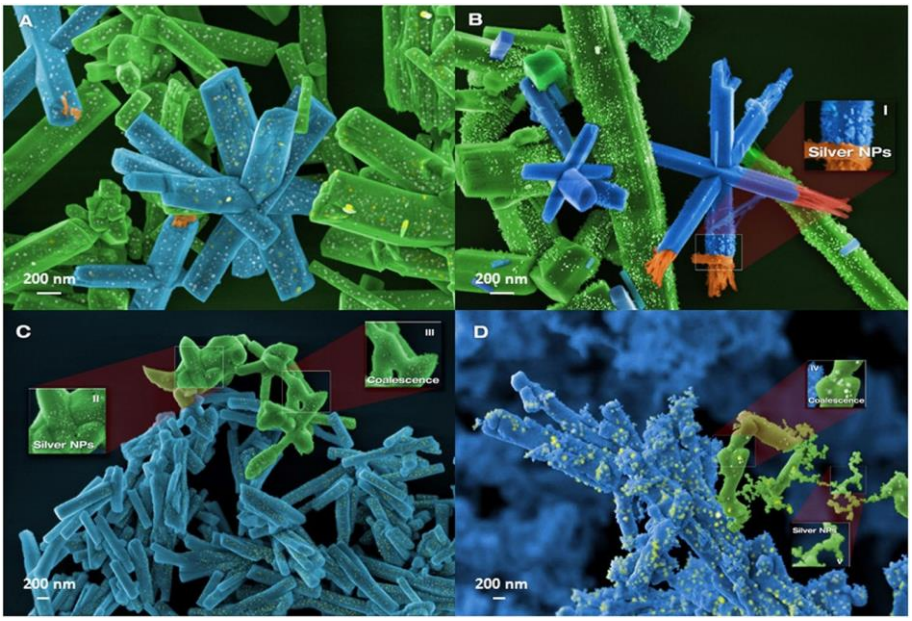

Figure 3. FE-SEM images for (**A**) α-Ag_2WO_4; (**B**) α-Ag_2WO_4:E (**C**) α-Ag_2WO_4:NF; (**D**) α-Ag_2WO_4:F.

All materials have a normal size distribution, and the obtained sizes of width and length for the samples are of 0.31 ± 0.02 μm and 2.76 ± 0.88 μm, 0.33 ± 0.03 μm and 2.83 ± 0.62 μm, 0.33 ± 0.11 μm and 2.32 ± 1.2 μm, 0.36 ± 0.13 μm and 2.54 ± 0.95 μm for Ag_2WO_4, Ag_2WO_4:E, Ag_2WO_4:NF and Ag_2WO_4:F respectively. The increase in the error of the samples irradiated with the laser in femtoseconds, is due to the sinterization of some rods of α-Ag_2WO_4, as shown in the Fig. 3C, D.

Antifungal activity. The antifungal activity of the samples was evaluated against the biofilm formation of the *Candida albicans* ATCC 90028 reference strain. The minimum obtained inhibitory concentration (MIC) and minimum fungicidal concentration (MFC) values are presented in the Fig. 4A. The results obtained by counting colony forming units per mL (CFU.mL−1) show that the most effective samples were, in descending order: Ag NPs/α-Ag_2WO_4:F, Ag NPs/α-Ag_2WO_4:NF, Ag NPs/α-Ag_2WO_4:E, and α-Ag_2WO_4. The highest concentration used for the tests was 125.00 μg/mL and we observe that all irradiated materials have antifungal activity. Even at sub-inhibitory concentrations, the reduction in the number of

viable fungal colonies is observed in relation to the control. A dose-dependent effect was observed.

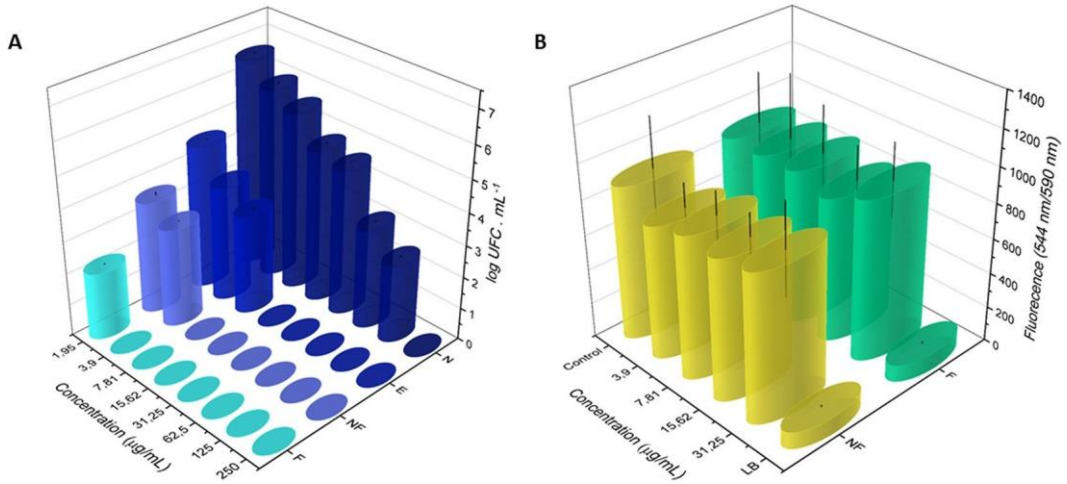

Figure 4. *Candida albicans* (**A**) and FGH (**B**) growth as a function of different concentrations of samples.

Four concentrations of Ag NPs/α-Ag_2WO_4:NF and Ag NPs/α-Ag_2WO_4:F composites were studied on a human gingival fibroblasts (FGH) cell line, because this exhibiting better fungicidal activity. After 24 h of incubation, the effects of these composites on cell viability, cell proliferation, and cell morphology were evaluated by the resazurin assay (Alamar Blue) quantitative fluorimetric assay (Fig. 4B), confocal laser scanning microscopy (CLSM) (Fig. 5), and SEM (Fig. 6), respectively. The studied concentrations were 31.25, 15.62, 7.81, and 3.90 µg/ mL, respectively, because they are above the optimum range of fungicidal activity of the materials. The results show no statistically significant loss of cell viability for these concentrations compared to the control (CT), which shows a contrasting behavior with respect to cell death control treated with Triton-X 100 0.9% buffer (LB) (see Fig. 4B). The proliferation assay on CLSM by carboxyfluorescein succinimidyl ester and propidium iodide (PI) showed a homogeneous label of CFSE by HGF cells for the concentrations, whereas no important staining with PI was detected. This was very similar to the CT cells, and completely different from the pattern of the fluorescence cells treated with the cell death control (CAM), showing no influence of α-Ag_2WO_4:NF and α-Ag_2WO_4:F mate- rials on HGF cell proliferation (see Figs 5 and 6). The cell morphology observed by SEM showed the presence of whole cells, with integrated shape and attached to the substrate, similar to the CT. Even at 31.25 µg/mL, the cells

maintained their normal morphology, showing no signs of typical morphology death as observed for cells treated with LB (see Fig. 6).

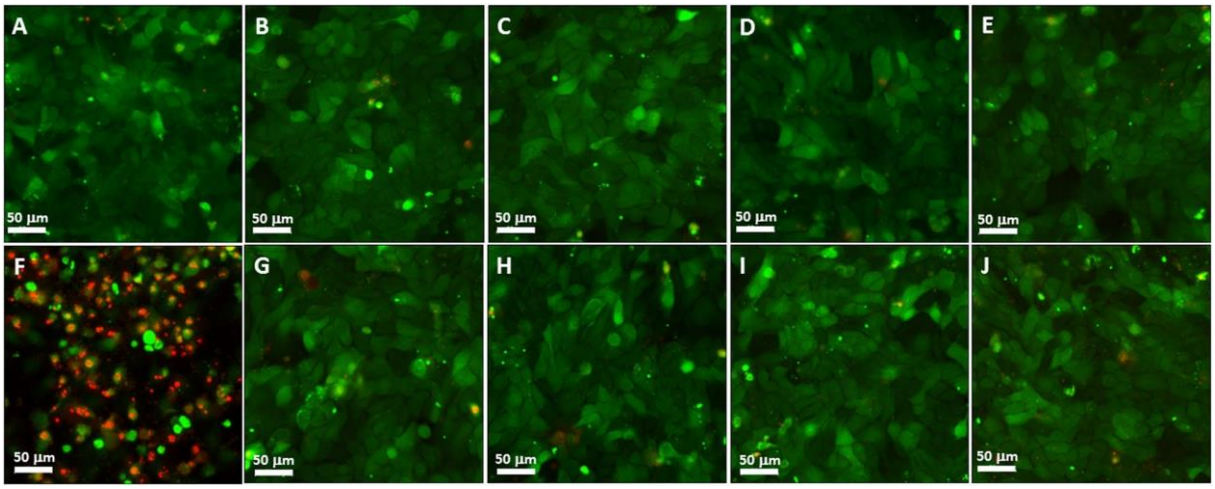

Figure 5. Fluorescence staining of FGH cells after α-Ag_2WO_4 microcrystal incubation. (**A**) Control (without microcrystal); (**B**) 31.25 µg/mL α-Ag_2WO_4:NF; (**C**) 15.62 µg/mL α-Ag_2WO_4:NF; (**D**) 7.81 µg/mL α-Ag_2WO_4:NF; (**E**) 3.90 µg/mL α-Ag_2WO_4:NF; (**F**) Death control (CAM); (**G**) 31.25 µg/mL α-Ag_2WO_4:F; (**H**) 15.62 µg/mL α-Ag_2WO_4:F; (**I**) 7.81 µg/mL α-Ag_2WO_4:F; (**J**) 3.90 µg/mL α-Ag_2WO_4:F.

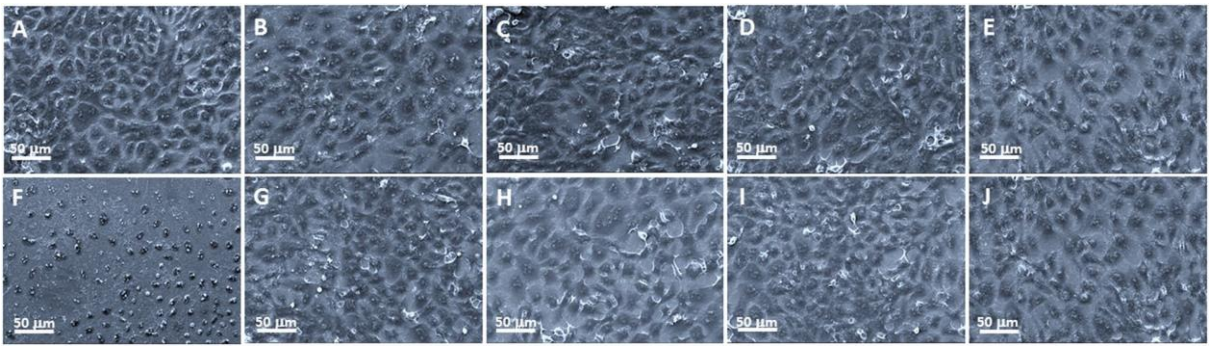

Figure 6. Scanning electron microscopy as a confirmation of biocompatibility α-Ag_2WO_4 effects on FGH cell morphology. (**A**) Control (without microcrystal); (**B**) 31.25 µg/mL α-Ag_2WO_4:NF; (**C**) 15.62 µg/mL α-Ag_2WO_4:NF; (**D**) 7.81 µg/mL α-Ag_2WO_4:NF; (**E**) 3.90 µg/mL α-Ag_2WO_4:NF; (**F**) Death control (LB); (**G**) 31.25 µg/mL α-Ag_2WO_4:F; (**H**) 15.62 µg/mL α-Ag_2WO_4:F; (**I**) 7.81 µg/mL α-Ag_2WO_4:F; (**J**) 3.90 µg/mL α-Ag_2WO_4:F.

In this study, we analyzed the viability of the MB49 and BALB/3T3 cells exposed for 24 h to different samples at concentrations of 1.0 (4.63 µg/mL), 2.5 (11.58 µg/mL), 5.0 (23.16 µg/mL), and 10.0 µmol/mL (46.31 µg/mL). MB49 is an induced bladder carcinoma derived from mouse, and BALB/3T3 is a representative of no tumorigenic cells evaluated by the resazurin assay (Alamar Blue) quantitative fluorimetric assay (Fig. 7). In relation to the major effect of the α-Ag_2WO_4, the BALB/3T3 cell culture presented 95% and 80% cell viability when exposed to concentrations of 4.63 and 11.58 µg/mL, respectively, whereas the MB49 cancer cells presented 50% and 10% of cell viability in comparison to the CT (Fig. 7A). In relation to the other concentration, the loss of viability was intense for both types of cells, mainly at a dose

of 46.31 µg/m. For Ag NPs/α-Ag_2WO_4:E composite, the BALB/3T3 cell culture at 4.63, 11.58, and 23.16 µg/mL concentrations presented viability equivalent to the CT group, whereas the MB49 cell presented a significant reduction in the viability (20%, 80%, and 10%) (Fig. 7B). This increase in cell viability at the intermediate concentration of 11.58 µg/mL shows that this sample has a non-linear behavior against MB49 tumor cell exposure, thus presenting a minimum of inhibition different from the minimum con- centration, obeying a gaussian behavior.

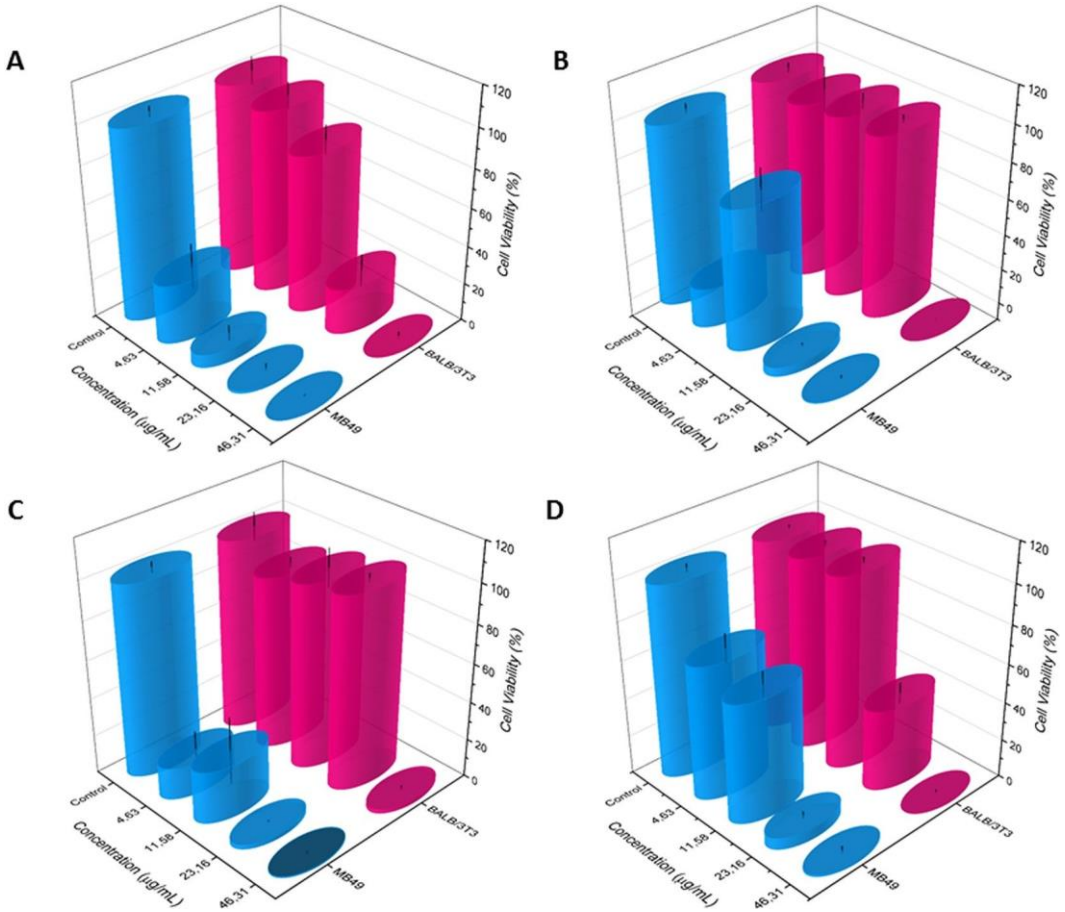

Figure 7. Viability assay of MB49 and BALB/3T3 cells on exposure to samples at concentrations 4.63; 11.58; 23.16; 46.31 µg/ml respectively, for 24 h. (**A**) Ag_2WO_4; (**B**) Ag_2WO_4:E; (**C**) Ag_2WO_4:NF; (**D**) Ag_2WO_4:F.

For Ag NPs/α-Ag_2WO_4:NF composite, the BALB/3T3 cell culture exposed to 4.63, 11.58, and 23.16 µg/mL concentrations of the composite presented viability equivalent to the CT in contrast with the MB49 culture that showed a significant reduction (16%, 32%, and 2%) at the same concentrations (Fig. 7C), with profile of cancer activity very similar with Ag NPs/α-Ag_2WO_4:NF composite (gaussian behavior). For Ag NPs/α-Ag_2WO_4:F composite, the BALB/3T3 cells exposed to 4.63 and 11.58 µg/mL of the sample presented viability greater than 95%, whereas the MB49 cell showed viabilities of 64% and 60%, respectively (Fig. 7D).

Figure 8 illustrates the kinetics of the production of the reactive oxygen species (ROS) in the period of 120 min by MB49 and BALB/3T3 exposed to the different samples at a concentration of 23.16 µg/mL (5 µmol/mL) in comparison with positive (1.0 mM of H_2O_2) and negative control. For the BALB/3T3 cells, the highest ROS pro- duction was reached with the exposure to Ag NPs/α-Ag_2WO_4:F followed by Ag NPs/α-Ag_2WO_4:NF, α-Ag_2WO_4, and Ag NPs/α-Ag_2WO_4:E (Fig. 7A). For the MB49 cell line, in the same way, the highest production of ROS was similar to the obtained with BALB/3T3 cells (α-Ag_2WO_4:F, α-Ag_2WO_4:NF, α-Ag_2WO_4, and α-Ag_2WO_4:E) (Fig. 8B). In comparison with CT, all materials presented a continuously higher production of ROS during the two hours of measurement. The ROS production pattern over time was equivalent for both cell lines (Fig. 8A,B). The level of ROS of the BALB/3T3 cells did not have a linear relationship with the different level of cytotoxicity of the materials (Fig. 7). To the MB49, the toxicity was high, independent of the level of ROS measured.

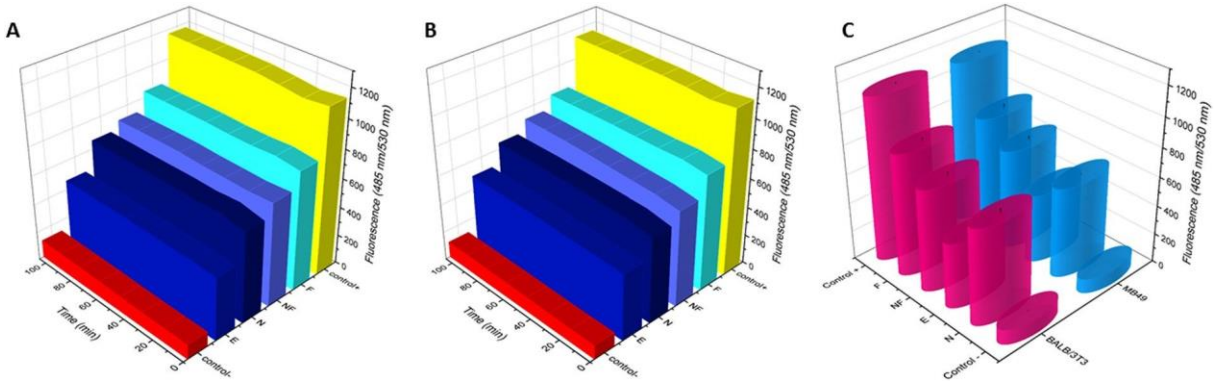

Figure 8. Intracellular detection production of reactive oxygen species (ROS) by BALB/3T3 (**A**) and MB49 (**B**) cells by exposing the samples of Ag_2WO_4:F; Ag_2WO_4:NF; Ag_2WO_4; Ag_2WO_4:E, respectively up to 120 min. Comparison of mean of ROS production by cells exposed to samples (**C**).

By analyzing the specific type of death caused by each sample for both cell lines through the acridine orange (AO) and ethidium bromide (EB) assay, it is possible to observe a difference in resistance of the BALB/3T3 and MB49 lines in relation to the type of sample. The fluorescence images (Fig. 9) show that the BALB/3T3 cell (healthy cell) exposed at a concentration of 23.16 µg/mL of α-Ag_2WO_4, Ag NPs/α-Ag_2WO_4:F, α- Ag NPs/ Ag_2WO_4:NF, or Ag NPs/α-Ag_2WO_4:E maintained its membranes (AO−/EB−). On the contrary, MB49 exposed to α-Ag_2WO_4, Ag NPs/α-Ag_2WO_4:F, and Ag NPs/α-Ag_2WO_4:NF presented signals of apoptosis (Fig. 9G,H: AO+/EB−), late apoptosis (Fig. 9K,L: AO+/EB+) and necrosis (Fig. 9O,P: AO−/EB+), respectively. The cells exposed to Ag NPs/α-Ag_2WO_4:E totally lost the

integrity of the membranes and it was possible to observe only the presence of cellular debris (Fig. 9O,P).

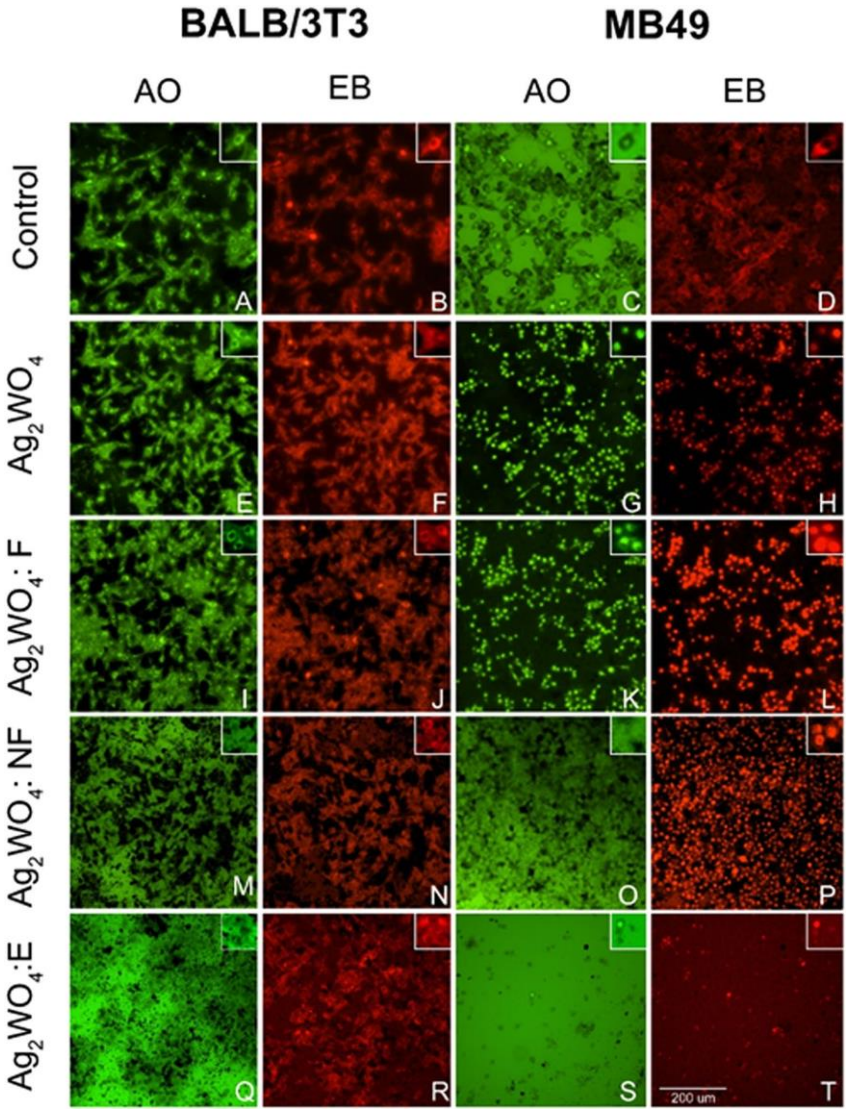

Figure 9. Cell death assay (apoptosis and necrosis). AO/EB: Acridine Orange/Ethidium Bromide. (**A**) control cells BALB/3T3 absent from apoptosis; (**B**) control cells BALB/3T3 absent from necrosis; (**C**) control cells MB49 absent from apoptosis; (**D**) control cells MB49 absent from necrosis; (**E**) Ag_2WO_4 cells BALB/3T3 absence amount of apoptosis death; (**F**) Ag_2WO_4 cells BALB/3T3 absence of necrotic death; (**G**) Ag_2WO_4 cells MB49 large amount of apoptosis death; (**H**) Ag_2WO_4 cells MB49 absence of necrotic death; (**I**) Ag_2WO_4:F cells BALB/3T3 absence amount of apoptosis death; (**J**) Ag_2WO_4:F cells BALB/3T3 absence of necrotic death; (**K**) Ag_2WO_4:F cells MB49 large amount of apoptosis death; (**L**) Ag_2WO_4:F cells MB49 large amount of necrotic death; (**M**)) Ag_2WO_4:NF cells BALB/3T3 absence of apoptosis death; (**N**) Ag_2WO_4:NF cells BALB/3T3 absence of necrotic death; (**O**) Ag_2WO_4:NF cells MB49 absence of apoptosis death; (**P**) Ag_2WO_4:NF cells MB49 large amount of necrotic death; (**Q**) Ag_2WO_4:E cells BALB/3T3 absence of apoptosis death; (**R**) Ag_2WO_4:E cells BALB/3T3 absence of necrotic death; (**S**) Ag_2WO_4:E cell debris (cellular debris) MB49; (**T**) Ag_2WO_4:E cell debris (cellular debris).

In order to evaluate the ROS production of the composites, tests of photocatalytic activity (Fig. 10) were per- formed with the addition of appropriate reactive species scavengers. For these tests, benzoquinone (BQ) was used to capture superoxide radicals (O_2') and tert-butyl alcohol (TBA) was used to capture hydroxyl radicals (*OH**), because these species are directly linked to the oxidative stress of these cells and their subsequent death. α-Ag_2WO_4 presents a low efficiency in the photocatalysis (~48%) and when the TBA is added, this value reduces, indicating an action by the radical *OH** in the oxidative processes. The same was done by adding BQ to Ag NPs/α-Ag_2WO_4 composite, but the photocatalytic activity remained constant, showing that the O_2' moiety is not generated by α-Ag_2WO_4. For Ag NPs/α-Ag_2WO_4:NF and Ag NPs/α-Ag_2WO_4:E composites, an increase in the dye degradation is observed, owing to the structural modifications of both samples. When TBA is added to the process, a reduction of the photocatalytic efficiency occurs, and once the BQ is added, the efficiency becomes constant, that is, the oxidative process occurs through the *OH** radical as well as in the α-Ag_2WO_4. Finally, Ag NPs/α-Ag_2WO_4:F composite was the only that showed a contribution to the radical O_2', apart from the contribution of *OH**, thus causing an increase in its photocatalytic efficiency among all the materials.

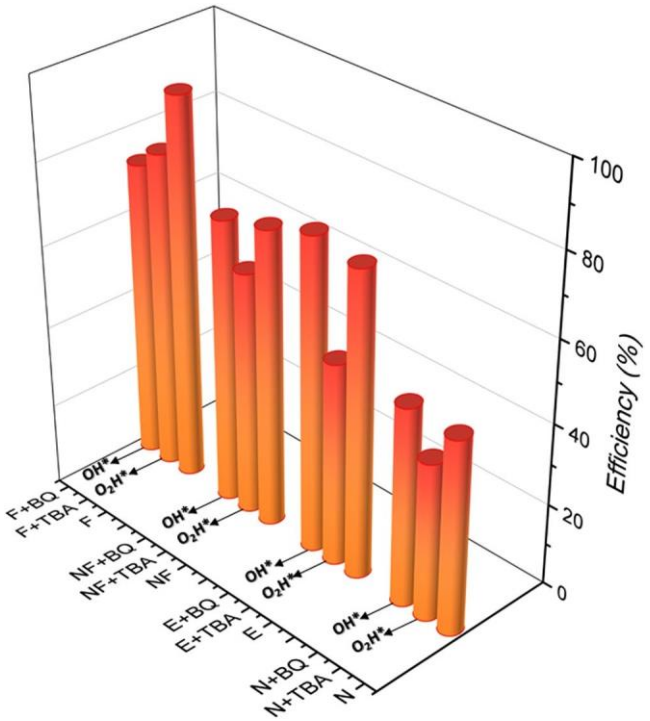

Figure 10. Influence of various scavengers onto the photodegradation of RhB.

Discussion

In the XRD patterns (Fig. 1), we observe a right-shift of some peaks in the composites, including the main peak (231), as well as the suppression of certain diffraction peaks (Fig. 1B,C). This change can be associated with the electron beam irradiation and fs laser irradiation that provokes a decrease in the interplanar distances of this plane with a concomitant small reduction in the volume of the unit cell, indicating that the effect of different irradiations changes certain orientations of the clusters forming the material, increasing the long-range disorder. It is not possible to observe Ag in the XRD spectrum, because the growth phenomena of these Ag NPs are delocalized and superficial in α-Ag_2WO_4.

Another factor related to structural order/disorder effects at long-range can be found by analyzing the full width at half maximum of the most intense peak of the XRD patterns, related to the (231) plane. An increment in the FWHM of this peak in the non-irradiated material with respect to the others is observed as 0.34°, 0.40°, 0.43°, and 0.57° related to α-Ag_2WO_4, α-Ag_2WO_4:E, α-Ag_2WO_4:NF, and α-Ag_2WO_4:F, respectively. These values indicate that when the material is irradiated with the focused fs laser, the structural disorder is much higher than it is for irradiation with the non-focused fs laser and electron beam.

The micro-Raman spectroscopy analysis shows structural disorder associated with the vibrational modes of [WO_6] clusters (Fig. 2). The formation of Ag NPs during the irradiation (fs laser and electron beam) provokes distortions in the [WO_6] clusters. According to Longo *et al.*[34], when the α-Ag_2WO_4 is irradiated with electron beam in a SEM, Ag nanofilaments grow in the surface of the material, thereby forming a Ag NPs/α-Ag_2WO_4 composite (Fig. 3B). This happens because [AgO_2] and [AgO_4] clusters accept the incoming electron density and the reduction of Ag cation occurs with a concomitant Ag formation process. When the material is irradiated with a fs laser, spherical Ag NPs grow on the surface of α-Ag_2WO_4, yielding a Ag NPs/α-Ag_2WO_4 composite (Fig. 3C,D). Fs laser irradiation strips the equilibrium system, causing the segregation of these Ag NPs[36].

As mentioned above, α-Ag_2WO_4 without any irradiation is an n-type semiconductor, it has positive charge holes in its structure, which combined with the effect of the Ag present on the material have a high oxidizing power. Under electron beam irradiation, α-Ag_2WO_4 semiconductor becomes n/p due to the formation of Ag vacancies within the material. On the contrary, when α-Ag_2WO_4 is subject to fs radiation, the structural disorder of the sample is increased because the fs laser beam is concentrated in localized regions of the material's surface, promoting an increment in the segregation process of Ag NPs out of α-Ag_2WO_4 semiconductor; then, a new semiconductor with a larger p character is formed, owing to a higher density of Ag vacancies.

When α-Ag_2WO_4 was irradiated with electron beam and fs laser in non-focused mode, nucleation and formation of Ag NPs was observed, transforming α-Ag_2WO_4 into Ag NPs/α-Ag_2WO_4 composite, acting as a n/p semiconductor type. In the α-Ag_2WO_4: NF sample, not only the plasmonic effect is potentiated but there is selectivity and only the cancer cells are affected under the effects of the new tungsten clusters. This is probably due to the highly unregulated energy rate of tumor cells, since they exhibit aberrant growth rates relative to normal cells, which require high levels of ATP for the production of carbohydrates, proteins, lipids and nucleic acids[58,59]. The antimicrobial activity of α-Ag_2WO_4 composites has been previously described[36,53–55]. Comparing the anti- microbial activity of α-Ag_2WO_4 and α- Ag NPs/Ag_2WO_4:E composite, a fourfold improvement in the activity against Methicillin-Resistant *Staphylococcus aureus* ATCC 33591 (MRSA) bacteria was observed. In previous works[36], the antimicrobial action of the Ag NPs/α-Ag_2WO_4:F composite against the MRSA bacteria exhibited a 32-fold greater efficacy than the non-irradiated material, where the nucleation of metallic Ag NPs can be associated to a surface plasmonic effect, with a subsequent enhancement of their antimicrobial activity. In the present study, Ag NPs/α-Ag_2WO_4:F composite exhibits the best antifungal activity, showing a larger number of defects and metallic Ag NPs on the material surface, which is believed to be the reason for the enhanced surface plasmonic effect leading to a bactericidal improvement (Fig. 4A). The biofilms treated with this sample presented a smaller area of coverage, smaller number of cells, and morphologically altered cells, in comparison with the other biofilms.

The known antimicrobial potential of α-Ag_2WO_4 is a notable feature of this material[54] and its antifungal potential was shown in this work. The development of technologies that provide modifications of different characteristics with respect to their morphological structure as well as highly controlled physicochemical activities and surface area, increases its capacity of application and its therapeutic use[60]. Ag NPs is extremely poisonous against planktonic cells and biofilms of different species, at exceptionally low concentrations, compared to different commercial antimicrobials[61]. Apart from its capacity to participate in oxidative reactions, Ag NPs damages and inhibits Fe–S-containing dehydratases at bactericide concentrations, leading to microbial death[62].

Previously, Ag NPs have been reported to have effective antitumor effects at low concentrations, as they cause irreversible DNA damage[63]. However, their genotoxic and cytotoxic effects provoked some instability in its use. The combination of Ag NPs with other materials, such as tungsten (W) has led to its reduced toxicity according to different studies[54,55]. As eukaryotic and bacterial cells possess distinct transport metalloproteins, some metal com-

pounds discriminate between bacterial targets and eukaryotic cells[64]. In this way, the material is toxic to *Candida albicans* cells, and at the same concentration does not cause damage FGH cells (Figs 4B, 5 and 6).

In this study, the viability and cytotoxicity of MB49 tumor and BALB/3T3 non-tumor cells exposed to the samples irradiated by different energy sources has been analyzed (Fig. 7). Our results show that the samples had effective abilities to cause the death of MB49 relative to normal BALB/3T3 cells, depending on the concentration (Fig. 7). The order of antitumor activity when the cells was exposed to a more effective concentrations (23.16 μg/mL) of the composites is: Ag NPs/α-Ag_2WO_4:NF > Ag NPs/α-Ag_2WO_4:E > Ag NPs/α-Ag_2WO_4:F > α-Ag_2WO_4. This is due to the formation of Ag NPs on the surface of the semiconductor and the generation of internal defects in the material, which cause a threshold between Ag toxicity and its antitumor activity. It was also observed that the material that was better for the antifungal activity, Ag NPs/α-Ag_2WO_4:F composite, showed no selectivity between tumor and non-tumor cells in relation to the others, because the number of Ag NPs on its surface exceeded its toxicity threshold[58].

The samples are considered triggering elements for the cell death pathway. Oxidative stress induced by the samples linked to the intrinsic (mitochondrial effects) or extrinsic apoptotic network (cytoplasmic effect) is currently the most accepted description[65], and many *in vitro* studies have identified a significant increase in ROS as a toxicity factor[66–68], regulating the expression of apoptotic proteins (Figs 8 and 9). The signals that are produced in response to these stimuli increase the permeabilization of the mitochondria, interrupting the synthesis of ATP and releasing the pro-apoptotic molecules, which triggers the production of the protein complex, culminating with the final events of the cell death itself[65,69].

In the case of Ag NPs/α-Ag_2WO_4 composites, the excited electrons from Ag NPs can be transferred to the conduction band (CB) of α-Ag_2WO_4 semiconductor and then further transferred to the noble metal particles owing to the Fermi-level equilibration. Under visible-light irradiation, the processes of the photo-induced charge separation and transfer at the interface of the metal Ag NPs and α-Ag_2WO_4 semiconductor can be divided into the following steps: (i) the visible light is harvested by the metal Ag, and then a hot electron transfer from Ag to α-Ag_2WO_4 takes place; (ii) the local electric field in the Ag NPs/α-Ag_2WO_4 composite can promote electron–hole pair separation under visible-light irradiation. The other Ag particles on the α-Ag_2WO_4 surface act as an efficient photocatalyst and trap the photoexcited electrons that come from the CB of α-Ag_2WO_4. The promotion effects on the separation of the photogenerated electron−hole pairs on α-Ag_2WO_4 by Ag can be achieved. Overall, the synergistic effect,

enhanced visible-light absorption, and efficient electron–hole separation plays an important role in enhancing the activity of Ag NPs/α-Ag_2WO_4 composite.

In the photocatalytic activity of both α -Ag_2WO_4 and Ag/α -Ag_2WO_4, Liu et al. proposed a mechanism involving three steps: (i) Light absorption and photoelectron excitation, i.e., the electrons are excited from the CB to the valence band (VB) and the photogenerated holes appear in the VB. (ii) Formation of the free radical. The photoelectrons at the CB at the surface of the semiconductor would react with the surrounding substances, such as O_2 molecule and generate O_2' radical, which could turn into other ROS including HO^*, or H_2O_2 by successive photochemical processes. On the contrary, the photogenerated holes in the VB can yield OH^* by combining with OH^- (iii) The last step corresponds to radical oxidizing rearrangements involving ROS; it must be pointed out that neither α-Ag_2WO_4 nor Ag/α-Ag_2WO_4 could produce electron spin resonance (ESR) signals without light irradiation. However, after visible-light irradiation, the presence of radical OH* is detected by ESR, where the ESR signals of the Ag/α-Ag_2WO_4 nanocomposites was almost 1.5 bigger than that of α-Ag_2WO_4, exhibiting a better photosensitive ability to produce OH* under visible-light irradiation.

Avalos et al.[70] measured the production of ROS induced by distinct sizes of Ag NPs in HepG2 and HL-60 tumor cells. The results showed that the higher ROS production can be attributed to an increment in the surface area of the NPs. In the work of Hussain et al.[71] it was also demonstrated that for TiO_2 NPs, the ROS modulation was proportional to the reactivity of the small area of the NPs. Depending of the magnitude of ROS production, the samples presented a different level of toxicity.

The Ag NPs/α-Ag_2WO_4:F composite has a major capacity to produce ROS (Fig. 9), which causes this material to have the best antifungal activity, as confirmed by assay (Fig. 4A). However, with respect to the antitumor activity, the high degree of cytotoxicity affects the tumor cell MB49 and non-tumor cell BALB/3T3 in the same way, indistinctly producing cell death at concentration of 23.16 µg/mL. On the contrary, the number of Ag NPs formed on the surface of Ag NPs/α-Ag_2WO_4:NF and Ag NPs/α-Ag_2WO_4:E composites is capable of producing a selective cytotoxic effect on tumor cells. This characteristic is probably related to the resistance to ROS action.

Thus, these electrons and holes ultimately produce ROS. As a function of the aerobic metabolism and oxidation of substrates, normal cells continuously produce ROS and the low level of intracellular ROS generated during the physiological activities acts as a factor in the differentiation, progression, arrest of growth, apoptosis, and immune response. However, when ROS are accumulated in a high quantity, the cells get into an oxidative stress state that induces

a plethora of dysfunctional alterations in macromolecules such as DNA and lipids, among others that can lead to the cellular death. In order to counterbalance the excess of ROS production, the cells possess an efficient system formed by antioxidant enzymes such as superoxide dismutase (SOD), glutathione peroxidase, and catalase that protect the cell from oxidative stress[72].

In the normal process, the redox state may contribute to tumor progression, increasing the expression of genes related to ROS metabolism, such as the enzyme SOD[73,74]. However, with exposure to materials, the induction of genotoxicity through DNA breakdown may occur. In this case, the production of ROS is an important factor. Materials have the potential to lead to cell death by the induction of autophagic dysfunction produced by mechanisms that lead to the overload or inhibition of lysosomal activity, interference of organelles trafficking by the cytoskeleton, and the breakdown of lysosomal stability (oxidative stress, alkalinization, osmotic edema, and membrane rupture). Finally, the materials induce the formation of the protein complex known as inflammassome that mediates the production of the IL-1β pyrogenic mediator, which stimulates the development of acute inflammatory process.

Here, we can assume that non-tumor cells could present some mechanism beyond tumor cells that allow survival when exposed to oxidative stress. This selectivity is associated with the basic mechanism that undergoes interference by the samples with the cells' ability to compensate for the changes caused[75]. This is in contrast to the tumoral cells, in which the ROS act as secondary messengers in intracellular cascades, inducing and maintaining malignant phenotype. The DNA damage, mutations, and altered gene expression are involved in carcinogenesis[76]. A large body of research about the microbial[53,54] and antifungal[55] activity of α-Ag_2WO_4 material has been presented by our research group, and very recently, we demonstrated that when the material is irradiated by pulsed fs laser, its bactericidal properties are enhanced[36]. The present study demonstrates, for first time, the antifungal and antitumor activity of Ag NPs/α-Ag_2WO_4 composite formed by electron beam and fs irradiation. However, it is important to remark that the mode through which these composites exert their biological actions has not as yet been fully elucidated. There is compelling evidence that ROS species are responsible for the antifungal and antitumor effects.

It is important to note that the elucidation of the mechanisms of action as well as the molecular changes caused in the cells is out of the aims of present work. Excellent reports on antifungal and potential tumoricidal NPs, particularly for realistic physiological situations, have been published in the literature. The ongoing works are based on different studies in which the production of ROS is the main mechanism of action of Ag containing materials for the

elimination of neoplastic cells[63,77–84]. Tough, the researchers have widely explored the antibacterial efficacy of Ag NPs but their mode of action is still not clear[85,86]. Possible mechanisms contributing to the biological effects include both the direct damage to cell membranes by Ag NPs and the Ag NPs-mediated generation of ROS. He et al. points out that Ag NPs enhance a powerful oxidant through a reaction with H_2O_2, and the oxidizing species did not include the free OH*. It is well known that free OH* is highly reactive and can damage virtually all types of macromolecules, especially the nucleic acid and lipids. This evidence indicates that the lack of significant generation of OH* but large amount of other ROS species by the laser generated Ag NPs in our experiment suggest that the molecular mechanisms underlying the antifungal and antitumor effect might be dependent on the method used for the NP production and the target microbial species. It would be interesting in a future study to compare the behavior between the specific ROS species induced by electron beam and fs laser irradiation. This would further clarify the specific properties of the generated Ag NPs/α Ag2WO4 composite.

Conclusions

The development and use of hybrid nanomaterials, composed by noble metal nanoparticles–semiconductor composites, are playing increasingly important roles and becoming useful multifunctional materials toward the development of advanced intelligent devices with novel, multiple, and versatile bioactivities.

In the current work, we deployed our investigations in this regard by constructing an interesting composite system formed by Ag NPs and α-Ag_2WO_4 fabricated by electron beam and fs laser irradiation on α-Ag_2WO_4, and its remarkable higher performance in antifungal and antitumor activity were demonstrated.

The synergistic effect of the plasmonic Ag nanoparticles on the α- Ag_2WO_4 semiconductor enhances the anti- fungal and antitumor efficiency. For the antitumor activity, the best results were achieved by the α-Ag_2WO_4:NF and α-Ag_2WO_4:E materials, which showed greater selectivity and efficacy against the action of MB49 tumor cells and greater cell viability of healthy BALB/3T3 cells. In the case of the antifungal activity, the synergism between the bacteriostatic effect of W and the higher oxidizing power of Ag NPs makes the α-Ag_2WO_4:F the best fungicide agent, with a minimum concentration of 3.90 µg/mL.

The irradiation of solids with energetic species, such as electrons or photons, normally gives rise to formation of atomic defects in the target and spoils the material properties. However, in spite of the damage, irradiation may overall have a beneficial effect on the target.

This application motivated further studies of defect production under irradiation, because each implanted atom creates many lattice defects in the sample, imparting to the material new properties to be explored.

Experimental section

Synthesis. The synthesis method, based on the aqueous coprecipitation method, of α-Ag_2WO_4 was previously reported by Longo *et al*.[36].

Electron irradiation. To irradiate the material with electrons to obtain Ag NPs/α-Ag_2WO_4:E composite, the α-Ag_2WO_4 sample was placed in a field emission gun scanning electron microscope (SEM-FEG) using a Supra 35-VP (Carl Zeiss, Germany) with an acceleration voltage of 15 kV for 5 min.

Fs irradiation. α-Ag_2WO_4 pellets were irradiated with a Ti:sapphire laser (Femtopower Compact Pro, Femto Lasers) using 30 fs full width at half maximum (FWHM) pulses at the central wavelength of 800 nm, and a repetition rate of 1 kHz. To get more precise pulse compression at the sample, a programmable acousto-optic filter (DAZZLER, Faslite) was used. A laser beam of 6 mm diameter and mean power of 200 mW was focused onto the surface of a pellet target of α- Ag_2WO_4 with a 75 mm lens. To obtain the Ag NPs/α-Ag_2WO_4:F composite, the α- Ag_2WO_4 pellet was placed at the bottom of a quartz cuvette attached to a two-dimensional motion-controlled stage moving in a raster scanning at a constant speed of 0.45 mm/s in the focus plane perpendicular to the laser beam. At the focal position, the spot size was approximately 21 μm with a fluence of approximately 60 J/cm2. For the Ag NPs/α-Ag_2WO_4:NF composite, the position of the pellet was moved 8 mm closer to the convex lens to obtain a focal spot of approximately 84 μm and a fluence of approximately 3.6 J/cm2. The large difference in the fluence over the two samples is the key parameter for the structural differences between them as, reported in[38].

Characterization. The microcrystalline powders were characterized using XRD with a D/Max-2500PC diffractometer (Rigaku, Japan) involving CuK α radiation (λ = 1.54056 Å) in the 10–70° 2θ range at a scan rate of 0.01° min^{-1}. Micro-Raman spectroscopy was carried out using an iHR550 spectrometer (Horiba Jobin-Yvon, Japan) coupled to a charge-coupled device (CCD) detector and an argon-ion laser (MellesGriot, USA) operating at 633 nm with a maximum power of 200 mW. The spectra were measured in the 50–1000 cm^{-1} range. The SEM images were analyzed using field emission gun scanning electron microscopy (FEG-SEM) on an FEI instrument (Model Inspect F50) operating at 5 kV.

Antifungal study. The culture of *Candida albicans* ATCC 90028 was kept frozen at −80 °C. Before the tests, the cells were thawed and streaked onto Sabouraud dextrose agar supplemented with 0.05 g/L chloramphenicol (SDA, Acumedia Manufacturers Inc., Baltimore, MD, USA). The plate was incubated for 24 h at 37 °C, and then five colonies were transferred to yeast nitrogen base culture medium supplemented with 100 mM glucose (YNB) and incubated for 16 h to prepare the pre-inoculum. Sequentially, the pre-inoculum was diluted 1:10 in fresh YNB and incubated for an additional 8 h until the cells had the mid-log phase of growth. The cells were standardized at a concentration of 10^7 by a spectrophotometer and incubated for 90 min for the initial cell adhesion phase at 37 °C. Then, the non-adhered cells were removed through two washes with phosphate-buffered saline solution (PBS, pH 7.2), and incubated for 24 h with the samples two-fold diluted in YNB for the biofilm formation phase. After the growth of the biofilm in contact with the particles, 10-fold dilutions were prepared of each well and 10 µL aliquots of these were inoculated in duplicate SDA. The plates were incubated for 24 h at 37 °C, the colony forming units per milliliter (CFU/mL) were calculated and $\log_{10}$-transformed.

Biocompatibility of antifungal Ag NPs/Ag_2WO_4:NF and Ag NPs/Ag_2WO_4:F composites. For biocompatibility assays, human gingival fibroblasts (FGH cell line from Rio de Janeiro Cell Bank Code 0089) were used as a model in monolayer cultures. The cells were cultured in Dulbecco's Modified Eagle's Medium Low Glucose (DMEM, Sigma Chemical Co., St. Louis, MO, USA) medium, supplemented with 10% fetal bovine serum (FBS, Gibco, Grand Island, NY, USA), 100 IU/mL penicillin, 100 mg/mL streptomycin (Sigma-Aldrich, St. Louis, MO, USA), and 2 mM L-glutamine (Gibco, Grand Island, NY, USA) in a humidified atmosphere containing 5% CO_2 at 37 °C. After reaching 90% confluence, the cells were washed with PBS, recovered using trypsin, and re suspended in fresh medium prior to further analyses. The assessment of α- Ag NPs/Ag_2WO_4:NF and Ag NPs/α-Ag_2WO_4:F composites on cell viability were evaluated by the resazurin assay (Alamar Blue quantitative fluorimetric assay). FGH cells were seeded at 8 × 103 cells/well directly into the 96-well polystyrene black plate (TPP Tissue Culture Plates, USA) for monolayer cell culture. The cells were incubated at 37 °C under 5% CO_2 for 24 h. Next, the medium was removed and 200 µL of the fresh medium containing the composites was added at 3.90, 7,81, 15.62, and 31.25 µg/mL. In sequence, 10% of resazurin assay-Alamar Blue (Invitrogen, Carlsbad, CA, USA) was added into each well and the fluorescence signals were measured using a Fluoroskan (Fluoroskan Ascent FL; Thermo Scientific; Waltham, MA, USA) at an excitation wavelength at 544 nm and an emission wavelength at 590 nm, after 24-h incubation. The experiment was performed in triplicate and with

three independent biological repetitions. To confirm the impact of the concentrations of the samples on gingival fibroblasts behavior we investigated the proliferation/cell death staining by labeling the cells with CellTracerTMCFSE (Invitrogen, Eugene, OR,USA) and propidium iodide - PI 20 µM (Invitrogen, Eugene, OR,USA) after 24 h of incubation with materials. This assay was performed by CLSM using a Carl Zeiss LSM 800 microscope (Zeiss, Jena, Germany). The green fluorescence of CFSE and the red one of PI were employed by laser excitation at 488 nm and 561 nm, respectively. Images were acquired through 20X dry (Plan NeoFluar NA). Finally, the cell morphology was investigated by SEM using a JEOL JSM-6610LV microscope (Ref JEOL). First, 5 × 104 cells were plated on sterile cover glass discs on a 24-well plate (TPP Tissue Culture, Switzerland) and maintained at 37 °C under 5% CO_2 conditions. After 24 h the medium was removed and materials were added at concentrations 3.90, 7,81, 15.62, and 31.25 µg/mL for 24 h. After this period, the samples were prepared for SEM analyses. A fixation step was performed by sample incubation in a solution of 2.5% glutaraldehyde (pH 7.4) at room temperature for 1 h. The PBS-washed discs were then subjected to a standard procedure for dehydrating of specimens: 70% and 90% ethanol for 1 h per step, ending with five changes within 30 minutes of 100% ethanol. Prior to visualization, the discs were placed under *vacuum* to protect the dry samples from moisture, and after storage for seven days, the discs were sputter-coated with gold. The experiment was performed in duplicate for each experimental and control group, which were: CT: cells in standard culture conditions, cell death controls for Alamar Blue and SEM: Triton-X 100 0.9% buffer (LB) or 10 µM of Camptothecin for 8 h (CAM) for CLSM.

Cell viability MB49 and BALB/3T3 on α-Ag_2WO_4 samples exposure. To investigate the *in vitro* toxicity of the samples, the test was carried out with the cell lines MB49 (tumor cell) and BALB/3T3 (non-tumor cell). Both cell lines were plated on 2 96-well culture plates (Corning Incorporated, NY, USA) to a concentration of 1.105 cell/well in DMEM medium (SIGMA-ALDRICH, USA) in the presence of L-glutamine (2 mmol L−1) and penicillin/streptomycin (100 U mL−1) with the addition of fetal bovine serum (10% SFB) and kept overnight. The cells were exposed to α-Ag_2WO_4 samples irradiated by different sources at the following concentrations: 4.63, 11.58, 23.16 and 46.31 µM and a negative control. After the 24 h exposure, the supernatant containing the nanomaterials was collected and the resulting cells were washed with PBS (1X) buffer and the cell viability test was performed by the resazurin assay-Alamar Blue (SIGMA-ALDRICH, USA), was added into each well and the fluorescence signals were measured using a Fluoroskan (Fluoroskan Ascent FL; Thermo Scientific; Waltham, MA, USA), according to the instructions provided by the supplier. The

readings were taken using a spectrophotometer with absorbance in the range 570–600 nm. The experiment was performed in triplicate.

Reactive oxygen species generation assay. The MB49 and BALB/3T3 cells were plated under the same conditions described in item 1, and exposed to the materials at the concentration that presented the best results in the cell viability assay. For the measurement of the production of ROS, kinetics (ROS production/ time) were performed for 105 min (every 15 min) using 100 μm 2′,7′-dichlorofluorescein diacetate (DCF-DA, SIGMA-ALDRICH, USA). The measurement of the ROS production was performed using a Spectra Max i3 (Molecular Devices) with 485–530 nm excitation.

Cytotoxicity assay: apoptosis and necrosis. The MB49 and BALB/3T3 cells were plated in black plate 96-well (Corning Incorporated, NY, USA) under the same conditions described above, and exposed to the mate- rials at the concentration that showed the best results in the previous assay. After the 24 h exposure, the cells were washed with PBS buffer (1X) and subjected to the apoptosis and necrosis assay using acridine orange/ethidium bromide (AO/EB), according to the instructions provided by the supplier. The total count of apoptotic and necrotic cells, as well as the analysis of cellular morphology, was performed on the ImageXpress Micro (Molecular Device) with 515–560 nm excitation filter and 590 nm barrier filter.

Scavengers tests. The scavengers test was performed from the degradation of rhodamine B (RhB) (Aldrich 95%) under ultraviolet light. We dispersed the samples (50 mg) in a RhB solution (50 mL $1 \times 10{-}5$ mol L^{-1}) in a beaker placed in an ultrasonic bath (Branson, model 1510; frequency 42 kHz) for 10 min. This solution was maintained in the dark, under stirring for 30 min to allow the adsorption–desorption process. After this process, the initial aliquot was withdrawn. Next, these solutions were illuminated by four visible lamps (Philips TL-D, 15 W) in a photocatalytic system maintained at 20 °C in a thermostatic bath under stirring. The final aliquot was with- drawn after 60 min. This process was repeated for all the samples. The aliquots were centrifuged to obtain the liquid phase alone. Variations in the absorption band maximum at $\lambda = 553$ nm (RhB) were measured by performing UV-Vis absorption spectroscopy measurements of the solution on a V-660 spectrophotometer (JASCO). To analyze the action of the radicals OH^* and O_2', we performed tests by adding appropriate reactive species scavengers such as 0.067 g of BQ (Alfa Aesar) and 0.0589 mL tert-butyl alcohol (TBA), respectively.

Data presentation and statistical analyses. Data were represented by the mean and standard error of the mean. The data followed the normal distribution; according to the Shapiro-Wilk test, differences between groups were determined using the ANOVA and Newman–Keuls

tests for multiple comparisons. The nominal variables were analyzed by Fisher's exact test. The software used for analyses was GraphPad Prism version 5.00 for Windows (GraphPad Software, San Diego, CA, USA). The tests were considered statistically significant when the p-value was less than 0.05.

References

1. Dong, Z. *et al*. Silver nanoparticles immobilized on fibrous nano-silica as highly efficient and recyclable heterogeneous catalyst for reduction of 4-nitrophenol and 2-nitroaniline. *Applied Catalysis B: Environmental* **158**, 129–135 (2014).
2. Yang, G.-W., Gao, G.-Y., Wang, C., Xu, C.-L. & Li, H.-L. Controllable deposition of Ag nanoparticles on carbon nanotubes as a catalyst for hydrazine oxidation. *Carbon* **46**, 747–752 (2008).
3. Xia, Y., Xiong, Y., Lim, B. & Skrabalak, S. E. Shape-controlled synthesis of metal nanocrystals: Simple chemistry meets complex physics? *Angewandte Chemie International Edition* **48**, 60–103 (2009).
4. Pradhan, N., Pal, A. & Pal, T. Catalytic reduction of aromatic nitro compounds by coinage metal nanoparticles. *Langmuir* **17**, 1800–1802 (2001).
5. Saha, S., Pal, A., Kundu, S., Basu, S. & Pal, T. Photochemical green synthesis of calcium-alginate-stabilized Ag and Au nanoparticles and their catalytic application to 4-nitrophenol reduction. *Langmuir* **26**, 2885–2893 (2009).
6. Signori, A. M. *et al*. Formation of catalytic silver nanoparticles supported on branched polyethyleneimine derivatives. *Langmuir* **26**, 17772–17779 (2010).
7. Li, Q. *et al*. Antimicrobial nanomaterials for water disinfection and microbial control: potential applications and implications. *Water research* **42**, 4591–4602 (2008).
8. Tolaymat, T. M. *et al*. An evidence-based environmental perspective of manufactured silver nanoparticle in syntheses and applications: a systematic review and critical appraisal of peer-reviewed scientific papers. *Science of the Total Environment* **408**, 999–1006 (2010).
9. Mitrano, D. M. *et al*. Presence of nanoparticles in wash water from conventional silver and nano-silver textiles. *ACS Nano* **8**, 7208–7219 (2014).
10. Varner, K., El-Badawy, A., Feldhake, D. & Venkatapathy, R. State-of-the-science review: everything nanosilver and more. US Environmental Protection Agency, Washington, DC. (EPA/600/R-10/084, 2010).
11. Rai, M., Yadav, A. & Gade, A. Silver nanoparticles as a new generation of antimicrobials. *Biotechnology Advances* **27**, 76–83 (2009).
12. Nowack, B., Krug, H. F. & Height, M. 120 years of nanosilver history: implications for policy makers. *Environmental Science & Technology* **45**, 1177–1183 (2011).
13. Seil, J. T. & Webster, T. J. Antimicrobial applications of nanotechnology: methods and literature. *International Journal of Nanomedicine* **7**, 2767 (2012).
14. Xiang, D. *et al*. Inhibition of A/Human/Hubei/3/2005 (H3N2) influenza virus infection by silver nanoparticles *in vitro* and *in vivo*. *International Journal of Nanomedicine* **8**, 4103 (2013).
15. Maillard, J.-Y. & Hartemann, P. Silver as an antimicrobial: facts and gaps in knowledge. *Critical Reviews in Microbiology* **39**, 373–383 (2013).
16. Morones, J. R. *et al*. The bactericidal effect of silver nanoparticles. *Nanotechnology* **16**, 2346 (2005).
17. Chernousova, S. & Epple, M. Silver as antibacterial agent: ion, nanoparticle, and metal. *Angewandte Chemie* **52**, 1636–1653 (2013).

18. Kvitek, L. *et al*. Initial study on the toxicity of silver nanoparticles (NPs) against Paramecium caudatum. *The Journal of Physical Chemistry C* **113**, 4296–4300 (2009).
19. Kim, J. S. *et al*. Antimicrobial effects of silver nanoparticles. *Nanomedicine: Nanotechnology, Biology and Medicine* **3**, 95–101 (2007).
20. Wodka, D. *et al*. Photocatalytic activity of titanium dioxide modified by silver nanoparticles. *ACS Applied Materials & Interfaces* **2**, 1945–1953 (2010).
21. Panáček, A. *et al*. Antifungal activity of silver nanoparticles against Candida spp. *Biomaterials* **30**, 6333–6340 (2009).
22. Xiu, Z.-M., Zhang, Q.-B., Puppala, H. L., Colvin, V. L. & Alvarez, P. J. Negligible particle-specific antibacterial activity of silver nanoparticles. *Nano Letters* **12**, 4271–4275 (2012).
23. Martinez-Gutierrez, F. *et al*. Synthesis, characterization, and evaluation of antimicrobial and cytotoxic effect of silver and titanium nanoparticles. *Nanomedicine: Nanotechnology, Biology and Medicine* **6**, 681–688 (2010).
24. Bhat, R. *et al*. Photo-bio-synthesis of irregular shaped functionalized gold nanoparticles using edible mushroom Pleurotus florida and its anticancer evaluation. *Journal of Photochemistry and Photobiology B: Biology* **125**, 63–69 (2013).
25. Dipankar, C. & Murugan, S. The green synthesis, characterization and evaluation of the biological activities of silver nanoparticles synthesized from Iresine herbstii leaf aqueous extracts. *Colloids and Surfaces B: Biointerfaces* **98**, 112–119 (2012).
26. Jeyaraj, M. *et al*. Biogenic silver nanoparticles for cancer treatment: an experimental report. *Colloids and Surfaces B: Biointerfaces* **106**, 86–92 (2013).
27. Pugazhendhi, S., Kirubha, E., Palanisamy, P. & Gopalakrishnan, R. Synthesis and characterization of silver nanoparticles from Alpinia calcarata by Green approach and its applications in bactericidal and nonlinear optics. *Applied Surface Science* **357**, 1801–1808 (2015).
28. Wang, H. *et al*. Semiconductor heterojunction photocatalysts: design, construction, and photocatalytic performances. *Chemical Society Reviews* **43**, 5234–5244 (2014).
29. Mehdi, A., Reye, C. & Corriu, R. From molecular chemistry to hybrid nanomaterials. Design and functionalization. *Chemical Society Reviews* **40**, 563–574 (2011).
30. Emeline, A., Kuznetsov, V., Ryabchuk, V. & Serpone, N. On the way to the creation of next generation photoactive materials. *Environmental Science and Pollution Research* **19**, 3666–3675 (2012).
31. Zhang, Y. *et al*. Surface-plasmon-driven hot electron photochemistry. *Chemical Reviews* **118**, 2927–2954 (2017).
32. Knight, M. W., Sobhani, H., Nordlander, P. & Halas, N. J. Photodetection with active optical antennas. *Science* **332**, 702–704 (2011).
33. Clavero, C. Plasmon-induced hot-electron generation at nanoparticle/metal-oxide interfaces for photovoltaic and photocatalytic devices. *Nature Photonics* **8**, 95 (2014).
34. Andrés, J. *et al*. Structural and electronic analysis of the atomic scale nucleation of Ag on α-Ag_2WO_4 induced by electron irradiation. *Scientific Reports* **4**, srep05391 (2014).
35. Cavalcante, L. *et al*. Cluster coordination and photoluminescence properties of α-Ag_2WO_4 microcrystals. *Inorganic Chemistry* **51**, 10675–10687 (2012).
36. Assis, M. *et al*. Towards the scale-up of the formation of nanoparticles on α-Ag_2WO_4 with bactericidal properties by femtosecond laser irradiation. *Scientific Reports* **8**, 1884 (2018).
37. Zhang, X.-Y., Wang, J.-D., Liu, J.-K., Yang, X.-H. & Lu, Y. Construction of silver tungstate multilevel sphere clusters by controlling the energy distribution on the crystal surface. *CrystEngComm* **17**, 1129–1138 (2015).

38. Chen, H. & Xu, Y. Photoactivity and stability of Ag_2WO_4 for organic degradation in aqueous suspensions. *Applied Surface Science* **319**, 319–323 (2014).
39. Lin, Z. *et al*. Electronic reconstruction of α-Ag_2WO_4 nanorods for visible-light photocatalysis. *ACS Nano* **9**, 7256–7265 (2015).
40. Zhang, R. et al. Facile hydrothermal synthesis and photocatalytic activity of rod-like nanosized silver tungstate. *Micro & Nano Letters* **7**, 1285–1288 (2012).
41. Da Silva, L. F. et al. A novel ozone gas sensor based on one-dimensional (1D) α-Ag_2WO_4 nanostructures. *Nanoscale* **6**, 4058–4062 (2014).
42. Da Silva, L. F. et al. Acetone gas sensor based on α-Ag_2WO_4 nanorods obtained via a microwave-assisted hydrothermal route. *Journal of Alloys and Compounds* **683**, 186–190 (2016).
43. Linic, S., Christopher, P. & Ingram, D. B. Plasmonic-metal nanostructures for efficient conversion of solar to chemical energy. *Nature Materials* **10**, 911 (2011).
44. Shi, G. et al. Electron beam induced growth of silver nanoparticles. *Scanning* **35**, 69–74 (2013).
45. Mansourian, A., Paknejad, S. A., Zayats, A. V. & Mannan, S. H. Stereoscopic Nanoscale-Precision Growth of Free-Standing Silver Nanorods by Electron Beam Irradiation. *The Journal of Physical Chemistry C* **120**, 20310–20314 (2016).
46. Li, K. & Zhang, F.-S. A novel approach for preparing silver nanoparticles under electron beam irradiation. *Journal of Nanoparticle Research* **12**, 1423–1428 (2010).
47. Longo, E. et al. Direct in situ observation of the electron-driven synthesis of Ag filaments on α-Ag_2WO_4 crystals. *Scientific Reports* **3**, 1676 (2013).
48. da Silva Pereira, W. et al. Elucidating the real-time Ag nanoparticle growth on α-Ag_2WO_4 during electron beam irradiation: experimental evidence and theoretical insights. *Physical Chemistry Chemical Physics* **17**, 5352–5359 (2015).
49. San-Miguel, M. A. et al. In situ growth of Ag nanoparticles on α-Ag_2WO_4 under electron irradiation: probing the physical principles. *Nanotechnology* **27**, 225703 (2016).
50. Longo, E., Avansi, W. Jr., Bettini, J., Andrés, J. & Gracia, L. In situ Transmission Electron Microscopy observation of Ag nanocrystal evolution by surfactant free electron-driven synthesis. *Scientific Reports* **6**, 21498 (2016).
51. Faccin, G. M., San-Miguel, M. A., Andrés, J., Longo, E. & da Silva, E. Z. Computational Modeling for the Ag Nanoparticle Coalescence Process: A Case of Surface Plasmon Resonance. *The Journal of Physical Chemistry C* **121**, 7030–7036 (2017).
52. Andrés, J. et al. Formation of Ag nanoparticles under electron beam irradiation: Atomistic origins from first-principles calculations. *International Journal of Quantum Chemistry* (2017).
53. Longo, V. M. et al. Potentiated electron transference in α-Ag_2WO_4 microcrystals with Ag nanofilaments as microbial agent. *The Journal of Physical Chemistry A* **118**, 5769–5778 (2014).
54. Foggi, C. C. et al. Tuning the morphology, optical and antimicrobial properties of α-Ag_2WO_4 microcrystals by using different solvents. *Crystal Growth & Design* **17**, 6239-6246 (2017).
55. Foggi, C. C. et al. Synthesis and evaluation of α-Ag2WO_4 as novel antifungal agent. *Chemical Physics Letters* **674**, 125–129 (2017).
56. Turkovič, A., Fox, D. L., Scott, J. F., Geller, S. & Ruse, G. F. High temperature Raman spectroscopy of silver tetratungstate, $Ag_8W_4O_{16}$. *Materials Research Bulletin* **12**, 189–195 (1977).
57. Pereira, P. et al. $ZnWO_4$ nanocrystals: synthesis, morphology, photoluminescence and photocatalytic properties. *Physical Chemistry Chemical Physics* **20**, 1923-1937 (2018).

58. Johnston, H. J. et al. A review of the in vivo and in vitro toxicity of silver and gold particulates: particle attributes and biological mechanisms responsible for the observed toxicity. *Critical Reviews in Toxicology* **40**, 328–346 (2010).
59. Tung, J. C. et al. Tumor mechanics and metabolic dysfunction. *Free Radical Biology and Medicine* **79**, 269–280 (2015).
60. De Stefano, D., Carnuccio, R. & Maiuri, M. C. Nanomaterials toxicity and cell death modalities. *Journal of Drug Delivery* **2012**, 167896 (2012).
61. Harrison, J. J., Ceri, H., Stremick, C. A. & Turner, R. J. Biofilm susceptibility to metal toxicity. *Environmental Microbiology* **6**, 1220–1227 (2004).
62. Xu, F. F. & Imlay, J. A. Silver (I), mercury (II), cadmium (II), and zinc (II) target exposed enzymic iron-sulfur clusters when they toxify *Escherichia coli*. *Applied and Environmental Microbiology* **78**, 3614–3621 (2012).
63. Wei, L. et al. Silver nanoparticles: synthesis, properties, and therapeutic applications. *Drug Discovery Today* **20**, 595–601 (2015).
64. Lemire, J. A., Harrison, J. J. & Turner, R. J. Antimicrobial activity of metals: mechanisms, molecular targets and applications. *Nature Reviews Microbiology* **11**, 371 (2013).
65. Sarkar, A., Das, J., Manna, P. & Sil, P. C. Nano-copper induces oxidative stress and apoptosis in kidney via both extrinsic and intrinsic pathways. *Toxicology* **290**, 208–217 (2011).
66. Nel, A., Xia, T., Mädler, L. & Li, N. Toxic potential of materials at the nanolevel. *Science* **311**, 622–627 (2006).
67. Shvedova, A. A., Kagan, V. E. & Fadeel, B. Close encounters of the small kind: adverse effects of man-made materials interfacing with the nano-cosmos of biological systems. *Annual Review of Pharmacology and Toxicology* **50**, 63–88 (2010).
68. Orrenius, S., Nicotera, P. & Zhivotovsky, B. Cell death mechanisms and their implications in toxicology. *Toxicological Sciences* **119**, 3–19 (2010).
69. Manna, P., Ghosh, M., Ghosh, J., Das, J. & Sil, P. C. Contribution of nano-copper particles to in vivo liver dysfunction and cellular damage: Role of IκBα/NF-κB, MAPKs and mitochondrial signal. *Nanotoxicology* **6**, 1–21 (2012).
70. Avalos, A., Haza, A. I., Mateo, D. & Morales, P. Cytotoxicity and ROS production of manufactured silver nanoparticles of different sizes in hepatoma and leukemia cells. *Journal of Applied Toxicology* **34**, 413–423 (2014).
71. Hussain, S. et al. Oxidative stress and proinflammatory effects of carbon black and titanium dioxide nanoparticles: role of particle surface area and internalized amount. *Toxicology* **260**, 142–149 (2009).
72. Matés, J. M., Pérez-Gómez, C. & De Castro, I. N. Antioxidant enzymes and human diseases. *Clinical Biochemistry* **32**, 595–603 (1999).
73. Hempel, N., Ye, H., Abessi, B., Mian, B. & Melendez, J. A. Altered redox status accompanies progression to metastatic human bladder cancer. *Free Radical Biology and Medicine* **46**, 42–50 (2009).
74. Kim, Y. S., Gupta Vallur, P., Phaëton, R., Mythreye, K. & Hempel, N. Insights into the Dichotomous Regulation of SOD2 in Cancer. *Antioxidants* **6**, 86 (2017).
75. Bendale, Y., Bendale, V. & Paul, S. Evaluation of cytotoxic activity of platinum nanoparticles against normal and cancer cells and its anticancer potential through induction of apoptosis. *Integrative Medicine Research* **6**, 141–148 (2017).
76. Valko, M., Rhodes, C., Moncol, J., Izakovic, M. & Mazur, M. Free radicals, metals and antioxidants in oxidative stress-induced cancer. *Chemico-Biological Interactions* **160**, 1–40 (2006).

77. Arora, S., Jain, J., Rajwade, J. & Paknikar, K. Cellular responses induced by silver nanoparticles: in vitro studies. *Toxicology Letters* **179**, 93–100 (2008).
78. Gaillet, S. & Rouanet, J.-M. Silver nanoparticles: their potential toxic effects after oral exposure and underlying mechanisms–a review. *Food and Chemical Toxicology* **77**, 58–63 (2015).
79. Dai, X. et al. Functional silver nanoparticle as a benign antimicrobial agent that eradicates antibiotic-resistant bacteria and promotes wound healing. *ACS Applied Materials & Interfaces* **8**, 25798–25807 (2016).
80. Huma, Z.-e et al. Cationic Silver Nanoclusters as Potent Antimicrobials against Multidrug-Resistant Bacteria. *ACS Omega* **3**, 16721–16727 (2018).
81. Rizzello, L. & Pompa, P. P. Nanosilver-based antibacterial drugs and devices: mechanisms, methodological drawbacks, and guidelines. *Chemical Society Reviews* **43**, 1501–1518 (2014).
82. Le Ouay, B. & Stellacci, F. Antibacterial activity of silver nanoparticles: a surface science insight. *Nano today* **10**, 339–354 (2015).
83. Wang, L.-S., Gupta, A. & Rotello, V. M. Nanomaterials for the treatment of bacterial biofilms. *ACS Infectious Diseases* **2**, 3–4 (2015).
84. Huh, A. J. & Kwon, Y. J. "Nanoantibiotics": a new paradigm for treating infectious diseases using nanomaterials in the antibiotics resistant era. *Journal of Controlled Release* **156**, 128–145 (2011).
85. Jeeva, K., Thiyagarajan, M., Elangovan, V., Geetha, N. & Venkatachalam, P. Caesalpinia coriaria leaf extracts mediated biosynthesis of metallic silver nanoparticles and their antibacterial activity against clinically isolated pathogens. *Industrial Crops and Products* **52**, 714–720 (2014).
86. Khatoon, N., Ahmad, R. & Sardar, M. Robust and fluorescent silver nanoparticles using Artemisia annua: biosynthesis, characterization and antibacterial activity. *Biochemical Engineering Journal* **102**, 91–97 (2015).

2.3 – SiO_2-Ag composite as a highly virucide material: a roadmap that rapidly eliminates SARS-CoV-2

nanomaterials MDPI

Article

SiO_2-Ag Composite as a Highly Virucidal Material: A Roadmap that Rapidly Eliminates SARS-CoV-2

Marcelo Assis [1,2], Luiz Gustavo P. Simoes [3], Guilherme C. Tremiliosi [3], Dyovani Coelho [1], Daniel T. Minozzi [3], Renato I. Santos [3], Daiane C. B. Vilela [3], Jeziel Rodrigues do Santos [1], Lara Kelly Ribeiro [1], Ieda Lucia Viana Rosa [1], Lucia Helena Mascaro [1], Juan Andrés [2,*] and Elson Longo [1]

[1] CDMF, LIEC, Federal University of São Carlos—(UFSCar), 13565-905 São Carlos, SP, Brazil; marcelostassis@gmail.com (M.A.); dyovani@gmail.com (D.C.); prof.jeziel@gmail.com (J.R.d.S.); larakribeiro@gmail.com (L.K.R.); ilvrosa@ufscar.br (I.L.V.R.); lmascaro@ufscar.br (L.H.M.); elson.liec@gmail.com (E.L.)
[2] Department of Physical and Analytical Chemistry, University Jaume I (UJI), 12071 Castellon, Spain
[3] Nanox Tecnologia S/A, 13562-400 São Carlos, SP, Brazil; gustavo@nanox.com.br (L.G.P.S.); guilherme@nanox.com.br (G.C.T.); daniel@nanox.com.br (D.T.M.); renato.santos@nanox.com.br (R.I.S.); microbiologia@nanox.com.br (D.C.B.V.)
* Correspondence: andres@qfa.uji.es

Abstract: COVID-19, as the cause of a global pandemic, has resulted in lockdowns all over the world since early 2020. Both theoretical and experimental efforts are being made to find an effective treatment to suppress the virus, constituting the forefront of current global safety concerns and a significant burden on global economies. The development of innovative materials able to prevent the transmission, spread, and entry of COVID-19 pathogens into the human body is currently in the spotlight. The synthesis of these materials is, therefore, gaining momentum, as methods providing nontoxic and environmentally friendly procedures are in high demand. Here, a highly virucidal material constructed from SiO_2-Ag composite immobilized in a polymeric matrix (ethyl vinyl acetate) is presented. The experimental results indicated that the as-fabricated samples exhibited high antibacterial activity towards *Escherichia coli* (*E. coli*) and *Staphylococcus aureus* (*S. aureus*) as well as towards SARS-CoV-2. Based on the present results and radical scavenger experiments, we propose a possible mechanism to explain the enhancement of the biocidal activity. In the presence of O_2 and H_2O, the plasmon-assisted surface mechanism is the major reaction channel generating reactive oxygen species (ROS). We believe that the present strategy based on the plasmonic effect would be a significant contribution to the design and preparation of efficient biocidal materials. This fundamental research is a precedent for the design and application of adequate technology to the next-generation of antiviral surfaces to combat SARS-CoV-2.

Keywords: COVID-19; virus elimination; antiviral surfaces; SiO_2-Ag composite; ethyl vinyl acetate; surface plasmon resonance effect

check for updates

Citation: Assis, M.; Simoes, L.G.P.; Tremiliosi, G.C.; Coelho, D.; Minozzi, D.T.; Santos, R.I.; Vilela, D.C.B.; Santos, J.R.d.; Ribeiro, L.K.; Rosa, I.L.V.; et al. SiO_2-Ag Composite as a Highly Virucidal Material: A Roadmap that Rapidly Eliminates SARS-CoV-2. *Nanomaterials* **2021**, *11*, 638. https://doi.org/10.3390/nano11030638

Academic Editors: Miguel Gama and Francesco Paolo La Mantia

Received: 7 February 2021
Accepted: 26 February 2021
Published: 4 March 2021

Publisher's Note: MDPI stays neutral

SiO_2-Ag Composite as a Highly Virucidal Material: A Roadmap that Rapidly Eliminates SARS-CoV-2

Marcelo Assis[1,2], Luiz Gustavo P. Simoes[3], Guilherme C. Tremiliosi [3], Dyovani Coelho[1], Daniel T. Minozzi[3], Renato I. Santos[3], Daiane C. B. Vilela[3], Jeziel Rodrigues do Santos[1], Lara Kelly Ribeiro[1], Ieda Lucia Viana Rosa[1], Lucia Helena Mascaro[1], Juan Andrés[2] & Elson Longo[1]

[1]CDMF, LIEC, Federal University of São Carlos (UFSCar), 13565-905 São Carlos, SP, Brazil.
[2]Department of Physical and Analytical Chemistry, University Jaume I (UJI), 12071 Castellon, Spain.
[3]Nanox Tecnologia S/A, 13562-400 São Carlos, SP, Brazil.

COVID-19, as the cause of a global pandemic, has resulted in lockdowns all over the world since early 2020. Both theoretical and experimental efforts are being made to find an effective treatment to suppress the virus, constituting the forefront of current global safety concerns and a significant burden on global economies. The development of innovative materials able to prevent the transmission, spread, and entry of COVID-19 pathogens into the human body is currently in the spotlight. The synthesis of these materials is, therefore, gaining momentum, as methods providing nontoxic and environmentally friendly procedures are in high demand. Here, a highly virucidal material constructed from SiO_2-Ag composite immobilized in a polymeric matrix (ethyl vinyl acetate) is presented. The experimental results indicated that the as-fabricated samples exhibited high antibacterial activity towards *Escherichia coli* (*E. coli*) and *Staphylococcus aureus* (*S. aureus*) as well as towards SARS-CoV-2. Based on the present results and radical scavenger experiments, we propose a possible mechanism to explain the enhancement of the biocidal activity. In the presence of O_2 and H_2O, the plasmon-assisted surface mechanism is the major reaction channel generating reactive oxygen species (ROS). We believe that the present strategy based on the plasmonic effect would be a significant contribution to the design and preparation of efficient biocidal materials. This fundamental research is a precedent for the design and application of adequate technology to the next-generation of antiviral surfaces to combat SARS-CoV-2.

Introduction

The current worldwide public health and economic crisis resulting from COVID-19 has become a critical problem.[1] At present, there are no vaccines or antiviral drugs available for the

prevention or treatment of COVID-19 infections. Currently, many different antiviral agents, including repurposed drugs, are under testing in clinical trials to assess their efficacy, but the quest for an effective treatment against COVID-19 is still ongoing;[2-5] therefore, it is essential to explore any other effective intervention strategies that may reduce the mortality and morbidity rates of the disease. Some excellent reviews of therapeutics and tools that inactivate SARS-CoV-2 have been published.[6-8]

SARS-CoV-2 spreads mainly via human fluids, and individuals may acquire the virus after touching different contaminated surfaces.[9] It is known that SARS-CoV-2 remains viable on solids for extended periods (for up to 1 week on hard surfaces such as glass and stainless steel.[10,11] In response, not only materials capable of killing viruses by contact and having low cytotoxicity is clearly a high priority for all scientists around the world, but also finding new and effective materials to decontaminate surfaces is of great concern.[12–14] Given the significance of the surface and air contamination in the spread of the virus, attention should also be paid to the development of biocide (virus, bacteria, fungus) materials against the spread of contamination facilitated by high touch surfaces, such as protecting hospital environments and the surfaces of biomedical de-vices, along with decontamination equipment and technologies.[6,15–18]

In this scenario, metals, semiconductors, and inorganic materials are gaining in-creased attention as broad-spectrum antivirus agents to protect surfaces and packaging, thus preventing new infections in humans.[19] Very recently, Ghaffari et al.[20] discuss efforts to deploy nanotechnology, biomaterials, and stem cells in each step of the fight against SARS-CoV-2; while Basak and Packirisamy[21] have discussed sever-al nanotechnological strategies that can be used as an antiviral coating to inhibit viral transmission by preventing viral entry into the host cells. In this context, metal oxide nanoparticles and their composites were established as potent antibacterial agents due to the induced generation of reactive oxygen species (ROS) and the subsequent oxidative stress.[22,23] They can still enter the microorganism's membranes, reacting with the existing phosphate and sulfate groups, impairing their functioning, and consequently leading the microorganism to death.[24,25] ROS can still inhibit the replication activities of DNA/plasmid and some proteins enzymes, due to its interaction with phosphate/sulfate groups or even due to genetic changes.[25,26] All of these results, added to the permeability of ROS under the cell membrane, can affect the expression of proteins essential for the correct functioning of microorganisms, as well as their replication.[24,27–31]

In particular, silver (Ag) is a widely known element for its antimicrobial proper-ties and has been used in colloidal silver compounds or as adsorbed particles in a colloidal carrier.[32] In

addition, Ag nanoparticles (Ag NPs), display the antimicrobial properties of bulk Ag, with a significant reduction in the toxic effects observed with Ag cations.[33–35] The antimicrobial effects of Ag NPs are accomplished by a unique physiochemical property to generate more efficient contact with microorganisms and enhance interactions with microbial proteins.[36] Ag NPs present excellent activity against many kinds of bacteria[37–42] and are capable of disrupting the mitochondrial respiratory chain, leading to the production of ROS[43] and have also demonstrated promising antifungal[44,45] and antiviral capabilities with viruses, such as HIV, Tacaribe virus, and several respiratory pathogens, including adenovirus, parainfluenza and influenza (H3N2).[31,46–49] More specific to antiviral activities, AgNPs are thought to inhibit the entry of the virus into cells due to the binding of envelope proteins, such as glycoprotein gp120, which prevent CD4-dependent virion binding, fusion, and infectivity.[31] In most cases, Ag NPs present the disadvantage of their tendency to agglomerate, leading to a loss of effectiveness. In recent years, the construction of Ag metal/semiconductor composite materials has been identified as a promising strategy for responding to the above problems. Therefore, the strong surface plasmon resonance (SPR) adsorption and high electron trapping ability of Ag NPs are beneficial for promoting the charge transmission bridge.[29,50–55] This modification of Ag NPs by light establishes a coulombic restoring force and prompts a charge density and they are frequently used in plasmonic composites.

Among the large number of metal/semiconductor composites SiO_2-Ag has attracted considerable attention due to its excellent properties, because SiO_2 is thermally stable and highly bioactive, and could not only prevent the agglomeration of particles and enhance the surface hydrophilicity, but also further improves their stability.[56–65] Recently it has been demonstrated that mesoporous silica nanoparticles/Ag composite presents great potential as a candidate for the development of products aiming to prevent the spread of drug-resistant pathogens.[66,67]

An important feature of such materials is the combination of positive properties of the polymer matrix, such as lightness, flexibility, and ease of production, as well as the ability to modify the properties of the material. However, the Ag NPs hosted in SiO_2 have certain drawbacks in relation to their stability. This situation has spurred the study of alternatives allowing a viability for technological applications such as their immobilization in a physical support such as polymer matrix[68,69] and additional reducing agents or capping agents.[70] Polymers displaying antimicrobial properties are the subject of significant attention for their potential technical and medical applications.[71–74] One of the most promising types of such

materials is based on SiO_2-Ag composite immobilized in a polymeric matrix, which have properties that are individually not achievable for each of the components.

Very recently, our research group presented the development and manufacture of materials with anti-SARS-CoV-2 activity, generating potentially safe alternatives for their application, preventing viral proliferation and transmission.[27] Herein we report the results of our studies on the structure and properties of SiO_2-Ag composite immobilized in a polymeric matrix (ethyl vinyl acetate, EVA). Their antibacterial activity towards *Escherichia coli* (*E. coli*) and *Staphylococcus aureus* (*S. aureus*) as well as towards SARS-CoV-2 have been investigated. The synthesized materials were characterized by X-ray diffraction (XRD), field emission scanning electron microscopy (FE-SEM), and micro-Raman spectroscopy. Moreover, their optical properties were investigated by using ultraviolet−visible (UV−vis) spectroscopy. In addition, first-principles calculations within the framework of DFT were employed to obtain atomic-level information on the geometry and electronic structure, local bonding of SiO_2 model and their interaction with O_2 and H_2O. Furthermore, we explored the application of the samples for the photocatalytic activity in the degradation of RhB and trapping experiments have been carried out to understand the radical scavenging behavior. The broad spectrum of interesting properties displayed by such materials offer them opportunities for a multitude of biomedical applications.

Results and Discussion

The X-ray diffraction (XRD) measurements were presented in Figure 1. An analysis of the results renders that the sample SiO_2-Ag has a characteristic peak of amorphous SiO_2 at around $2\theta = 22.2\ °$.[78–81] No additional peak is observed regarding possible Ag phases. For pure EVA, a high crystallinity of the polymer is observed, which is in line with what has been observed in other studies in the literature.[82,83] The SiO_2-Ag particles were added in a polymeric matrix, EVA, which has the role of acting as a carrier. For the EVA-SiO_2-Ag composite, there is an amorphization of the polymeric structure, that is, the symmetry and periodicity break at long-range. This is due to the high degree of disorder of the distorted tetrahedral clusters of [SiO_4] present in amorphous SiO_2,[84] which cause an induction to amorphization of the polymeric EVA chains. As a result of this union, a broadband located at $2\theta = 19.9\ °$ is observed.

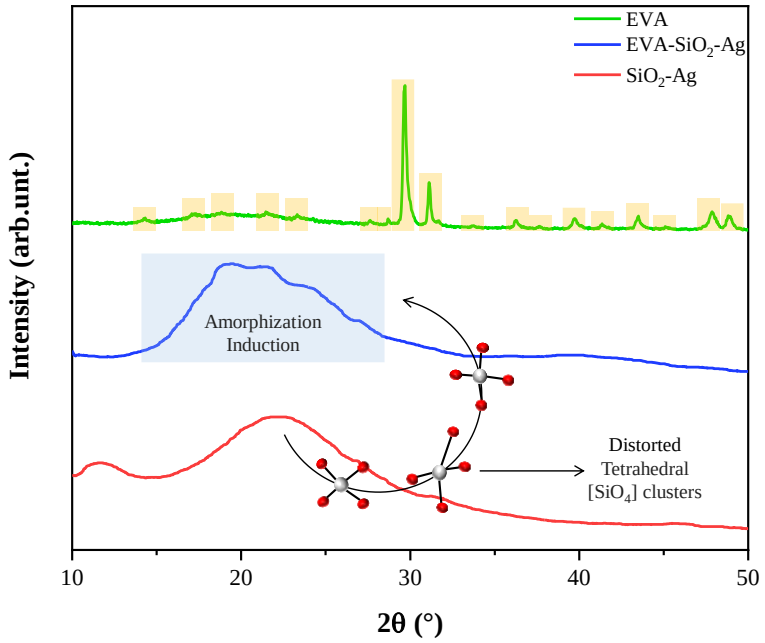

Figure 1 - X-ray diffractograms of SiO_2-Ag, EVA-SiO_2-Ag and EVA samples.

In order to complement the results obtained by XRD, micro-Raman measurements were performed, seeking to analyze the degree of order of the samples at short-range. For the SiO_2-Ag sample, a peak of approximately ~240 cm^{-1} is observed referring to the scissoring of the distorted tetrahedral of the [SiO_4] clusters.[85] For pure EVA, there are five distinct groups of vibrations in the micro Raman spectrum.[86] The vibrations in the range 500-700 cm^{-1} correspond to the deformation movements of the acetate groups of the EVA monomers.[86–88] A set of peaks related to the C-C stretches of the constituent monomers is observed in the range from 750 to 1250 cm^{-1}.[86,89] The peaks between 1300 and 1500 cm^{-1} were ascribed to the bending and twisting vibrations of the ethylene groups in the monomers of EVA.[86,87] Between 1700 and 1900 cm^{-1} the stretches related to C=O bonds are observed.[86,90] At the highest wavelengths, located between 2800 and 3050 cm^{-1}, the C-H aliphatic stretches of the EVA are observed.[87,91] Unlike what was observed in XRD, the composite does not lose its organization at short-range, that is, its constituent monomers maintain their degree of structural order. The SiO_2-Ag mode in the composite can also be observed, indicating a good incorporation in the EVA polymer. According to Shen et al., this mode at ~240 cm^{-1} may also refer to vibrations of the Ag-O bonds, which can be formed from the interaction of the O atoms of the carbonyl groups of the EVA with the Ag contained in SiO_2-Ag.[87]

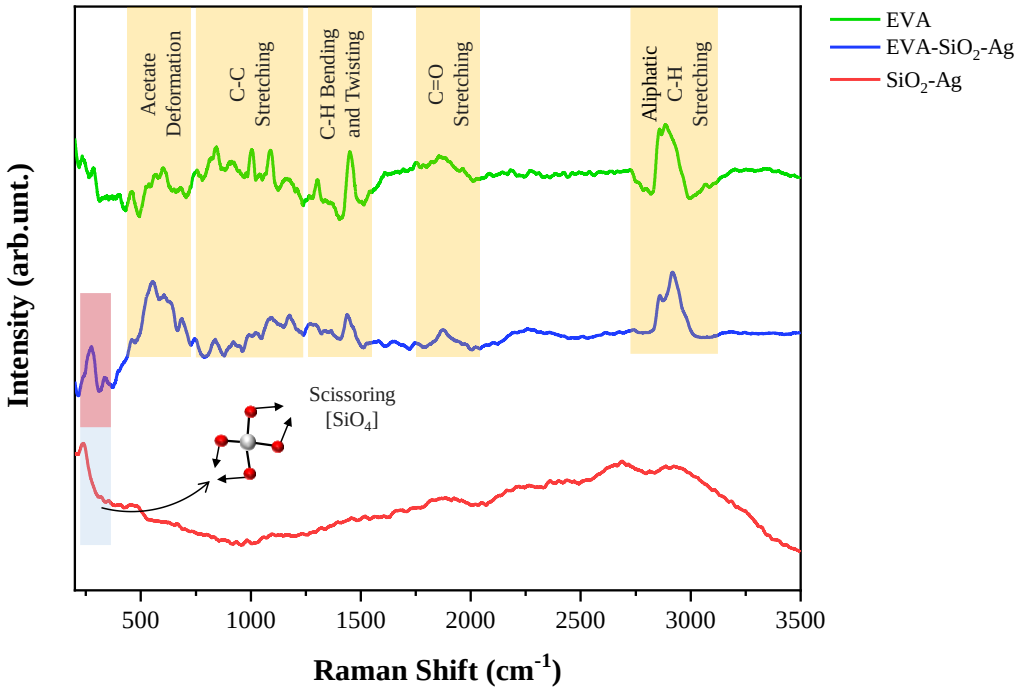

Figure 2 – Micro Raman Spectra of SiO_2-Ag, EVA-SiO_2-Ag and EVA samples.

Fourier transform infrared spectroscopy (FTIR) was performed to analyze changes in the functional groups of the samples and to verify the formation of the composite EVA-SiO_2-Ag. For SiO_2-Ag, there is a broad band located near 3400 cm^{-1} and another located at 1627 cm^{-1}, both corresponding to the O-H stretching of water and the formed silanol groups (Si-OH), respectively.[92,93] The bands observed at 1100 and 475 cm^{-1}, on the other hand are attributed to symmetrical stretching and bending of Si-O-Si bonds, respetively.[92,94,95] The peaks located at 950 and 845 cm^{-1} indicate the bending of the O-Si-O moiety.[80,95] The low intensity mode located at 552 cm^{-1} can be at-tributed to Ag-O stretching, showing the presence of Ag in SiO_2-Ag.[96,97] For EVA, the bands referring to the fingerprint of the polymer are observed at 2954, 2850, 1467, 1243, 874, 707 and 546 cm^{-1} related to the EVA aliphatic groups.[98–102] At 1020 cm^{-1} the bending of the C-O-C bonds is observed[102] and at 1801 and 1739 cm^{-1} the C=O bonds stretching refers to two different types of carbonyl groups,[101,102] as noted by Poljansek et al.[103] For the EVA-SiO_2-Ag composite, changes are observed especially for the stretching of the C=O bonds and throughout the low wavelength region, where the SiO_2 vibrational modes appear. This is because EVA monomers interact through ionic and van der Waals forces with SiO_2 and Ag, observing the overlap of some vibrational modes of the samples and the appearance of new ones. These findings are fingerprints of the interactions between the polymer, at short- and long-range, with the particles of SiO_2 and Ag.

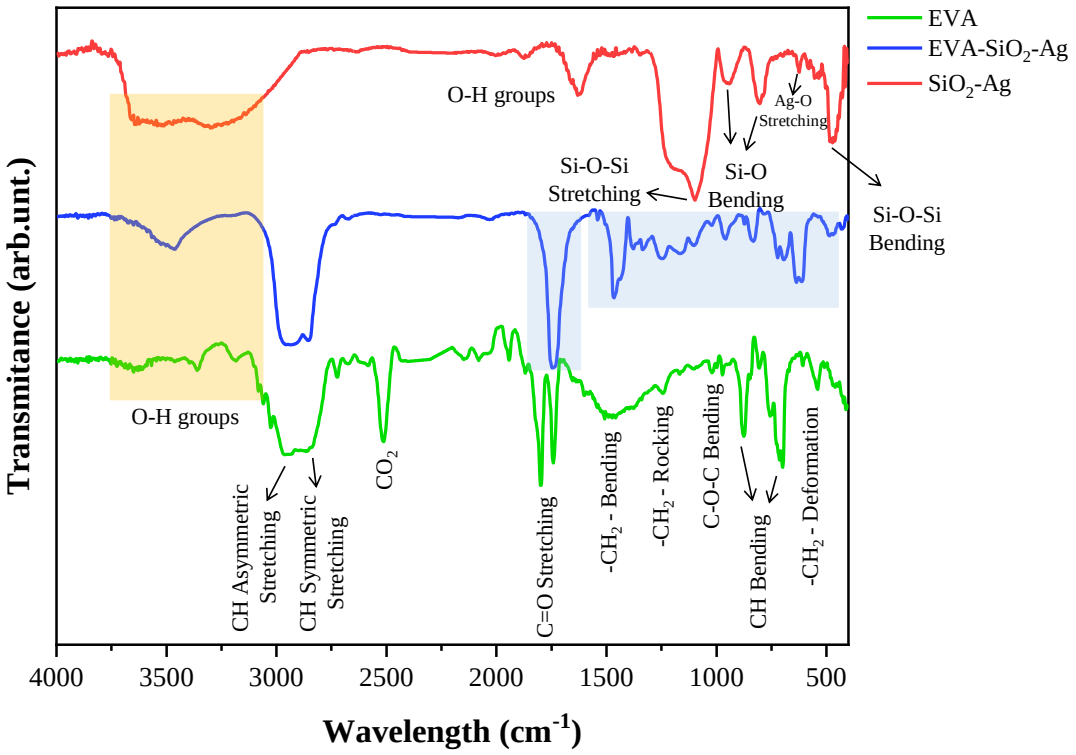

Figure 3 – FTIR spectra of SiO_2-Ag, EVA-SiO_2-Ag and EVA samples.

The thermogravimetric (TG) and differential thermal analysis (DTA) curves are shown in Figure 4. In the SiO_2-Ag sample, a small loss of mass (9.3%) is observed at 50°C, due to the loss of water molecules adsorbed onto the material surface, demonstrating its high thermal stability.[104,105] The degradation of the EVA polymer occurs in two main stages, the first one is due to the loss of acetate groups (between 300 and 400 ° C) and the second one is due to the decomposition of the remaining ethylene groups (between 400 and 650 °C).[106,107] For the composite, there are no significant differences in the TG/DTA profiles compared to the pure polymer, but a slightly smaller loss of mass occurs for this compound (96.8%) than for the EVA (98.2%). This difference is due to the addition of SiO_2-Ag in the polymeric structure, which due to its high thermal stability does not decompose at higher temperatures.

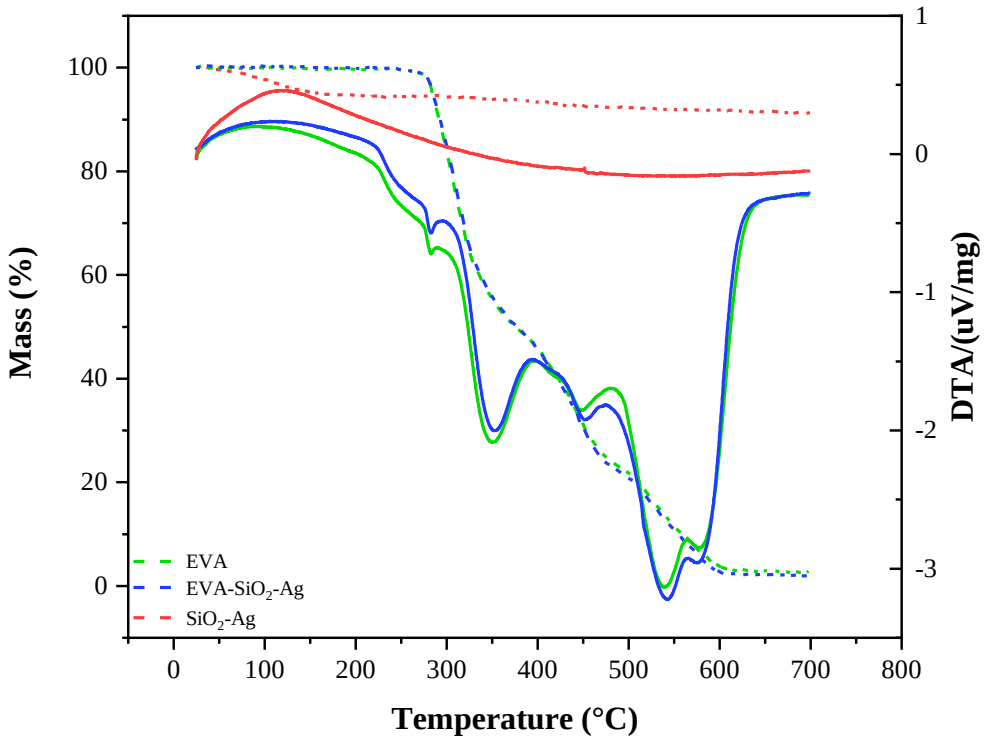

Figure 4 – TG/DTA curves of SiO_2-Ag, EVA-SiO_2-Ag and EVA samples.

Figure 5A shows the diffuse reflectance spectra to pure EVA and EVA-SiO_2-Ag in which a light absorption is observed in the range from 685 to 480 nm attributed to the presence of composite SiO_2-Ag in the polymers blend. The absorptions on near-infrared wavelengths are ascribed to EVA, where the peaks at 1218, 1440 and 1750 nm are the vibrational modes of the C-H groups in the polymers chain, while the absorption from 1780 to 2000 nm is due to the vinyl acetate group.[108–110] The high absorption from 425 nm to ultraviolet wavelengths is attributed to the UV absorber added to the EVA production. The peak at 680 nm is observed for both samples, EVA and EVA-SiO_2-Ag. The broad absorption due to the presence of SiO_2-Ag is ascribed to the Ag_2O nanoparticle in the SiO_2 as shown in Figure 5B. The same effect was observed by Paul et al.[111] to Ag_2O nanoparticles growth on TiO_2 nanorods, in which the composite reduces the bandgap from 2.80 eV (pure TiO_2) to 1.68 eV. In another report, Deng and Zhu[112] produced nanocomposite spheres of $TiO_2/SiO_2/Ag/Ag_2O$ with a bandgap in the range of 2.19-3.01 eV. Although the Ag_2O bulk material shows a bandgap from 1.2 to 1.43 eV,[113] these values depend on the size of the particle, where the smaller the particle the higher its bandgap. Here, the bandgap of the SiO_2-Ag is shown in the inset of Figure 5B calculated

from an indirect interband transition with the value of 1.81 eV. The bandgaps at around 3.03 eV are attributed to the absorption of the UV absorbed added to EVA production. If a direct electronic transition were considered, only the absorption of the UV absorber would be detected due to the drastic decrease of the diffuse reflectance bellow 425 nm. The direct transition presents an average energy of approximately 3.26 eV (Figure 5C).

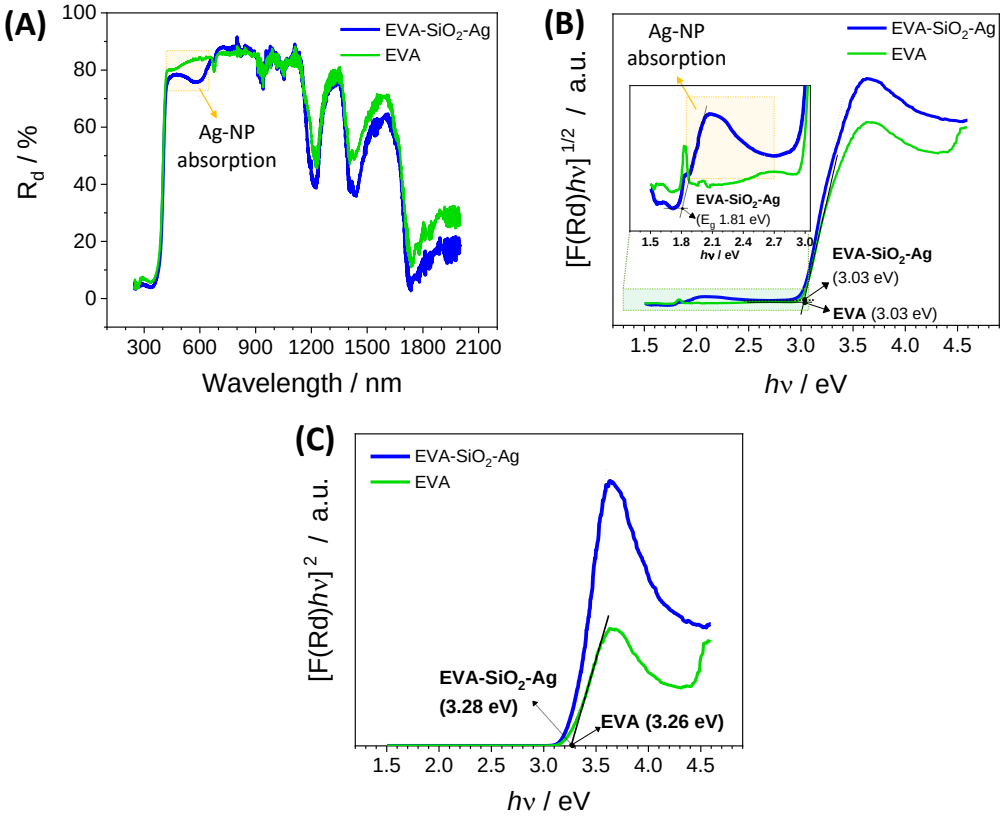

Figure 5 – DRS spectra of SiO_2-Ag, EVA-SiO_2-Ag and EVA samples.

Figure 6 shows the FE-SEM and HR-TEM images for the SiO_2-Ag sample. It is observed that SiO_2 microparticles have no defined morphology, due to their degree of amorphization. In addition, on the surface of the larger particles, the deposition of some NPs with greater contrast is observed, indicating the deposition of Ag NPs on the surface of SiO_2 (Figures 6A-B). To confirm the nature of these deposited NPs, HR-TEM measurements of this sample were performed (Figures 6C-D). As observed in XRD, in the SiO_2 microparticles, crystalline planes are not observed, confirming that they are amorphous. In addition, smaller crystalline particles associated with a high contrast surface are observed, as shown in Figure 6D. Fourier transform (FT) analysis of the crystalline planes of these particles renders that the interplanar distance of 2.35Å was obtained, which is associated with the metallic Ag plane (111) with a cubic structure, according to the card n°44387[114] in the Inorganic Crystal Structure

Database (ICSD), confirming the formation of the SiO_2-Ag interface. From the EDX analysis of the sample, the Si/Ag ratio (wt/wt) of 25.84 was obtained (Figure SI-1).

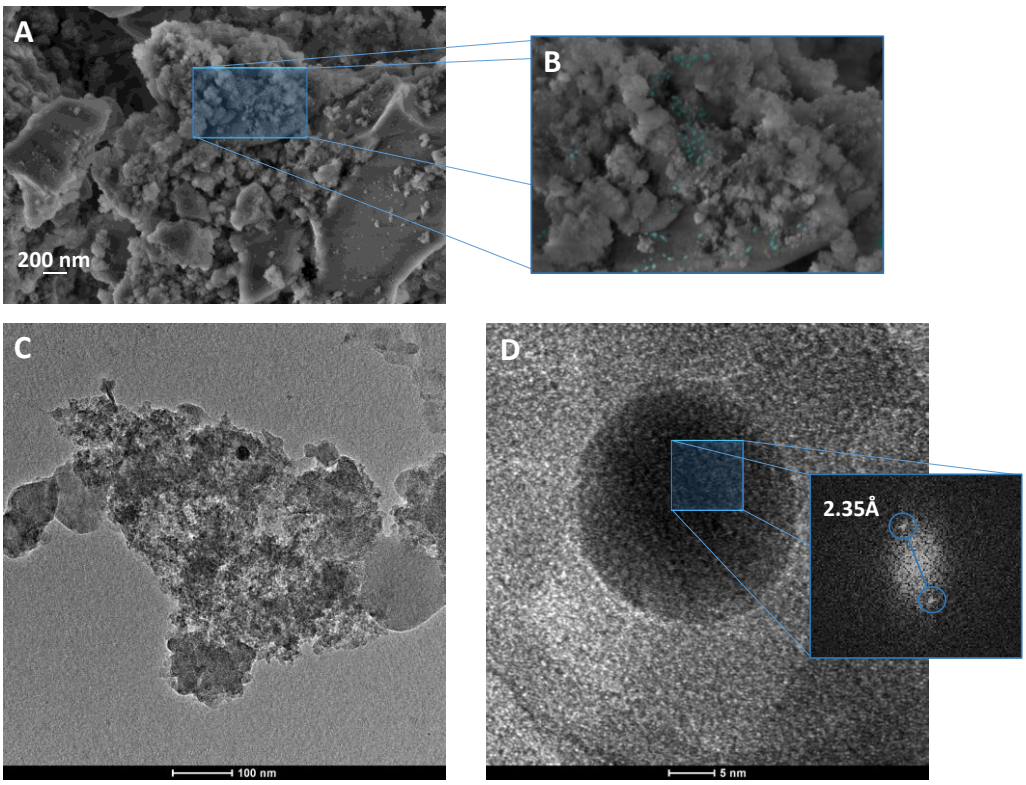

Figure 6 – A-B) FE-SEM images of SiO_2-Ag and C-D) TEM and HR-TEM of SiO_2-Ag sample.

The 2D AFM images shown in Figure 7 present different characteristics after modification of the EVA with the formation of SiO_2-Ag composite. In Figures 7A-B the height and phase contrast profile to sample of EVA without the silica-based composite is exhibited, which provides a surface roughness of 65 nm (root mean square deviation) and a uniform phase contrast with few regions of well-defined contrast. However, the sample EVA-SiO_2-Ag shows a small surface roughness, 32 nm, and well-defined regions of contrast phase (Figures 7D-E). The 3D AFM images clearly display the roughness differences between the EVA and EVA-SiO_2-Ag samples, Figures 7C and 7F, respectively. Moreover, the dark domains in the contrast phase correspond to the SiO_2-Ag composite for Figure 7E and present particles of several size scales distributed in the polymeric matrix. Using the image of EVA-SiO_2-Ag in contrast phase and assuming that all dark domains are SiO_2-Ag composite it is possible to verify the presence of 599 particles on the surface in a size scale span from 30 to 385000 nm^2. The AFM results are in agreement with the FE-SEM images of the polymer samples. The EVA presents a granular morphology, which is caused by the cure of the polymer blend in its extrusion. After the

addition of SiO_2-Ag, a distribution of particles is observed on the surface of the polymer composite in a broad size scale span, which is in accordance with the AFM images. The broad size distribution of the particles was observed by Hui et al.[115] in the investigation of the low-density polyethylene/ethylene vinyl acetate modification with SiO_2. Furthermore, the decrease in the surface roughness with the addition of Ag in polymer matrix was noticed by Filip et al.[116] in their study of polyurethane modified with Ag to produce bionanocomposites.

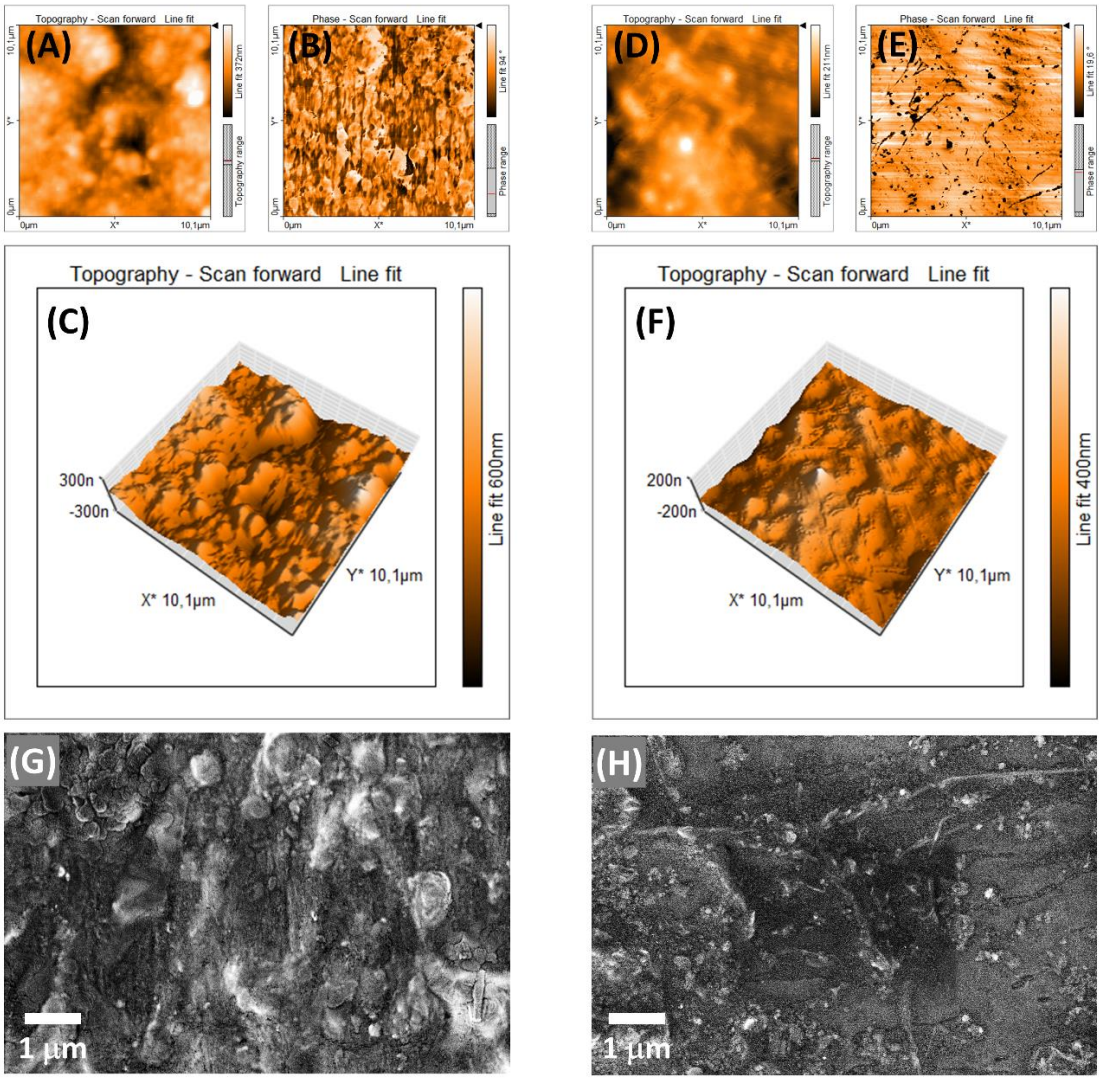

Figure 7 – AFM images of (A, B, C) EVA and (D, E, F) EVA-SiO_2-Ag samples. SEM images of the (G) EVA and (H) EVA-SiO_2-Ag samples.

Once the SiO_2-Ag particles were successfully incorporated into the EVA, microbiological tests were carried out against *E. coli*, *S. aureus* and the SARS-CoV-2 virus, due to the high oxidizing power of the Ag NPs combined with the SiO_2 capacity to produce ROS, which can cause irreversible damage to these microorganisms. The elimination values

against *E. coli* and *S. aureus* are shown in Table 1 and the inhibition values against SARS-CoV-2 in Table 2.

Table 1 - Results of the efficacy evaluation of biocides incorporated into specimens against *S. aureus* (ATCC 6538) and *E. coli* (ATCC 8739).

	EVA		**Eva-SiO_2-Ag**		**Obtained results of reduction from sample with additive in relation to control**	
	Count in CFU*/test piece (recovery)	Count in Log_{10} of CFU*/test piece (recovery)	Count in CFU*/test piece (recovery)	Count in Log_{10} of CFU*/test piece (recovery)	Reduction in Log_{10}	Percent of reduction
S. aureus	5.53×10^5	5.74	$<1.0 \times 10^{-1}$	<1.0	>4.74	>99.99%
E. coli	6.40×10^5	5.80	$<1.0 \times 10^{-1}$	<1.0	>4.80	>99.99%

Table 2 – Copies per mL of SARS-CoV-2 at different times of incubation.

Sample	**Incubation time**	**Day 1**		**Day 2**	
		Copies/mL (SARS-CoV-2)	Viral Inactivation (%)	Copies/mL (SARS-CoV-2)	Viral Inactivation (%)
EVA	2 min	7.68 x 109	-	3.85 x 108	-
EVA-SiO_2-Ag	2 min	7.27 x 107	99.05	2.87 x 106	99.26
EVA	10 min	2.21 x 109	-	5.21 x 108	-
EVA-SiO_2-Ag	10 min	3.28 x 106	99.85	1.98 x 106	99.62

For both bacteria, *E. coli* and *S. aureus*, a 99.99% reduction is observed when in contact with the composite after 24 h of incubation. In contrast to the SARS-CoV-2 virus, 99.05% inactivation is observed in 2 min and 99.85% in 10 min for day 1, and 99.26% in 2 min and 99.62% in 10 min for day 2. In both cases, there was no elimination of microorganisms for pure EVA, that is, without the addition of SiO_2-Ag composite. This behavior proves the synergistic effect of SiO_2 microparticles and Ag NPs with EVA.

The microbicidal tests were performed for the EVA-SiO_2-Ag sample after forced aging by ultraviolet irradiation, following ISO 4892-2: 2013,[117] which aims to reproduce the effects of weathering (temperature, humidity and/or wetting) that occur when materials are exposed in real-life environments to daylight or daylight filtered through window glass. It was observed that after simulating two years of aging (1200 hours of exposure) there is still a 99.950%

reduction in the elimination of S. aureus and E. coli. Thus, the durability defined for the EVA-SiO_2-Ag was minimum two years.

Figure 8 shows the degradation behaviors of the SiO_2-Ag composite. An analysis of the results renders that the SiO_2-Ag sample has a photocatalytic efficiency of 23.7% in 60 min (see the degradation kinetics in Figure SI2), with a reduction of 0.0, 7.3 and 5.7% in the presence of AA, AO and TBA, respectively. These findings render that h•, OH*, and O_2H*, are involved in the photodegradation mechanism. These reactive species appear through the formation of e'-h• pairs generated in the valence band (VB) and conduction band (CB)[118,119] SiO_2-Ag composite, with subsequent reaction with O_2 and H_2O.

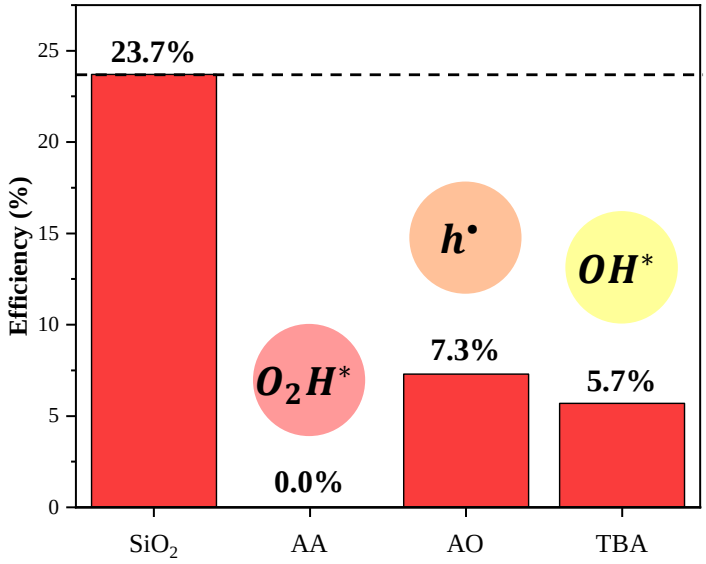

Figure 8 - Comparison of photocatalytic degradation of RhB in the presence of different scavengers under visible light irradiation.

SiO_2 is a n-type semiconductor with a defined electronic structure, band gap, and position of both CB and VB. Considering the close relation between photocatalytic and biocide properties of semiconductors, their activity can be exerted though similar mechanisms. Activations of water (H_2O) and molecular oxygen (O_2) are the most important chemical processes involved in both photocatalytic and biocide activities, and the ROS are the key signaling molecules in both processes. As demonstrated from the results of radical scavengers experiments, SiO_2 interacts with H_2O and O_2 to provoke the formation of ROS OH*and O_2H*.[120–123] and is effective for inhibiting protein adhesion.[124,125]

First principles calculations were performed to analyze the interaction of H_2O and O_2 molecules with the SiO_2 model. We optimize the SiO_2 model and then the map of the molecular

electrostatic potential (MEP) is calculated to investigate the charge transfer process between SiO_2 and H_2O and O_2 and these results are presented in Supplementary Information. The MEP displays the nucleophilic and electrophilic regions where energetically favorable interactions with H_2O and O_2 take place, respectively. At the minima of both interactions there is an electronic charge of 0.04 e- from H_2O to SiO_2 and 0.10 e- from SiO_2 to O_2. These events can be considered the early stages for the formation of OH* and O_2 H*.

The recognized mechanism corresponding to SPR and associated with photoreactivity has not yet been strictly established. In the present study, the proposed photocatalysis and biocide mechanism of SiO_2-Ag composites is summarized in Figure 9. The Ag NPs and SiO_2 particles absorb the incident photons, and the e' in the VB in SiO_2 are excited afterwards. The excited e' moves to the CB; at the same time, the same amount of h• are generated in the VB. Because of the higher work function of Ag compared with that of SiO_2, partially excited e' would transfer from SiO_2 CB to the surface-loaded Ag NPs, since the Fermi energy level of Ag metal is lower than that of SiO_2. When the Ag NPs and the SiO_2 semiconductor come into contact, free electrons migrate from the Fermi level of metallic Ag to the CB of SiO_2 to reach an equilibrium Fermi state. As a subsequence, the whole energy band of the SiO_2 semiconductor is raised up, while that of metallic Ag descends, this leads to the formation of a depletion layer and an internal electrical field at the interface. The migration of e' away from the depleted region causes the creation of excess positive and negative charges on the Ag NPs surface and in the SiO_2 semiconductor, respectively. Thus, the internal electrical field is directed from Ag NP toward the SiO_2 semiconductor. Since the SiO_2-Ag composite is able to absorb the near-ultraviolet to visible light, this helps to absorb more photons, further excite more e' within SiO_2, resulting in accumulating more h•. The e' come up against the O_2 molecule, meanwhile h• would be quenched by H_2O to complete the cycle. Therefore, the biocide activity of SiO_2 would be greatly improved if the Ag NPs were anchored onto SiO_2. To the best of our knowledge, there are still no reports on the utilization of SiO_2-Ag composite to destroy SARS-CoV-2. The SiO_2-Ag composite encapsulated EVA with a narrow band gap not only efficiently increases the e' flow of the SiO_2 but also largely facilitates the charge separation. The subsequent deposition of Ag NPs promotes electron transfer ability, which leads to higher biocide activity. Moreover, the contact of Ag NPs with the surface of the semiconductor SiO_2 can result in an electron-enhanced area in their interface that could effectively facilitate the uptake of electrons and then improve the reduction activity. These reactions can be increased due to the formation of an intense local electric field close to the surface of the Ag NPs (SPR effect) (Figure 9A). At the Ag-semiconductor interface the number of charge carriers is greater due to the generated

electric field, increasing the corresponding separation process (Figure 9B). On the other hand, the interaction with the e' in a cluster is represented by the transition of e' from occupied to unoccupied states in the band structure. The occupied states are below the Fermi level, and the unoccupied states are mostly above the Fermi level. In the specific case of bacteria, fungi and viruses, there is the interaction of the region of lower electronic density of the crystal surface with H_2O. In this interaction, H_2O loses an e' forming a hydroxyl radical OH* and a proton H•. Simultaneously, an e' is transferred to the O_2 molecule, forming the superoxide anion O_2'. This ion in turn, to maintain the balance of charge and mass, interacts with the H• forming the hydrogen peroxide radical O_2H*. The results summarized above can be exemplified in Figure 9C.

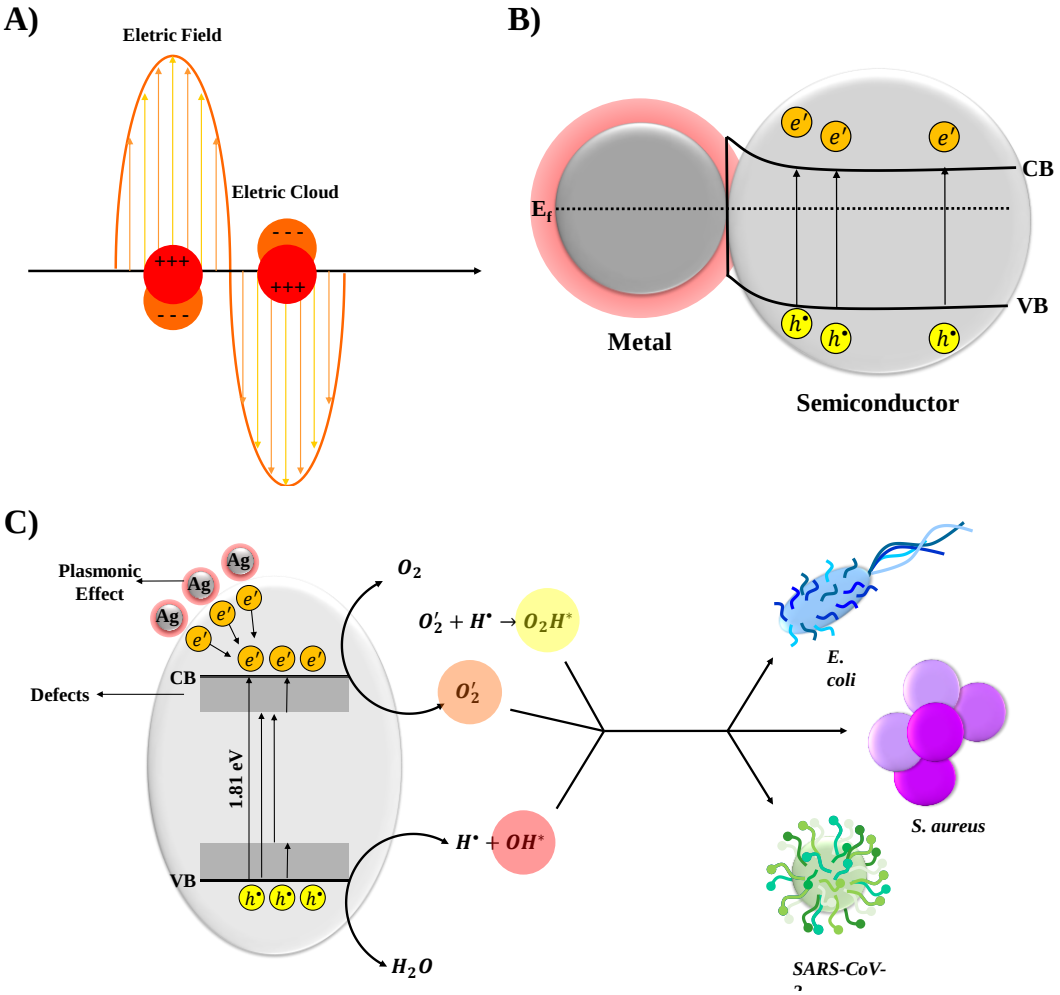

Figure 9 – A schematic representation of plasmon-induced hot electrons over SiO_2-Ag composite: A) At Ag NPs particles; B) At metal-semiconductor; and C) Proposed mechanism for biocide activity. (CB and VB represent the conduction band and valence band, respectively).

Conclusions

Developing new technologies for constructing highly efficient biocide materials, in particular coating strategies to prevent SARS-CoV-2, is of great significance. Here, a plasmonic SiO_2-Ag composite immobilized in polymeric matrix (ethyl vinyl acetate) was successfully prepared and the as-fabricated samples exhibited high antibacterial activity towards *Escherichia coli* (*E. coli*) and *Staphylococcus aureus* (*S. aureus*) as well as towards SARS-CoV-2. The enhancement is mainly due to the SPR effect of the Ag NPs anchored onto the SiO_2. Considering the close relation between photocatalytic and biocide properties of semiconductors, their activity can be exerted though similar mechanisms. The active species trapping experiments suggested that h•, OH*, and O_2H* were the main active species for the photocatalytic degradation of RhB and biocide activity. Given that EVA has high mechanical resistance and stability to water and heat and that the procedure for obtaining the composites is simple and uses low-cost reagents, the SiO_2-Ag composite has potential advantages for its application as a material biocide, and the elimination of SARS-CoV-2. Finally, we propose emerging technologies that have not yet been used for bactericide/virucide purposes but hold great promise and potential for the future engineering of biocide surfaces. This is the case of the reusable mask manufactured using the EVA-SiO_2-Ag composite presented here, which has high durability, requiring only the replacement of its filters to have a technology applicable to current demands (Figure 10).

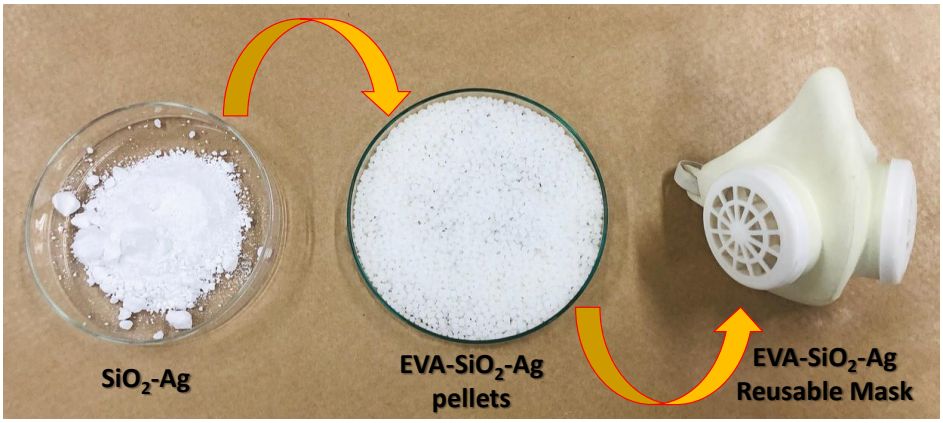

Figure 10 – Reusable mask manufactured using the EVA-SiO_2-Ag composite.

Materials and Methods

Synthesis Ag NPs: Briefly, silver nitrate (850 mg, $AgNO_3$, Cennabras, 99.8%) was dissolved in 100 ml of deionized water at 90°C and stirred until complete dissolution. Subsequently 1.0 ml of sodium citrate ($C_6H_5Na_3O_7$, Sigma-Aldrich, 98%) diluted in water (1% [wt/wt]) was added and the transparent solution converted to yellowish-green colloid, which

indicated the formation of Ag NPs. After 1 h, the colloidal dispersion was mixed with 11g of amorphous SiO_2 (Sigma-Aldrich, USA) and dried at 125°C in a conventional oven.

Preparation of EVA-SiO_2-Ag Composite: EVA 3019, melt index 2.5 g/10 min, was purchased from Braskem. EVA-SiO_2-Ag masterbatch was prepared by incorporation in the molten state processing of the SiO_2-Ag into the EVA using a co-rotational twin-screw extruder Plastic AX, Brazil. Mineral oil was used as a compatibilizer agent to prevent agglomeration and to provide uniform distribution of the SiO_2-Ag into EVA matrix. Then, 1% in weight of mineral oil (USP Grade, Anastacio Chemistry, Brazil) was firstly dispersed in the polymer by drumming for 20 minutes at 15 Hz. Subsequently, 10% in weight of SiO_2-Ag was added to the mixing drum and the process was kept for an additional time of 20 min. The processing extrusion temperature was 140°C. To examine the antimicrobial properties of a typical application product, EVA-SiO_2-Ag composite samples were produced using a thermoplastic injection-molding process. Test samples were produced by dry blending the EVA polymer with the required amount of masterbatch containing the SiO_2-Ag additive, which was followed by injection molding. The samples were 50 by 50 by 1.5 mm and contained the melt-blended EVA composite masterbatch (10% [wt/wt], corresponding to approximately 50 ppm Ag).

Characterizations: The samples were structurally characterized by XRD using a D/Max-2500PC diffractometer (Rigaku,) with Cu Kα radiation (λ = 1.5406 Å) in the 2θ range of 10 - 50° and a scanning speed of 1° min^{-1}. Furthermore, micro-Raman spectra were recorded using the iHR550 spectrometer (Horiba Jobin-Yvon) coupled with a Silicon CCD detector and an argon-ion laser (Melles Griot, USA), which operated at 514.5 nm with a maximum power of 200 mW; moreover, a fiber optic microscope was also employed. Fourier-transform infrared spectroscopy (FT-IR, Bruker Vector 22 FTIR) of the samples was recorded at 400–4000 cm^{-1}. UV-Vis diffuse reflectance measurements were obtained using a Varian Cary spectrometer model 5G in the diffuse reflectance mode, with a wavelength range of 2000 to 250 nm and a scan speed of 300 nm min-1. An analysis of the thermal stability of samples was conducted on a thermogravimetric analyzer (NETZSCH—409 Cell) from 30 to 700 °C at a heating rate of 10 °C min^{-1} and in an oxidizing atmosphere (O2) with 50 mL min^{-1} flux. The morphologies, textures, and sizes of the samples were observed with a FE-SEM, which operated at 2 kV (Supra 35-VP, Carl Zeiss). A Jem-2100 LaB6 (Jeol) high resolution-transmission electron microscope (HR-TEM) with an accelerating voltage of 200 kV coupled with an INCA Energy TEM 200 (Oxford) was used to obtain larger magnifications and to clearly verify the samples. AFM images were obtained using a Flex-AFM controlled by Easyscan 2 software (Nanosurf, Switzerland) in contrast phase mode on active vibration isolation table (model TS-150, Table

Stable LTD®). The cantilever used for image acquisition was the silicon Tap190G (Resonant frequency 190 kHz, force constant 48 N/m, Budget Sensors) in setpoint of 50%.

Bactericidal Tests: The bactericidal activity towards *E. coli* and *S. aureus* of the pure polymer and the composite with SiO_2-Ag was carried out according to the standard test methodology described in ISO 22196 - Measurement of antibacterial activity on plastics and other non-porous surfaces[75], carried out in Nanox's microbiology laboratory. A 100μL volume of the bacterial solution (in a concentration of 105 CFU/ml) was inoculated in triplicate over the surface of the samples. The inoculum was then covered with a sterile plastic film which was gently pressed to be distributed throughout the sample area. Samples were incubated in a bacteriological oven at 36°C for 24 h at 90% humidity. After incubation, the inoculum was recovered with 10 mL of SCDLP broth followed by serial dilution to 10^{-4} in PBS buffer. One mL of each dilution was plated with Standard Count Agar by Pour Plate. After solidification of the culture medium, the Petri dishes were incubated in the inverted position in a bacteriological oven at 36°C for 24 h. The logarithmic reduction and percentage reduction by the CFU/mL count were then determined by the following equation:

$$R = (U_t - U_0) - (A_t - U_0) = U_t - A_t$$

where R is the antibacterial activity; U_0 is the average of the common logarithm of the number of viable bacteria, in cells/cm^2, recovered from the untreated test specimens immediately after inoculation; U_t is the average of the common logarithm of the number of viable bacteria, in cells/cm^2, recovered from the untreated test specimens after 24 h and A_t is the average of the common logarithm of the number of viable bacteria, in cells/cm^2, recovered from the treated test specimens after 24 h.

Antiviral Tests: The antiviral activity of the pure polymer and the composite with SiO_2-Ag was carried out by adapting the standard model ISO 21702 - Measures of antiviral activity on plastics and other non-porous surfaces[76] and the method used by Tremiliosi et al.[27] The tests were carried out in a NB3 (biosafety level 3) laboratory at the University of São Paulo, following the recommendations of ANVISA. The SARS-CoV-2 was inoculated into liquid media, EVA polymer and the EVA-SiO_2-Ag composite samples were incubated for 2 different time intervals (2 and 10 min). Then, they were seeded in Vero CCL-81 cell cultures. After incubation, the viral genetic material was quantified by quantitative PCR in real time and based on the control, the ability of each sample to inactivate SARS-CoV-2 was determined.

Reactive oxygen species (ROS) identification: To investigate the active species generated in the photocatalytic RhB (Aldrich, 95%) degradation process over SiO_2-Ag composite, a trapping experiment was conducted with ascorbic acid (AA), ammonium oxalate (AO) and tert-butyl alcohol (TBA) as the capture agent of hydroxyl radical OH*, hole, h•, and hydroperoxyl radical O_2H*, respectively. The trapping experimental procedure was identical to photocatalytic degradation except that an additional capture agent was added each time. In this way, 50 mg of the sample was dispersed in 50 ml of RhB solution (1×10^{-5} M), and it was kept in the dark for 30 min at 20 ° C and then 6 visible lamps (Philips TL-D, 15W) were switched on. After 60 minutes, an aliquot was removed and centrifuged to obtain only the liquid phase. The variations in the standard absorption of RhB (554 nm) were made through analysis of absorption spectroscopy in the UV-Vis region on a V-660 spectrophotometer (JASCO).

Computational Method: The calculations were performed with the Gaussian 09 package[77] by using the density functional theory (DFT), with the hybrid functional B3LYP and 6-31 ++ G ** basis set. In the supplementary material the model systems employed in this study are presented. An analysis based on the results of the natural bond orbital (NBO) method (Reed et al.) and the map electrostatic potential (MEP) is employed to investigate the charge transfer process between SiO_2 model and O_2 and H_2O.

Supplementary Materials: The following are available online at https://www.mdpi.com/2079-4991/11/3/638/s1, Figure S1 Chemical composition from EDX analysis of the SiO_2-Ag; Figure S2 (A) Relative concentration of RhB dye (C_n/C_0). (B) Reaction kinetics of the RhB degradation $-l_n(C_n/C_0)$ versus time (min) for SiO_2-Ag composite; Figure S3. Schematic representation of the different rings used for modeling SiO_2. Silicon (yellow) and Oxygen (red); Figure S4. The optimized SiO_2 model used in the calculations; Table S1 Bond angles and lengths of the structure used; Figure S5. MEP (in eV) of SiO_2 model.

Author Contributions: M.A., L.G.P.S., G.C.T., D.C., D.T.M., R.I.S., D.C.B.V., J.R.d.S., L.K.R. and J.A., conceptualization, methodology, validation, formal analysis, investigation, data curation, writing—original draft preparation, writing—review and editing; I.L.V.R., L.H.M., J.A. and E.L., conceptualization, writing—review and editing, supervision. All authors have read and agreed to the published version of the manuscript.

Funding: This research was funded by Fundação de Amparo à Pesquisa do Estado de São Paulo—FAPESP (FAPESP CEPID—finance code 2013/07296-2, FAPESP/SHELL—finance code 2017/11986-5 and PIPE—finance codes 15/50113-3 and 11/51084-4), FINEP (finance code 03/2013 Ref. 0555/13), Conselho Nacional de Desenvolvimento Cientifico e

Tecnológico—CNPq (finance code 166281/2017-4), CAPES (finance code 001), Universitat Jaume I (project UJI-B2019-30), and the Ministerio de Ciencia, Innovación y Universidades (Spain) (project PGC2018094417-B-I00).

Data Availability Statement: The data that support the findings of this study are available from the corresponding author: J.A., upon reasonable request.

Conflicts of Interest: The authors declare no conflict of interest.

References

World Health Organization Infection Prevention and Control during Health Care When Novel Coronavirus (nCoV) Infection is Suspected—Interim Guidance.

1. Li, G.; De Clercq, E. Therapeutic options for the 2019 novel coronavirus (2019-nCoV). *Nature Reviews Drug Discovery* **19**, 149–150, 2020.
2. Wang, M. et al. Remdesivir and chloroquine effectively inhibit the recently emerged novel coronavirus (2019-nCoV) in vitro. *Cell Research* **30**, 269–271, 2020.
3. Colson, P. et al. Chloroquine and hydroxychloroquine as available weapons to fight COVID-19. *International Journal of Antimicrobial Agents* **55**, 105932, 2020.
4. Gao, J.; Tian, Z.; Yang, X. Breakthrough: Chloroquine phosphate has shown apparent efficacy in treatment of COVID-19 associated pneumonia in clinical studies. *Bioscience Trends* **16**, 72-73, 2020.
5. Weiss, C. et al. Toward Nanotechnology-Enabled Approaches against the COVID-19 Pandemic. *ACS Nano* **14**, 6383–6406, 2020.
6. Sportelli, M.C. et al. Can Nanotechnology and Materials Science Help the Fight against SARS-CoV-2? *Nanomaterials* **10**, 802, 2020.
7. Tharayil, A. et al. A short review on nanotechnology interventions against COVID-19. *Emergent Materials*, 2021.
8. Luo, W. et al. The role of absolute humidity on transmission rates of the COVID-19 outbreak. *medRxiv* 2020.
9. Chin, A. et al. Stability of SARS-CoV-2 in different environmental conditions. *medRxiv* 2020.
10. van Doremalen, N. et al. Aerosol and Surface Stability of SARS-CoV-2 as Compared with SARS-CoV-1. *New England Journal of Medicine* **382**, 1564–1567, 2020.
11. Fathizadeh, H. et al. Protection and disinfection policies against SARS-CoV-2 (COVID-19). *Le Infezioni in Medicina* **28**, 185–191, 2020.
12. Derraik, J.G.B. et al. Rapid Review of SARS-CoV-1 and SARS-CoV-2 Viability, Susceptibility to Treatment, and the Disinfection and Reuse of PPE, Particularly Filtering Facepiece Respirators. *International Journal of Environmental Research and Public Health* **17**, 6117, 2020.
13. Behzadinasab, S. et al. A Surface Coating that Rapidly Inactivates SARS-CoV-2. *ACS Applied Matererials & Interfaces* **12**, 34723–34727, 2020.
14. Kampf, G. Potential role of inanimate surfaces for the spread of coronaviruses and their inactivation with disinfectant agents. *Infection Prevention in Practice* **2**, 100044, 2020.
15. Kampf, G. et al. Persistence of coronaviruses on inanimate surfaces and their inactivation with biocidal agents. *Journal of Hospital Infection* **104**, 246–251, 2020.
16. Otter, J.A. et al. Transmission of SARS and MERS corona-viruses and influenza virus in healthcare settings: the possible role of dry surface contamination. *Journal of Hospital Infection* **92**, 235–250, 2016.
17. Lancet, T. COVID-19: protecting health-care workers. *Lancet* **395**, 922, 2020.

18. Imani, S.M. et al. Antimicrobial Nanomaterials and Coatings: Current Mechanisms and Future Perspectives to Control the Spread of Viruses Including SARS-CoV-2. *ACS Nano* **14**, 12341–12369, 2020.
19. Ghaffari, M. et al. An overview of the use of biomaterials, nanotechnology, and stem cells for detection and treatment of COVID-19: towards a framework to address future global pandemics. *Emergent Materials* 1–16, 2021.
    Basak, S.; Packirisamy, G. Nano-based antiviral coatings to combat viral infections. *Nano-Structures & Nano-Objects* **24**, 100620, 2020.
20. Podder, S. et al. Superb hydroxyl radical-mediated biocidal effect induced antibacterial activity of tuned ZnO/chitosan type II heterostructure under dark. *Journal Nanoparticle Research* **18**, 294, 2016.
21. Lakshmi Prasanna, V.; Vijayaraghavan, R. Insight into the Mechanism of Antibacterial Activity of ZnO: Surface Defects Mediated Reactive Oxygen Species Even in the Dark. *Langmuir* **31**, 9155–9162, 2015.
22. Alkhouri, N.; Zein, N.N. Protease inhibitors: Silver bullets for chronic hepatitis C infection? *Cleveland Clinic Journal of Medicine* **79**, 213–222, 2012.
23. Kehrer, J.P. The Haber–Weiss reaction and mechanisms of toxicity. *Toxicology* 149, 43–50, 2000.
24. Durãn, N. et al. Potential use of silver nanoparticles on pathogenic bacteria, their toxicity and possible mechanisms of action. *Journal of the Brazilian Chemical Society* 21, 949–959, 2010.
25. Tremiliosi, G.C. et al. Engineering polycotton fiber surfaces, with antimicrobial activity against *S. aureus*, *E. Coli*, *C. albicans* and SARS-CoV-2. *Japan Journal of Medical Science* **1**, 47-58, 2020.
26. Assis, M. et al. Towards the scale-up of the formation of nanoparticles on α-Ag_2WO_4 with bactericidal properties by femtosecond laser irradiation. *Scientific Reports* **8**, 1–11, 2018.
27. Assis, M. et al. Ag Nanoparticles/AgX (X=Cl, Br and I) Composites with Enhanced Photocatalytic Activity and Low Toxicological Effects. *ChemistrySelect* **5**, 4655–4673, 2020.
28. Akbarzadeh, A. et al. An overview application of silver nanoparticles in inhibition of herpes simplex virus. *Artificial Cells, Nanomedicine, and Biotechnology* **46**, 263–267, 2018.
29. Lara, H.H. et al. Mode of antiviral action of silver nanoparticles against HIV-1. J. *Nanobiotechnology* **8**, 1, 2010.
30. Silvestry-Rodriguez, N. et al. Silver as a Disinfectant BT - Reviews of Environ-mental Contamination and Toxicology. In; Springer New York: New York, NY, 2007; pp. 23–45.
31. Kędziora, A. et al. Similarities and Differences be-tween Silver Ions and Silver in Nanoforms as Antibacterial Agents. *International Journal of Molecular Sciences* 19, 2018.
32. Beer, C.; Foldbjerg, R.; Hayashi, Y.; Sutherland, D.S.; Autrup, H. Toxicity of silver nanoparticles—Nanoparticle or silver ion? Toxicology Letters **208**, 286–292, 2012.
33. Pauksch, L. et al. Biocompatibility of silver nanoparticles and silver ions in primary human mesenchymal stem cells and osteoblasts. *Acta Biomaterialia* **10**, 439–449, 2014.
34. Wei, L. et al. Silver nanoparticles: synthesis, properties, and therapeutic applications. *Drug Discovery Today* **20**, 595–601, 2015.
35. Wang, Z. et al. Embedding ultrasmall Ag nanoclusters in Luria-Bertani extract via light irradiation for enhanced antibacterial activity. *Nano Research* **13**, 203–208, 2020.

36. Monerris, M. et al. Highly effective antimicrobial nanocomposites based on hydrogel matrix and silver nanoparticles: long-lasting bactericidal and bacteriostatic effects. *Soft Matter* **15**, 8059–8066, 2019.
37. Luo, S. et al. In situ and controllable synthesis of Ag NPs in tannic acid-based hyperbranched waterborne polyurethanes to prepare antibacterial polyurethanes/Ag NPs composites. *RSC Advances* 8, 36571–36578, 2018.
38. Jeremiah, S.S. et al. Potent antiviral effect of silver nanoparticles on SARS-CoV-2. *Biochemical and Biophysical Research Communications* **533**, 195–200, 2020.
39. Burdușel, A.C. et al. Biomedical Applications of Silver Nanoparticles: An Up-to-Date Overview. *Nanomaterials* **8**, 681, 2018.
40. Bhakya, S. et al. Biogenic synthesis of silver nanoparticles and their anti-oxidant and antibacterial activity. *Applied Nanoscience* **6**, 755–766, 2016.
41. AshaRani, P. V. et al. Cytotoxicity and Genotoxicity of Silver Nanoparticles in Human Cells. *ACS Nano* **3**, 279–290, 2009.
42. Lara, H.H. et al. Effect of silver nanoparticles on *Candida albicans* biofilms: an ultrastructural study. *Journal of Nanobiotechnology* **13**, 91, 2015.
43. Kim, K.J. et al. Antifungal activity and mode of action of silver nano-particles on Candida albicans. *BioMetals* **22**, 235–242, 2009.
44. Chen, N. et al. Inhibitory effects of silver nanoparticles against adenovirus type 3 in vitro. *Journal of Virological Methods* **193**, 470–477, 2013.
45. Gaikwad, S. et al. Antiviral activity of mycosynthesized silver nanoparticles against herpes simplex virus and human parainfluenza virus type 3. *International Journal of Nanomedicine* **8**, 4303–4314, 2013.
46. Speshock, J.L. et al. Interaction of silver nanoparticles with Tacaribe virus. *Journal Nanobiotechnology* 8, 19, 2010.
47. Xiang, D. et al. Inhibition of A/Human/Hubei/3/2005 (H3N2) influenza virus infection by silver nanoparticles in vitro and in vivo. *International Journal Nanomedicine* **8**, 4103–4114, 2013.
48. Huo, Y. et al. Ag SPR-promoted 2D porous g-C_3N_4/Ag_2MoO_4 composites for enhanced photocatalytic performance towards methylene blue degradation. *Applied Surface Science* 459, 271–280, 2018.
49. Zhang, Z. et al. Photocatalysis Coupled with Thermal Effect Induced by SPR on Ag-Loaded Bi_2WO_6 with Enhanced Photocatalytic Activity. *The Journal of Physical Chemistry C* **116**, 25898–25903, 2012.
50. Mitsushio, M.; Miyashita, K.; Higo, M. Sensor properties and surface characterization of the metal-deposited SPR optical fiber sensors with Au, Ag, Cu, and Al. *Sensors Actuators A Physics* **125**, 296–303, 2006.
51. Vasa, P.; Lienau, C. Strong Light–Matter Interaction in Quantum Emitter/Metal Hybrid Nanostructures. *ACS Photonics* **5**, 2–23, 2018.
52. Kim, S.M. et al. The effect of hot electrons and surface plasmons on heterogeneous catalysis. *Journal of Physics: Condensed Matter* **28**, 254002, 2016.
53. Wang, Z. et al. Manipulation of charge transfer and transport in plasmonic-ferroelectric hybrids for photoelectrochemical applications. *Nature Communications* **7**, 10348, 2016.
54. Jeon, H.J.; Yi, S.C.; Oh, S.G. Preparation and antibacterial effects of Ag–SiO_2 thin films by sol–gel method. *Biomaterials* **24**, 4921–4928, 2003.
55. Zhang, Y. et al. Hierarchically-structured SiO_2-Ag@TiO_2 hollow spheres with excellent photocatalytic activity and recyclability. *Journal Hazardous Materials* **354**, 17–26, 2018.

56. Chi, Y. et al. Synthesis of Fe_3O_4@SiO_2–Ag magnetic nanocomposite based on small-sized and highly dispersed silver nanoparticles for catalytic reduction of 4-nitrophenol. *Journal of Colloid Interface Science* 383, 96–102, 2012.
57. He, Y. et al. New Application of Z-Scheme Ag_3PO_4/g-C_3N_4 Composite in Converting CO_2 to Fuel. *Environmental Science & Technology* **49**, 649–656, 2015.
58. Zeng, J.; Xuan, Y. Enhanced solar thermal conversion and thermal conduction of MWCNT-SiO_2/Ag binary nanofluids. *Applied Energy* **212**, 809–819, 2018.
59. Gu, G. et al. Synthesis and antibacterial property of hollow SiO_2/Ag nanocomposite spheres. *Journal of Colloid Interface Science* **359**, 327–333, 2011.
60. Flores, J.C. et al. Preparation of core–shell nanospheres of silica–silver: SiO_2@Ag. *Journal of Non-Crystalline Solids* **354**, 5435–5439, 2008
61. Lambert, S. et al. Synthesis of Pd/SiO_2, Ag/SiO_2, and Cu/SiO_2 cogelled xerogel catalysts: study of metal dispersion and catalytic activity. *Journal Catalysis* **221**, 335–346, 2004.
62. Liu, C.; Yang, D.; Jiao, Y.; Tian, Y.; Wang, Y.; Jiang, Z. Biomimetic Synthesis of TiO2–SiO2–Ag Nanocomposites with Enhanced Visible-Light Photocatalytic Activity. ACS Appl. Mater. Interfaces 2013, 5, 3824–3832, doi:10.1021/am4004733.
63. Deng, Z.; Chen, M.; Wu, L. Novel Method to Fabricate SiO2/Ag Composite Spheres and Their Catalytic, Surface-Enhanced Raman Scattering Properties. J. Phys. Chem. C 2007, 111, 11692–11698, doi:10.1021/jp073632h.
64. Abduraimova, A.; Molkenova, A.; Duisembekova, A.; Mulikova, T.; Kanayeva, D. Cetyltrimethylammonium Bromide (CTAB)-Loaded SiO2–Ag Mesoporous Nanocomposite as an Efficient Antibacterial Agent. 2021, 11, 477. doi.org/10.3390/nano11020477
65. Liu, J.; Li, S.; Fang, Y.; Zhu, Z. Boosting antibacterial activity with mesoporous silica nanoparticles supported silver nanoclusters. *Journal Colloid Interface Science* **555**, 470–479, 2019.
66. Fullenkamp, D.E.; et al. Mussel-inspired silver-releasing antibacterial hydrogels. *Biomaterials* **33**, 3783–3791, 2012.
67. Otari, S. V. et al. A novel microbial synthesis of catalytically active Ag–alginate biohydrogel and its antimicrobial activity. *Dalton Transactions* **42**, 9966–9975, 2013.
68. Rawat, K.A. et al. Mg^{2+} ion as a tuner for colorimetric sensing of glyphosate with improved sensitivity via the aggregation of 2-mercapto-5-nitrobenzimidazole capped silver nanoparticles. *RSC Advances* **6**, 47741–47752, 2016.
69. Hassanien, R. et al. Preparation and Characterization of Conductive and Photoluminescent DNA-Templated Polyindole Nanowires. *ACS Nano* 4, 2149–2159, 2010.
70. Shoeb, M. et al. In Vitro and in Vivo Antimicrobial Evaluation of Graphene–Polyindole (Gr@PIn) Nanocomposite against Methicillin-Resistant *Staphylococcus aureus* Pathogen. *ACS Omega* 3, 9431–9440, 2018.
71. Xiao, W. et al. Antibacterial hybrid materials fabricated by nanocoating of microfibril bundles of cellulose substance with titania/chitosan/silver-nanoparticle composite films. *Journal Materials Chemistry B* **1**, 3477–3485, 2013.
72. Liang, X. et al. Preparation and antibacterial activities of polyaniline/$Cu_{0.05}Zn_{0.95}O$ nanocomposites. *Dalton Transactions* **41**, 2804–2811, 2012.
73. ISO 22196 - Measurement of antibacterial activity on plastics and other non-porous surfaces. 2019.
74. ISO 21702 - Measurement of antiviral activity on plastics and other non-porous surfaces. 2019.
75. Frisch, M.J. et al. Gaussian 09 2016.

76. Tinio, J.V.G. et al. Influence of OH^- Ion Concentration on the Surface Morphology of ZnO-SiO_2 Nanostructure. *Journal of Nanotechnolology* **2015**, 686021, 2015.
77. Ferreira, C.S. et al. Rice Husk Reuse in the Preparation of SnO_2/SiO_2 Nanocomposite. *Materials Research* **18**, 639–643, 2015.
78. Tran, T.N. et al. Synthesis of amorphous silica and sulfonic acid function-alized silica used as reinforced phase for polymer electrolyte membrane. *Advances in Natural Sciences: Nanoscience and Nanotechnology* **4**, 45007, 2013.
79. Musi, S. et al. Precipitation of amorphous SiO_2 particles and their properties. *Brazilian Journal Chemical Engineering* 28, 89–94, 2011.
80. He, X. et al. Study on orientation in EVA/Fe_3O_4 composite hot-melt adhesives. *International Journal of Adhesion and Adhesives* **44**, 9–14, 2013.
81. Bidsorkhi, H.C. et al. Mechanical, thermal and flammability properties of ethylene-vinyl acetate (EVA)/sepiolite nanocomposites. *Polymer Testing* **37**, 117–122, 2014.
82. Hoang, V. Molecular Dynamics Simulation of Amorphous SiO_2 Nanoparticles. *The Journal of Physical Chemistry B* **111**, 12649–12656, 2007.
83. Borowicz, P. et al. Raman Spectra of High-κ Dielectric Layers Investigated with Micro-Raman Spectroscopy Comparison with Silicon Dioxide. *Science World Journal* **2013**, 208081, 2013.
84. Chernev, B.S.; Hirschl, C.; Eder, G.C. Non-destructive determination of ethylene vinyl acetate cross-linking in photovoltaic (PV) modules by Raman spectroscopy. *Applied Spectroscopy* **67**, 1296–1301, 2013.
85. Shen, Y. et al. Solvent-free electrically conductive Ag/ethylene vinyl acetate (EVA) composites for paper-based printable electronics. *RSC Advances* **9**, 19501–19507, 2019.
86. Peike, C. et al. Non-destructive degradation analysis of encapsulants in PV modules by Raman Spectroscopy. *Solar Energy Materials and Solar Cells* **95**, 1686–1693, 2011.
87. Shimoyama, M. et al. Discrimination of ethylene/vinyl acetate copolymers with different composition and prediction of the vinyl acetate content in the copolymers using Fourier-transform Raman spectroscopy and multivariate data analysis. *Vibrational Spectroscopy* **14**, 253–259, 1997.
88. Kuna, L. et al. Reducing shadowing losses with femtosecond-laser-written deflective optical elements in the bulk of EVA encapsulation. *Progress in Photovoltaics: Research and Applications* **23**, 1120–1130, 2015.
89. Hirschl, C. et al. Determining the degree of crosslinking of ethylene vinyl acetate photovoltaic module encapsulants—A comparative study. *Solar Energy Materials and Solar Cells* 116, 203–218, 2013.
90. Sakthisabarimoorthi, A.; Dhas, S.A.M.A.; Jose, M. Nonlinear optical properties of Ag@SiO_2 core-shell nanoparticles investigated by continuous wave He-Ne laser. *Materials Chemistry and Physics* **212**, 224–229, 2018.
91. Sun, D.-H.; Lu, P.; Zhang, J.-L.; Liu, Y.-L.; Ni, J.-Z. Synthesis of the Fe_3O_4@SiO_2@SiO_2-Tb(PABA)3 luminomagnetic micro-spheres. *Journal of Nanoscience and Nanotechnology*. 11, 9774–9779, 2011.
92. Ramalla, I.; Gupta, R.K.; Bansal, K. Effect on superhydrophobic surfaces on electrical porcelain insulator, improved technique at polluted areas for longer life and reliability. *International Journal of Engineering & Technology* **4**, 509, 2015.
93. Liang, Y. et al. Synthesis and characterization of core–shell structured SiO_2@YVO_4:Yb^{3+},Er^{3+} microspheres. *Applied Surface Science* **258**, 3689–3694, 2012.
94. Siddiqui, M.R.H. et al. Synthesis and characterization of silver oxide and silver chloride nanoparticles with high thermal stability. *Asian Journal of Chemistry* 25, 3405–3409, 2013.

95. Oje, A.I. et al. Electrochemical energy storage of silver and silver oxide thin films in an aqueous NaCl electrolyte. *Journal of Electroanalytical Chemistry* **829**, 59–68, 2018.
96. Aguilar-Reynosa, A. et al. Microwave heating processing as alternative of pretreatment in second-generation biorefinery: An overview. *Energy Conversion and Management* **136**, 50–65, 2017.
97. Ramãrez-Hernãndez, A.; Aguilar-Flores, C.; Aparicio-Saguilãn, A. Fingerprint analysis of FTIR spectra of polymers containing vinyl acetate. *DYNA* **86**, 198–205, 2019.
98. Marcilla, A.; Gómez, A.; Menargues, S. TGA/FTIR study of the catalytic pyrolysis of ethylene–vinyl acetate copolymers in the presence of MCM-41. *Polymer Degradation and Stability* **89**, 145–152, 2005.
99. Marcilla, A.; Gómez, A.; Menargues, S. TGA/FTIR study of the evolution of the gases evolved in the catalytic pyrolysis of ethylene-vinyl acetate copolymers. Comparison among different catalysts. *Polymer Degradation and Stability* **89**, 454–460, 2005.
100. Hoang, T. et al. Effects of maleic anhydride grafted ethylene/vinyl acetate copolymer (EVA) on the properties of EVA/silica nanocomposites. *Macromolecules Research* **21**, 1210–1217, 2013.
101. Poljanšek, I. et al. Emulsion copolymerization of vinyl acetate-ethylene in high pressure reac-tor-characterization by inline FTIR spectroscopy. *Progress in Organic Coatings* **76**, 1798–1804, 2013.
102. Iijima, M. et al. Free-standing, roll-able, and transparent silicone polymer film prepared by using nanoparticles as cross-linking agents. *Advanced Powder Technololy* **24**, 625–631, 2013.
103. Jia, Y. et al. A combined interfacial and in-situ polymerization strategy to construct well-defined core-shell epoxy-containing SiO_2-based microcapsules with high encapsulation loading, super thermal stability and nonpolar solvent tolerance. *International Journal Smart Nano Materials* **7**, 221–235, 2016.
104. Duquesne, S.; Jama, C.; Le Bras, M.; Delobel, R.; Recourt, P.; Gloaguen, J.M. Elaboration of EVA–nanoclay systems-characterization, thermal behaviour and fire performance. *Composite Science Technology* **63**, 1141–1148, 2003.
105. Zanetti, M. et al. Synthesis and thermal behaviour of layered silicate–EVA nanocomposites. *Polymer* **42**, 4501–4507, 2001.
106. Shimoyama, M. et al. Discrimination of ethylene/vinyl acetate copolymers with different composition and prediction of the content of vinyl acetate in the copolymers and their melting points by near-infrared spectroscopy and chemometrics. *Journal Polymer Science: Part B Polymer Physics* 36, 1529–1537, 1998.
107. Watari, M.; Ozaki, Y. Calibration Models for the Vinyl Acetate Concentration in Ethylene-Vinyl Acetate Copolymers and its On-Line Monitoring by Near-Infrared Spectroscopy and Chemometrics: Use of Band Shifts Associated with Variations in the Vinyl Acetate Concentration to Improve the Models. *Applied Spectroscopy* 59, 912–919, 2005.
108. Li, H.Y. et al. Optical transmission as a fast and non-destructive tool for determination of ethylene-co-vinyl acetate curing state in photovoltaic modules. *Progress in Photovoltaics: Research and Applications* **21**, 187–194, 2013.
109. Paul, K.K.; Ghosh, R.; Giri, P.K. Mechanism of strong visible light photocatalysis by Ag_2O-nanoparticle-decorated monoclinic TiO_2 porous nanorods. *Nanotechnology* 27, 315703, 2016.
110. Deng, A.; Zhu, Y. Synthesis of $TiO_2/SiO_2/Ag/Ag_2O$ and $TiO_2/Ag/Ag_2O$ nanocomposite spheres with photocatalytic performance. *Research on Chemical Intermediates* **44**, 4227–4243, 2018.

111. Shume, W.M.; Murthy, H.C.A.; Zereffa, E.A. A Review on Synthesis and Characterization of Ag_2O Nanoparticles for Photocatalytic Applications. *Journal of Chemistry* **2020**, 5039479, 2020.
112. Spreadborough, J.; Christian, J.W. High-temperature X-ray diffractometer. *Journal of Scientific Instruments* **36**, 116–118, 1959.
113. Hui, S.; Chaki, T.K.; Chattopadhyay, S. Effect of silica-based nanofillers on the properties of a low-density polyeth-ylene/ethylene vinyl acetate copolymer based thermoplastic elastomer. *Journal Applied Polymer Science* **110**, 825–836, 2008.
114. Filip, D.; Macocinschi, D.; Paslaru, E.; Munteanu, B.S.; Dumitriu, R.P.; Lungu, M.; Vasile, C. Polyurethane biocompatible silver bionanocomposites for biomedical applications. *Journal of Nanoparticle Research* **16**, 2710, 2014.
115. ISO 4892-2:2013 Plastics — Methods of exposure to laboratory light sources — Part 2: Xenon-arc lamps. 2013.
116. Silva, J. S. et al. α-$AgVO_3$ Decorated by Hydroxyapatite ($Ca_{10}(PO_4)_6(OH)_2$): Tuning Its Photoluminescence Emissions and Bactericidal Activity. *Inorganic Chemistry* **58**, 5900–5913, 2019.
117. Assis, M. et al. Ag Nanoparticles/α-Ag_2WO_4 Composite Formed by Electron Beam and Femtosecond Irradiation as Potent Antifungal and Antitumor Agents. *Scientific Reports* **9**, 9927, 2019.
118. Sun, R.; Chen, Z.; Yang, Y.; Peng, J.; Zheng, T. Effects and mechanism of SiO_2 on photocatalysis and super hydrophilicity of TiO_2 films prepared by sol-gel method. *Materials Research Express* **6**, 46409, 2019.
119. Yao, C.; Zhu, J. Synthesis, Characterization and Photocatalytic Activity of Au/SiO_2@TiO_2 Core-Shell Microspheres. *Journal of Brazilian Chemical Society* **31**, 589–596, 2020.
120. Salgado, B.C.B.; Valentini, A. Evaluation of the Photocatalytic Activity of SiO_2@TiO_2 Hybrid Spheres in the Degradation of Methylene Blue and Hydroxylation of Benzene: Kinetic and Mechanistic Study. *Brazilian Journal of Chemical Engineering* **36**, 1501–1518, 2019.
121. Hou, Y.X. et al. A comparison study of SiO_2/nano metal oxide composite sphere for antibacterial application. *Composites Part B: Engineering* **133**, 166–176, 2018.
122. Shen, J. et al. Preparation and characterization of PES–SiO_2 organic–inorganic composite ultrafiltration membrane for raw water pretreatment. *Chemical Engineering Journal* **168**, 1272–1278, 2011.
123. Yu, H. et al. Preparation and antibacterial property of SiO_2–Ag/PES hybrid ultrafiltration membranes. *Desalination and Water Treatment* **51**, 3584–3590, 2013.

SUPPLEMENTARY INFORMATION

SiO_2-Ag Composite as a Highly Virucidal Material: A Roadmap that Rapidly Eliminates SARS-CoV-2

Marcelo Assis[1,2], Luiz Gustavo P. Simoes[3], Guilherme C. Tremiliosi [3], Dyovani Coelho[1],

Daniel T. Minozzi[3], Renato I. Santos[3], Daiane C. B. Vilela[3], Jeziel Rodrigues do Santos[1], Lara Kelly Ribeiro[1], Ieda Lucia Viana Rosa[1], Lucia Helena Mascaro[1], Juan Andrés[2] & Elson Longo[1]

[1]CDMF, LIEC, Federal University of São Carlos (UFSCar), 13565-905 São Carlos, SP, Brazil.

[2]Department of Physical and Analytical Chemistry, University Jaume I (UJI), 12071 Castellon, Spain.

[3]Nanox Tecnologia S/A, 13562-400 São Carlos, SP, Brazil.

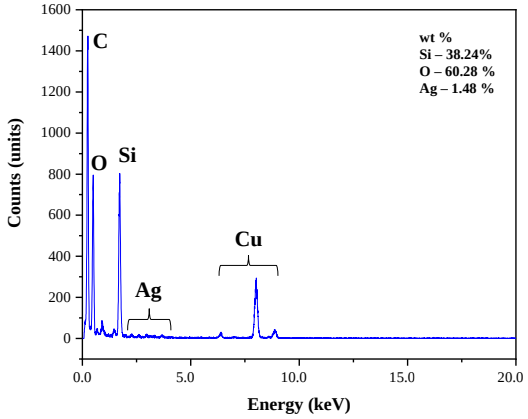

Figure SI1 - Chemical composition from EDX analysis of the SiO_2-Ag.

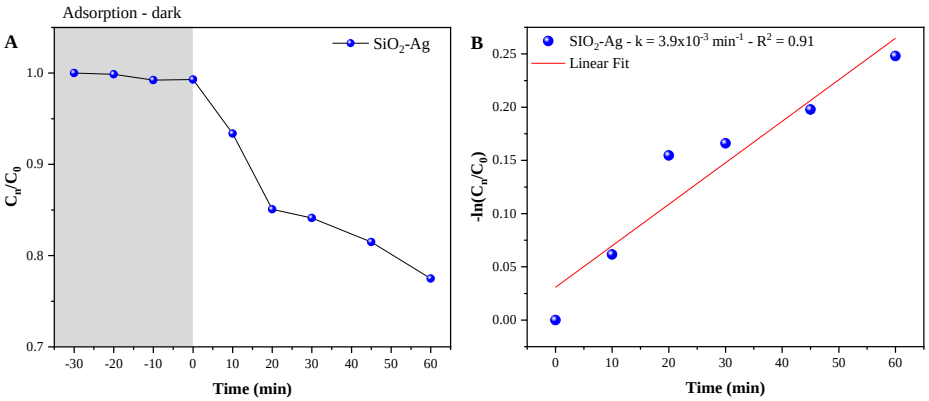

Figure SI2 - (A) Relative concentration of RhB dye (C_n/C_0). (B) Reaction kinetics of the RhB degradation $-\ln(C_n/C_0)$ versus time (min) for SiO_2-Ag composite.

Silica surfaces have been extensively studied through theoretical calculations with both a cluster and periodic approach. The choice of the modeling method is still a matter of debate, since studies show that cluster calculations that do not take into account the long-range interaction approximations imposed by the extremities are not adequate to describe the silanol groups (Si-OH). For our model we have 1 ring with 4 silicon, 5 silicon and 7 silicon. Our model is composed by three polygons: square, pentagon and heptagon, and later the atoms with the same position were removed. (Figure SI3) So this model has 12 Si atoms and 22 oxygen atoms, that is, the surface has two oxygen vacancies. The corresponding optimized SiO_2 model was

presented in Figure SI4 and Table SI1. On the other hand, it is well known that the functional hybrid B3LYP is appropriate for studies of interactions with small molecules, such as H_2O.[1,2]

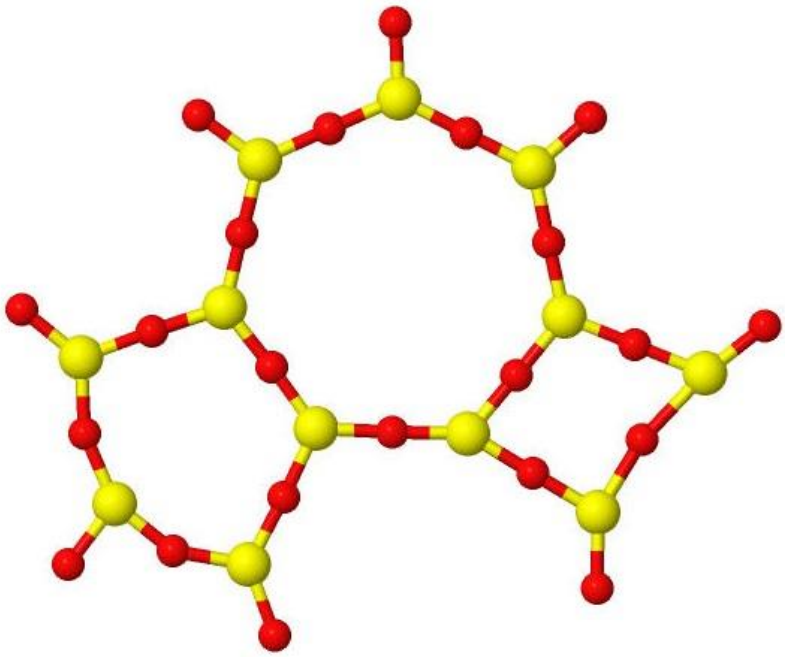

Figure SI3 - Schematic representation of the different rings used for modeling SiO_2. Silicon (yellow) and Oxygen (red).

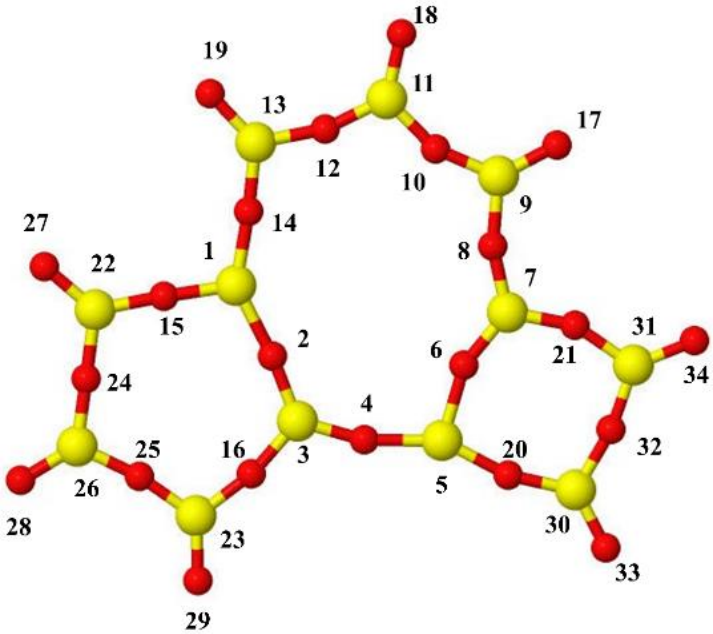

Figure SI4. The optimized SiO_2 model used in the calculations.

Table SI1 - Bond angles and lengths of the structure used.

connectivity	bond length (Å)	connectivity	bond angle (º)
Si_1-O_2	1.86	O_{14}-Si_1-O_2	143.2
O_2-Si_3	1.65	O_2-Si_3-O_4	126.5
Si_3-O_4	1.61	O_4-Si_5-O_6	105.1
O_4-Si_5	1.81	O_6-Si_7-O_8	127.2
Si_5-O_6	1.85	O_8-Si_9-O_{10}	109.1
O_6-Si_7	1.60	O_{10}- Si_{11}-O_{12}	108.1
Si_7-O_8	1.59	O_{12}- Si_{13}-O_{14}	106.8
O_8-Si_9	1.64	O_{15}- Si_1-O_2	108.4
Si_9-O_{10}	1.60	O_{16}- Si_3-O_2	117.7
O_{10}-Si_{11}	1.63	O_{25}-Si_{23}-O_{16}	107.8
Si_{11}-O_{12}	1.60	O_{24}-Si_{26}-O_{25}	108.2
O_{12}-Si_{13}	1.64	O_{24}- Si_{22}-O_{15}	108.9
Si_{13}-O_{14}	1.61	O_{20}-Si_6-O_5	101.6
O_{14}-Si_1	1.74	O_{21}-Si_7-O_6	119
O_{15}-Si_1	1.70	O_{32}-Si_{30}-O_{20}	107.3
O_{16}-Si_3	1.63	O_{32}-Si_{31}-O_{21}	105.6
O_{17}-Si_9	1.54	O_{17}-Si_9-O_8	122.2
O_{18}-Si_{11}	1.54	O_{18}-Si_{11}-O_{10}	123.1
O_{19}-Si_{13}	1.54	O_{19}-Si_{13}-O_{12}	122.3
O_{20}-Si_5	1.74	O_{27}-Si_{22}-O_{15}	128.5
O_{21}-Si_7	1.60	O_{28}-Si_{26}-O_{24}	128.8
Si_{22}-O_{15}	1.62	O_{29}-Si_{23}-O_{25}	126.5
Si_{23}-O_{16}	1.62	O_{33}-Si_{30}-O_{20}	130.3
O_{24}-Si_{22}	1.62	O_{34}-Si_{32}-O_{33}	130.0
O_{25}-Si_{23}	1.62	-	-
Si_{26}-O_{25}	1.62	-	-
O_{27}-Si_{22}	1.54	-	-
O_{28}-Si_{26}	1.54	-	-
O_{29}-Si_{23}	1.54	-	-
Si_{30}-O_{20}	1.63	-	-
Si_{31}-O_{21}	1.66	-	-
O_{32}-Si_{30}	1.64	-	-
O_{33}-Si_{30}	1.54	-	-
O_{34}-Si_{31}	1.54	-	-

In **Figure SI5** the map of the molecular electrostatic potential of the SiO_2 is displayed. The regions acting as electron receptor for H_2O and an electron donor for molecular O_2 are highlighted. The analysis of the charge transfer from H_2O to SiO_2 is 0.04 e^{--}, on the other hand,

the surface of SiO_2 is able to transfer 0.10 e^- to O_2 molecule After this charge transfer, new ectrophilic/nucleophilic centers appear on the surface giving the quantum probability of new interactions.

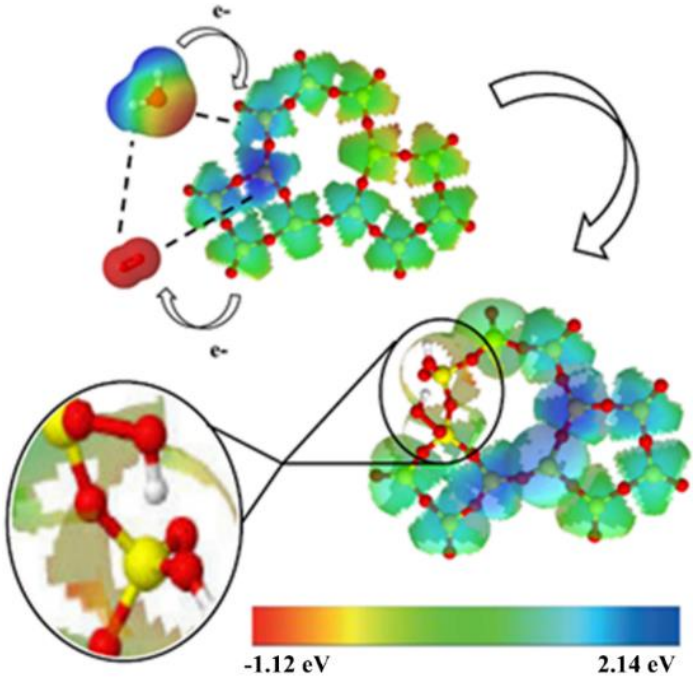

Figure SI5 – MEP (in eV) of SiO_2 model.

References

1. Civalleri, B.; Garrone, E.; Ugliengo, P. Ab Initio Study of the Adducts of Small Molecules with the Isolated Hydroxyl of Silica and the Brønsted Site in Zeolites: A Comparison between B3-LYP and MP2 Methods. *The Journal of Physical Chemistry B*, **102**, 2373–2382, 1998.
2. Bera, S. et al. Design of Visible-Light Photocatalysts by Coupling of Inorganic Semiconductors. *Catalysis Today* **335**, 3–19, 2019.

3 – CONCLUSIONS

Pathogenic microorganisms (bacteria, fungi and viruses) represent a major public health problem. Therefore, there is great interest in the development of new materials and new technologies capable of eliminating opportunistic pathogens, reducing the risk of infection and transmission by them. This thesis presents a set of published articles whose results were achieved through the use of metal-semiconductor interfaces, which can be obtained by chemical synthesis methods or by physical modification methods (electron beam and femtosecond laser irradiation).Materials obtained through these methods have shown great biocidal properties against a variety of pathogens resulting very attractive from the biotechnological point of view. In fact, these new materials constitute an alternative to the usual anticancer therapies. Their effectiveness has been demonstrated and linked to their ability to generate ROS, which interact with specific proteins, membranes and intra- and extracellular components essential for maintaining the life of both microorganisms and cells.

REFERENCES

ABO-ZEID, Y. et al. **A molecular docking study repurposes FDA approved iron oxide nanoparticles to treat and control COVID-19 infection**. European Journal of Pharmaceutical Sciences, v. 153, p. 105465, 2020.

ASSIS, M. e GROPPO FILHO, F. C. et al. **Ag Nanoparticles/AgX (X=Cl, Br and I) Composites with Enhanced Photocatalytic Activity and Low Toxicological Effects**. ChemistrySelect, v. 5, p. 4655–4673, 23 2020.

ASSIS, M. et al. **In Situ Growth of Bi Nanoparticles on $NaBiO_3$, δ-, and β-Bi_2O_3 Surfaces: Electron Irradiation and Theoretical Insights**. The Journal of Physical Chemistry C, v. 123, p. 5023–5030, 2019.

ASSIS, M. e CORDONCILLO, E. et al. **Laser-induced formation of bismuth nanoparticles**. Physical Chemistry Chemical Physics, v. 20, p. 13693–13696, 2018.

ASSIS, M. e MACEDO, N. G et al. **Laser/Electron Irradiation on Indium Phosphide (InP) Semiconductor: Promising Pathways to In Situ Formation of Indium Nanoparticles**. Particle & Particle Systems Characterization, v. 35, p. 1800237, 2018.

ASSIS, M. e SIMOES, L.G.P. et al. **SiO_2-Ag Composite as a Highly Virucidal Material: A Roadmap that Rapidly Eliminates SARS-CoV-2**. Nanomaterials, v. 11, p. 638, 2021.

ASSIS, M. e DE FOGGI, C. C. et al. **Surface-dependent photocatalytic and biological activities of Ag_2CrO_4: Integration of experiment and simulation**. Applied Surface Science, v. 545, p. 148964, 2021.

ASSIS, M. e CORDONCILLO, E. e TORRES-MENDIETA, R. et al. **Towards the scale-up of the formation of nanoparticles on α-Ag_2WO_4 with bactericidal properties by femtosecond laser irradiation**. Scientific Reports, v. 8, p. 1–11, 2018.

ASSIS, M. e PONTES RIBEIRO, R.A.P. et al. **Unconventional Magnetization Generated from Electron Beam and Femtosecond Irradiation on α-Ag_2WO_4: A Quantum Chemical Investigation**. ACS Omega, v. 5, p. 10052–10067, 2020.

ASTRUC, D. e LU, F. e ARANZAES, J.R. **Nanoparticles as Recyclable Catalysts: The Frontier between Homogeneous and Heterogeneous Catalysis**. Angewandte Chemie, v. 44, p. 7852–7872, 2005.

BALTA, S, et al. **A new outlook on membrane enhancement with nanoparticles: The alternative of ZnO**. Journal of Membrane Science, v. 389, p. 155–161, 2012.

BARUAH, S. e DUTTA, J. **Nanotechnology applications in pollution sensing and degradation in agriculture: a review**. Environmental Chemistry Letters, v. 7, p. 191–204, 2009.

BEHZADINASAB, S. et al. **A Surface Coating that Rapidly Inactivates SARS-CoV-2**. ACS Applied Materials & Interfaces, v. 12, p. 34723–34727, 2020.

BUI, T.Q. et al.. **A density functional theory study on silver and bis-silver complexes with lighter tetrylene: are silver and bis-silver carbenes candidates for SARS-CoV-2 inhibition? Insight from molecular docking simulation**. RSC Advances, v. 10, p. 30961–30974, 2020.

BUOT, F.A. **Mesoscopic physics and nanoelectronics: nanoscience and nanotechnology**. Physics Reports, v. 234, p. 73–174, 1993.

CARVALHO, A.P. et al. **Recent Advances on Nanomaterials to COVID-19 Management: A Systematic Review on Antiviral/Virucidal Agents and Mechanisms of SARS-CoV-2 Inhibition/Inactivatio.** Global Challenges, v. 5, p. 2000115, 2021.

CHEN, M. et al. **Complementary enhanced solar thermal conversion performance of core-shell nanoparticles**. Applied Energy, v. 211, p. 735–742, 2018.

CHEN, N. et al. **Inhibitory effects of silver nanoparticles against adenovirus type 3 in vitro**.

Journal of Virological Methods, v. 193, p. 470–477, 2013.
CHERIYAMUNDATH, S. e VAVILALA, S.L. **Nanotechnology-based wastewater treatment**. Water and Environment Journal, v. 35, p. 123–132, 2021.
CHIN, A.W.H. et al. **Stability of SARS-CoV-2 in different environmental conditions**. The Lancet Microbe, v. 5247, p. 2004973, 2020.
CHINTAGUNTA, A.D. et al. **Nanotechnology: an emerging approach to combat COVID-19.** Emergent materials, p. 1–12, Fev 2021.
CILEK, E.C. e KARACA, S. **Effect of nanoparticles on froth stability and bubble size distribution in flotation**. International Journal of Mineral Processing, v. 138, p. 6–14, 2015.
CLAVERO, C. **Plasmon-induced hot-electron generation at nanoparticle/metal-oxide interfaces for photovoltaic and photocatalytic devices**. Nature Photonics, v. 8, p. 95–103, 2014.
CRUZ, L. et al. **Multi-dimensional architecture of Ag/α-Ag_2WO_4 crystals: insights into microstructural, morphological, and photoluminescence properties**. CrystEngComm, v. 22, p. 7903–7917, 2020.
DE FOGGI, C.C. et al. **Unvealing the role of β-Ag_2MoO_4 microcrystals to the improvement of antibacterial activity**. Materials Science and Engineering: C, v. 111, p. 110765, 2020.
DE OLIVEIRA, R.C. et al. **Disclosing the electronic structure and optical properties of $Ag_4V_2O_7$ crystals: experimental and theoretical insights**. CrystEngComm, v. 18, p. 6483–6491, 2016.
DE OLIVEIRA, R.C. et al. **Mechanism of Antibacterial Activity via Morphology Change of α-$AgVO_3$: Theoretical and Experimental Insights**. ACS Applied Materials & Interfaces, v. 9, p. 11472–11481, 2017.
DOS SANTOS, C.C. et al. **Proof-of-Concept Studies Directed toward the Formation of Metallic Ag Nanostructures from Ag_3PO_4 Induced by Electron Beam and Femtosecond Laser**. Particle & Particle Systems Characterization, v. 36, p. 1800533, 2019.
ELTARAHONY, Marwa e colab. **Biosynthesis, Characterization of Some Combined Nanoparticles, and Its Biocide Potency against a Broad Spectrum of Pathogens**. Journal of Nanomaterials, v. 2018, p. 5263814, 2018.
FOMINYKH, K. et al. **Ultrasmall Dispersible Crystalline Nickel Oxide Nanoparticles as High-Performance Catalysts for Electrochemical Water Splitting**. Advanced Functional Materials, v. 24, p. 3123–3129, 2014.
GAIKWAD, S. et al. **Antiviral activity of mycosynthesized silver nanoparticles against herpes simplex virus and human parainfluenza virus type 3**. International Journal of Nanomedicine, v. 8, p. 4303–4314, 2013.
GHAFFARI, M. et al. **An overview of the use of biomaterials, nanotechnology, and stem cells for detection and treatment of COVID-19: towards a framework to address future global pandemics.** Emergent materials, p. 1–16, 2021.
GHATAK, J. e GUAN, W. e MÖBUS, G. **In situ TEM observation of lithium nanoparticle growth and morphological cycling**. Nanoscale, v. 4, p. 1754–1759, 2012.
GRANO, A.J. et al. **In situ observation of sintering of nickel nanoparticles during nanocasting into mesoporous silica**. Materials Letters, v. 111, p. 154–157, 2013.
GUSEINOV, N.R. e ILYIN, A.M. **Electrostatic energy analyzer for nanotechnology applications**. Journal of Electron Spectroscopy and Related Phenomena, v. 246, p. 147031, 2021.
HOSSEINI, M. et al. **Cupric Oxide Coating That Rapidly Reduces Infection by SARS-CoV-2 via Solids.** ACS applied materials & interfaces, v. 13, p. 5919–5928, 2021.
HUANG, Z.et al. **Antimicrobial Magnesium Hydroxide Nanoparticles As an Alternative to Cu Biocide for Crop Protection.** Journal of agricultural and food chemistry, v. 66, p. 8679–8686, Ago 2018.

ICHIKAWA, K. et al. **Control of Calcium Carbonate Polymorphism and Morphology through Biomimetic Mineralization by means of Nanotechnology**. Chemistry – A European Journal, v. 9, p. 3235–3241, 2003.
JEREMIAH, S.S. et al. **Potent antiviral effect of silver nanoparticles on SARS-CoV-2**. Biochemical and Biophysical Research Communications, v. 533, p. 195–200, 2020.
JINDAL, S. e GOPINATH, P. **Nanotechnology based approaches for combatting COVID-19 viral infection**. Nano Express, v. 1, p. 22003, 2020.
KANAPARTHY, R. e KANAPARTHY, A. **The changing face of dentistry: nanotechnology.** International journal of nanomedicine, v. 6, p. 2799–2804, 2011.
KHAN, I. e SAEED, K. e KHAN, I. **Nanoparticles: Properties, applications and toxicities**. Arabian Journal of Chemistry, v. 12, p. 908–931, 2019.
KIM, W. Y. et al. **Application of quantum chemistry to nanotechnology: electron and spin transport in molecular devices**. Chem. Soc. Rev., v. 38, p. 2319–2333, 2009.
KNIGHT, M.W. et al. **Photodetection with Active Optical Antennas**. Science, v. 332, p. 702–704, 2011.
KOH, I. e JOSEPHSON, L. **Magnetic Nanoparticle Sensors**. Sensors, v. 9, p. 8130–8145, 2009.
LAIER, L.O. et al. **Surface-dependent properties of α-Ag_2WO_4: a joint experimental and theoretical investigation**. Theoretical Chemistry Accounts, v. 139, p. 108, 2020.
LARA, H.H. et al. **Mode of antiviral action of silver nanoparticles against HIV-1**. Journal of Nanobiotechnology, v. 8, p. 1–10, 2010.
LI, Y. et al. **MoS_2 Nanoparticles Grown on Graphene: An Advanced Catalyst for the Hydrogen Evolution Reaction**. Journal of the American Chemical Society, v. 133, p. 7296–7299, 2011.
LONGO, E. et al.. **Direct in situ observation of the electron-driven synthesis of Ag filaments on α-Ag_2WO_4 crystals**. Scientific Reports, v. 3, p. 1676, 2013.
LONGO, E. et al.. **In situ Transmission Electron Microscopy observation of Ag nanocrystal evolution by surfactant free electron-driven synthesis**. Scientific Reports, v. 6, p. 21498, 2016.
MA, C. et al. **The optical duality of tellurium nanoparticles for broadband solar energy harvesting and efficient photothermal conversion**. Science Advances, v. 4, 2018.
MACEDO, N.G. et al. **Surfactant-Mediated Morphology and Photocatalytic Activity of α-Ag_2WO_4 Material**. Journal of Physical Chemistry C, v. 122, n. 15, p. 8667–8679, 2018.
MACEDO, N.G. et al. **Tailoring the bactericidal activity of Ag nanoparticles/α-Ag_2WO_4 composite induced by electron beam and femtosecond laser irradiation: Integration of experiment and computational modeling**. ACS Applied Bio Materials, v. 2, p. 824–837, 2019.
MACHADO, T.R. et al. **From Complex Inorganic Oxides to Ag–Bi Nanoalloy: Synthesis by Femtosecond Laser Irradiation**. ACS Omega, v. 3, p. 9880–9887, 2018.
MAIO, F.D. et al. **Graphene nanoplatelet and Graphene oxide functionalization of face mask materials inhibits infectivity of trapped SARS-CoV-2**. medRxiv, 2020.
MALLAKPOUR, S. et al. **The latest strategies in the fight against the COVID-19 pandemic: the role of metal and metal oxide nanoparticles. New Journal of Chemistry**. v, 14, p. 6167-6179, 2021.
MILEWSKA, A. et al. **HTCC as a Polymeric Inhibitor of SARS-CoV-2 and MERS-CoV.** Journal of virology, v. 95, 2021.
MLCOCHOVA, P. et al. **Extended in vitro inactivation of SARS-CoV-2 by titanium dioxide surface coating**. bioRxiv, 2020.
OLAYIWOLA, S.O. e DEJAM, M. **Interfacial energy for solutions of nanoparticles, surfactants, and electrolytes**. AIChE Journal, v. 66, p. e16891, 2020.

LEMOS, P.S. et al. **Laser and electron beam-induced formation of Ag/Cr structures on Ag_2CrO_4**. Physical Chemistry Chemical Physics, v. 21, p. 6101–6111, 2019.
PANDEY, A. et al. **Architectured Therapeutic and Diagnostic Nanoplatforms for Combating SARS-CoV-2: Role of Inorganic, Organic, and Radioactive Materials**. ACS Biomaterials Science & Engineering, v. 7, p. 31–54, 2021.
PARK, J.H. et al. **Size control of copper nanoparticle by electron beam irradiation**. Materials Research Innovations, v. 18, p. S2-678-S2-684, 2014.
PEREIRA, P.F.S. et al. **$ZnWO_4$ nanocrystals: synthesis, morphology, photoluminescence and photocatalytic properties**. Physical Chemistry Chemical Physics, v. 20, n. 3, p. 1923–1937, 2018a.
PERFÉZOU, M. e TURNER, A. e MERKOÇI, A. **Cancer detection using nanoparticle-based sensors**. Chemical Society reviews, v. 41, p. 2606—2622, 2012.
PRATHER, K.A. e WANG, C.C. e SCHOOLEY, R.T. **Reducing transmission of SARS-CoV-2**. Science, v. 368, p. 1422–1424, 2020.
PRIETO, G. et al. **Towards stable catalysts by controlling collective properties of supported metal nanoparticles**. Nature Materials, v. 12, p. 34–39, 2013.
SALATA, O.V. **Applications of nanoparticles in biology and medicine**. Journal of Nanobiotechnology, v. 2, p. 3, 2004.
SATHISH, M. e VISWANATHAN, B. e VISWANATH, R.P. **Alternate synthetic strategy for the preparation of CdS nanoparticles and its exploitation for water splitting**. International Journal of Hydrogen Energy, v. 31, p. 891–898, 2006.
SCHULZE, S. et al. **Morphological Differentiation of Neurons on Microtopographic Substrates Fabricated by Rolled-Up Nanotechnology**. Advanced Engineering Materials, v. 12, p. B558–B564, 2010.
SHCHUKIN, D.G. e CARUSO, R.A. **Inorganic Macroporous Films from Preformed Nanoparticles and Membrane Templates: Synthesis and Investigation of Photocatalytic and Photoelectrochemical Properties**. Advanced Functional Materials, v. 13, p. 789–794, 2003.
SPESHOCK, J.L. et al. **Interaction of silver nanoparticles with Tacaribe virus**. Journal of Nanobiotechnology, v. 8, p. 19, 2010.
SUBEDI, S. **An introduction to nanotechnology and its implications**. Himalayan Physics, v. 5, p. 78–81, 2015.
SUGIMOTO, T. **Underlying mechanisms in size control of uniform nanoparticles.** Journal of colloid and interface science, v. 309, p. 106–118, 2007.
TAVAKOLI, A. et al. **Polyethylene glycol-coated zinc oxide nanoparticle: an efficient nanoweapon to fight against herpes simplex virus type 1.** Nanomedicine, v. 13, p. 2675–2690, 018.
TE VELTHUIS, A.J.W. et al. **Zn^{2+} inhibits coronavirus and arterivirus RNA polymerase activity in vitro and zinc ionophores block the replication of these viruses in cell culture.** PLoS pathogens, v. 6, p. e1001176, 2010.
TELLO, A.C.M. et al. **Microwave-Driven Hexagonal-to-Monoclinic Transition in BiPO4: An In-Depth Experimental Investigation and First-Principles Study**. Inorganic Chemistry, v. 59, p. 7453–7468, 2020.
TREMILIOSI, G.C. et al. **Ag nanoparticles-based antimicrobial polycotton fabrics to prevent the transmission and spread of SARS-CoV-2**. bioRxiv, 2020.
VAN DOREMALEN, Neeltje e colab. **Aerosol and Surface Stability of SARS-CoV-2 as Compared with SARS-CoV-1**. New England Journal of Medicine, v. 382, p. 1564–1567, 2020.
VIDAL-IGLESIAS, F.J. et al. **Electrochemical Characterization of Shape-Controlled Pt Nanoparticles in Different Supporting Electrolytes**. ACS Catalysis, v. 2, p. 901–910, 2012.

WANG, Libing e colab. **Nanoparticle-based environmental sensors**. Materials Science and Engineering: R: Reports, v. 70, p. 265–274, 2010.
XU, Z.P. et al. **Dispersion and Size Control of Layered Double Hydroxide Nanoparticles in Aqueous Solutions**. The Journal of Physical Chemistry B, v. 110, p. 16923–16929, 2006.
YU, B. e MEYYAPPAN, M. **Nanotechnology: Role in emerging nanoelectronics**. Solid-State Electronics, v. 50, p. 536–544, 2006.
ZHANG, Y. et al. **Surface-Plasmon-Driven Hot Electron Photochemistry**. Chemical Reviews, v. 118, p. 2927–2954, 2018.